Shadow Nanosphere Lithography

Dissertation

zur

Erlangung des Doktorgrades (Dr. rer. nat.)

der

Mathematisch-Naturwissenschaftlichen Fakultät

der

Rheinischen Friedrich-Wilhelms-Universität Bonn

vorgelegt von

Witold Kandulski

aus

Poznań, Poland

Bonn, 2007

Angefertigt mit Genehmigung der Mathematisch-Naturwissenschaftlichen Fakultät der Rheinischen Friedrich-Wilhelms-Universität Bonn

Eidesstattliche Erklärung

Hiermit erkläre ich, diese Arbeit selbständig und ohne unerlaubte Hilfe verfasst und keine anderen als die angegebenen Quellen und Hilfsmittel verwendet zu haben.

Bonn, 18. Juni 2007

Diese Dissertation ist auf dem Hochschulschriftenserver der ULB Bonn

http://hss.ulb.uni-bonn.de/diss_online/ elektronisch publiziert.

1. Referent: Prof. Dr. Karsten Buse
2. Referent: Prof. Dr. Karl Maier

Tag der Abgabe: 18. Juni 2007

University of Bonn

Faculty of Mathematics and Natural Sciences

Institute of Physics

Shadow Nanosphere Lithography

Ph.D. Thesis

by

Witold Kandulski

This thesis presents a lithographic method, based on self-assembled two-dimensional colloidal crystals, for fabrication of large-area ($>$ cm^2) arrays of nanostructures. Preparation of colloidal crystals (≈ 200 cm^2) at the air-water interface is shown and discussed. Obtained crystals are used as lithographic masks. Utilizing shadow evaporation and reactive ion etching different nanoparticles are manufactured, such as dots, triangles, rods, rings, wires, pillars, and layers perforated with holes of various shape. Geometrical dependences of the size and shape of nanoparticles are shown and compared with experimental results.

June 2007

Contents

1. Introduction

Why do people wish to make things smaller? Imagine self-reproducible nano-robots that could manufacture food from single atoms, or arrange themselves into any useful object. Such technology would certainly have a significant impact on our civilization[1-3]. The origins of nanotechnology exist in the form of science fiction. The scientific community has adapted the term "nanotechnology" to describe the manufacture of objects in a controllable way; with dimensions from atoms to approximately 100 nm[4]. Among the many different branches of nanotechnology, metallic nanoparticles have received substantial scientific attention due to their interesting size-dependent properties; magnetic, optical, electrical, and catalytic processes are all influenced by them[5]. These reasons have stimulated development of a nanoparticle preparation method, which is the focus of this work. Before discussing this, a more general overview of structuring possibilities will be given.

There are two major routes for nanofabrication: "bottom-up" and "top-down". The "top-down" approach utilizes various techniques to scale down bulk materials and to create nanodevices. This approach uses very sophisticated preparation methods and provides the most control over composition and geometry of the manufactured structures. On the other hand, it is costly and time consuming. Examples of this approach are photolithography (PL) and electron beam lithography (EBL).

The "bottom-up" approach refers to the manipulation of atoms, molecules, or larger building blocks and their assembly into bigger structures. This can be achieved by the use of powerful microscopes, which allow nanomanipulation. Also, natural self-assembly properties of matter are used for the fabrication of more complex structures. Self-assembly is used in biotechnology and in chemistry. It is inherently parallel, time-efficient and low-cost, but it does not provide the same precision as the "top-down" approach.

Several important criteria determine the usability of nanofabrication methods that are utilized in the preparation of arrays of nanoparticles, namely: control of the geometry of the nanoparticle arrays, spatial resolution, cost, and time consumption. Table 1.1 summarizes the most popular nanofabrication techniques and their characteristics, gathered on the basis of the literature and references therein. Techniques listed in table 1.1 cannot be directly compared with each other, due to their diverse nature. They are categorized into two groups: "replication techniques" and "pattern generation" techniques. Lithographic methods (1 - 7) are replication techniques, which provide solutions for a large throughput reproduction of a pattern, but they cannot create it. Those strategies have to be assisted by pattern generation techniques in order to make a master. Techniques (8 - 17) are pattern generation techniques, which are able to create a specific pattern. These methods are compared below in terms of nanoparticle preparation while considering the aforementioned utility criteria. Methods (8 – 16) require standard etching or evaporation tools for nanofabrication. A few processes (8 - 13) also use microscopes or other advanced devices and therefore, are neither simple, nor low-priced. They all provide total control of the geometry of the structures with varying accuracy from tenths to hundreds of nanometers. Methods 14 and 15 require an optical system to generate interference between the light beams. Such systems are usually a few orders of magnitude cheap than tools used in previously mentioned techniques (8 - 13). The main advantage of interference techniques is the ability to make large nano-structured areas. Periodic nanolines or nanoparticle patterns can be manufactured easily with good reproducibility and control of the geometry of the pattern.

Block copolymer lithography and shadow nanosphere lithography (SNSL) (17 - 16) are the cheapest technologies. Block copolymer lithography is sometimes used together with a lithographically pre-patterned substrate (graphoepitaxy) for further

specific assembly of copolymers. This method is capable of manufacturing various periodic nanostructures according to the patterns achievable by thermodynamically driven systems. However, the materials employed in such nanostructure preparation are limited.

No.	Technique (abbreviation) l.=lithography	Geometry	Characte-ristic feature size	Cost	Time Con-sump-tion	Area	Ref.
1	X-ray l. (XRL)	arbitrary	≈ 20 nm	high	low	large	5
2	Deep ultraviolet l. (DUVL)	arbitrary	≈ 150 nm	high	low	large	6
3	Immersion DUV l. (DUVIL)	arbitrary	≈ 30 nm	high	low	large	7
4	Extreme ultra violet l. (EUVL)	arbitrary	< 50 nm	high	low	large	8
5	Optical projection l. (OPL)	arbitrary	≈ 40 nm	high	low	large	9
6	Step and flash l. (SFIL)	arbitrary	≈ 20 nm	low	high	large	10
7	Soft l. (SL)	arbitrary	≈ 30 nm	low	low	large	10
8	Maskless optical projection l. (MOPL)	arbitrary	≈ 90 nm	high	low	large	11
9	Zone plate array l. (ZPAL)	arbitrary	≈ 150 nm	high	low	large	11
10	Two-photon l.	arbitrary 3D	< 1 μm	low	high	large	8
11	Electron Beam l. (EBL)	arbitrary	≈ nm	high	high	small	10,11
12	Ion beam l., focused ion beam l. (IBL,FIB)	arbitrary	≈ nm	high	high	small	10,11
13	Scanning probe l. (SPL)	arbitrary	≈ nm	high	high	small	10
14	Laser focused atom deposition or neutral atom l.	periodic systems,	≈ 50 nm	low	low	large	5
15	Interference l. (IL)	periodic systems	< 100 nm	low	low	large	10,12
16	(Shadow) nanosphere l., colloidal l., natural l. ((S)NSL, CL, NL)	periodic systems, feature control	≈ 40 – 1000 nm	low	low	large	13–17
17	Block copolymer l.	periodic systems	≈ 10 - 100 nm	low	low	large	8

Table 1.1. Summary of most popular lithographic approaches.

The SNSL technique is composed of two stages, the first of which is mask preparation. It is based on self-assembly of microspheres into a monolayer. Such a monolayer of periodically arranged microspheres is called a "two-dimensional (2D) colloidal crystal"[18]. The second part of the lithographic process uses well-known nanomachining techniques – etching and metal deposition – to pattern the substrate. Due to the parallel nature of the microsphere assembly, SNSL is capable of making a large-area mask (≈ 200 cm^2) in a relatively short time (≈ 2 - 5 h). The second step allows modification of the mask substrate patterning. The lithographic pattern-generation techniques (8 - 13), can easily produce arrays of nanoparticles with high precision. However, complexity of the preparation process (mask preparation can take seconds to days per cm^2 of nanostructure depending on morphology) and high initial equipment costs make these techniques unaffordable

for many researchers[11]. Techniques (14 - 17) provide arrays at a much lower price, but without controlled morphology of the nanoparticles (14 - 15). Foregoing consideration of the lithographic techniques, in terms of nanoparticle array preparation, leads to the conclusion that NSL is one of the most convenient approaches. The large potential of the colloidal masks has been noticed and considered as a strong advantage in comparison to other laboratory methods in the area of nanoparticle and mesoscopic structures. This is mainly due to low laboratory requirements, low cost, fast preparation and (in contrast to other self-assembly approaches) outstanding control over nanoparticle shape.

Nanosphere lithography also has other names: "colloidal lithography" and "natural lithography". In 1981 Fischer and Zingsheim reported the use of a simple drop-coated, colloidal monolayer as a lithographic mask for preparation of platinum nanostructures[17]. However, the focus of their work was the replication of submicroscopic patterns using visible light and not realization of lithographic colloidal masks. One year later Deckman and Dunsmuir have extended the idea of this technique. They have shown results of two-fold mask preparation: using electrostatic adsorption and the spin-coating technique. Because the mask preparation process was based on the naturally occurring self-assembly phenomenon, they named this strategy "natural lithography"[14,15]. Over the last ten years Van Duyne *et al.* have popularized natural lithography under the name of "nanosphere lithography"[19]. Since the pioneering works of Fischer *et al.* and Deckman *et al.*, many groups have started to develop new approaches and to improve established methods in order to fabricate better quality colloidal masks. Each of these methods, together with briefly introduced strengths and weaknesses, are described in the following list.

Evaporation methods[7,20–25]

Evaporation methods are based on solvent evaporation from a droplet of a particle suspension deposited on a substrate. When the content of the solvent in the solution is very low, it forms a very thin layer over the substrate, and the particles start to self-organize. This kind of method is suitable for very small (hundreds of square microns) areas of a multicrystalline mask. Low control over the process often yields mixed multilayer structures.

Electrostatic deposition[14,15,26]

Electrostatic deposition is based on electrostatic attraction forces acting between counter-ions, and requires oppositely charged surfaces of the substrate and particles in an electrolytic solution. Electrostatic deposition can create almost area-unlimited masks, the only limit is the amount of colloid suspension used for preparation. Since the adsorption process is parallel, the spheres do not arrange into periodic structures.

Dip-coating[27]

Dip coating uses the same principle of monolayer formation as the one used in evaporation deposition, but the substrate is removed vertically from a bulk suspension of colloidal spheres with a constant velocity. In contrast to evaporation methods it is suitable for large-area preparation - tens of square millimeters can be covered. Masks obtained via this method have a multicrystalline structure that includes a substantial number of defects.

Langmuir-Blodgett coating[28]

Langmuir-Blodgett coating refers to preparation and transfer of nanosphere monolayers from a liquid-gas interface onto a solid substrate by controlled vertical removal of the substrate. The differential surface tension, or surface pressure, of the monolayer is controlled by a feedback system. This setup assures that the pressure in the monolayer remains constant as the substrate is being withdrawn,

and as a consequence it helps to maintain homogeneous stacking of the layer. This procedure is well-established and has been commonly used for preparation and examination of molecular layers. Using this route, macroscopic areas can be patterned with nanospheres, however a substantial number of structural defects is often present.

Electrophoretic deposition[29,30]

Electrophoretic deposition uses electrical currents for the deposition and self-assembly of latex nanospheres. Two- and three-dimensional colloidal crystals have been prepared using this technique. Although this method provides macroscopic colloidal crystals, it is limited to conductive substrates.

Self-assembly on pre-patterned substrates[31,32]

Self-assembly on pre-patterned substrates combines conventional lithographic techniques and self-assembled sphere monolayers. This method provides control at the mesoscopic scale depending on the accuracy of the lithographic method used for pre-patterning of the substrate. Subsequently, a fine structure of spheres is formed in the previously functionalized or patterned areas due to interactions between spheres and those areas. The first patterning step significantly raises the total processing time and cost of preparation.

Spin-coating[14,15,33,34]

Spin-coating is commonly used in the field of lithography to make thin layers of photoresist. Latex dispersion, with properly adjusted viscosity and density, can also be used to make a thin layer. Once the liquid is distributed on the substrate, and placed on the rotary stage, the rapid spinning movement of the stage makes the liquid flow away. Besides viscosity and density of the applied liquid, other key-factors include the surface properties of the substrate and the spinning rate of the stage. The ordering mechanism is similar to that during assembly of microspheres on a glass substrate[22]. When the thickness of the layer of microsphere dispersion is getting thinner, the spheres start to protrude from the water, giving rise to the water flux from thicker areas towards protruding spheres, which assembles them into a crystal. This approach is very convenient for preparation of two-dimensional colloidal crystals. The arrays obtainable by this process are large - tens or hundreds of square centimeters, and multicrystalline.

Self-assembly at the interface of two different media[35–37]

Self-assembly at the interface of two different media is similar to the Langmuir-Blodgett technique. The nanospheres are dispersed in a two-phase liquid medium or on the top of the surface of the liquid. Due to carefully prepared surface conditions, nanospheres assemble at the interface. Once they are trapped at the interface of two different media, they self-organize into a monolayer due to attractive forces. Subsequently, the monolayer is deposited on the substrate by a simple removal procedure or by evaporation of the subphase. Large surfaces (tens or hundreds of square centimeters) of multicrystalline monolayers have been realized. The same approach is used in the following (SNSL) technique.

Shadow nanosphere lithography[13,16]

Shadow nanosphere lithography (SNSL) consists of two subsequent processing steps: assembly of the colloidal mask and subsequent "top-down" patterning. The first step of SNSL, is studied in the present work, and assembly of interfacial colloidal crystals is improved. With carefully tuned chemical composition of the nanosphere suspension, a 2D balanced system was achieved that allowed formation of large (≈ 200 cm^2) colloidal multicrystalline monolayers. Self-assembly at the interface is particularly interesting for several reasons. First, the nanospheres have time to arrange into a crystal, in comparison to other methods. Second, trapped interfacial multicrystals can rearrange themselves into larger monocrystals due to

the motion of the liquid subphase. It will be shown that monocrystallinity is essential for the preparation of such nanostructures like periodic wires. The third advantage is that a chemical laboratory with standard equipment is sufficient to manufacture the colloidal crystals. The second step of SNSL is top-down patterning using annealing, chemical modification[38], reactive ion etching (RIE)[39], and electron beam evaporation (EBE). These procedures allow control of the spacing and size, independently from each other, within tens of nanometers. The shadow approach of EBE should be emphasized due to its relative simplicity and wealth of feasible nanostructures. The described methods are important strategies for manufacture of mesoscopic structures. Structures produced using colloidal crystals have potential applications as, e.g., ultrasensitive biosensors[40], DNA electrophoresis[41], superhydrophobic materials[42], microlens arrays[43], light emitting diode (LED) arrays[44], laser arrays[36], field emitters[45], optical antennas[46], photonic crystals[47], polymer membranes[48], nanocrystals synthesis [49], and protein micropatterning[50].

2. Fundamentals

This section contains fundamental information about the concept of shadow nanosphere lithography (SNSL), and all lithographic steps are described in detail from the theoretical point of view. A general discussion about crystal structures composed of 2D arrays, preparation strategies and a number of possible nanostructures that SNSL can provide will be given. Also, other techniques involved are discussed, for example, modification of polystyrene (PS) colloidal crystals, reactive ion etching, and electron beam evaporation, including the shadow approach.

2.1. Structure of particle arrays

A monolayer composed of spheres, assembled into a lithographic mask, possesses a hexagonal close-packed (HCP), 2D lattice. The HCP structure belongs to the highly symmetrical p6m group and defines the arrangement of the particle matrix that can be manufactured using SNSL. Many of the 2D lattices that belong to one of the 6pm sub-groups can be manufactured. For example, by deposition of material through two successive colloidal 2D crystals, various Moiré patterns can be created[33,51]. It was calculated that using mixtures of differently sized spheres[52] other arrangements are also possible. Arbitrarily designed ordered patterns made of PS spheres like regular lattices cannot be efficiently manufactured without costly pre-patterned substrates. That is why this work focuses on natural HCP order. In the present work, EBE and RIE have been chosen to perform substrate patterning. During the EBE process, a material is deposited through gaps between spheres via thermal evaporation of the source. Inter-sphere voids constitute the honeycomb lattice. Therefore, most patterns manufactured by EBE through a PS mask are arranged in this particular manner. Using HCP nanospheres and shadow EBE, structures can be 'written' on a substrate. A few examples of honeycomb patterns are shown in figure 2.1. Namely, triangles (C1 - C3 and C1-D5), rods (C1 - F7), rings (C1 - E5), and combined structures like rings with dots inside (C1 - E6). Processing step E2 is a mask modification step, which reduces the size of mask interstices. The RIE process has several functions in SNSL. The first is the modification of spheres before subsequent EBE processing. This strategy creates a grid with spherical or elliptical meshes depending on the evaporation angle. At the grazing evaporation angle, oval meshes interconnect and become a pattern of parallel lines (C1 - B7). Secondly, RIE can be used to pattern a substrate directly. In this way, hexagonally arranged pillars were fabricated (C1 - A5). Honeycomb arrays of tips can be manufactured, by the use of a metallic mask in RIE processing (C1 - C5). Furthermore, apart from the hexagonal matrix, the PS spheres can be adsorbed on the substrate in a random order, but with controlled average spacing[14,15,26]. The above manufacturing routes are just a few examples. There is still great variety in the sets of combinations that are achievable.
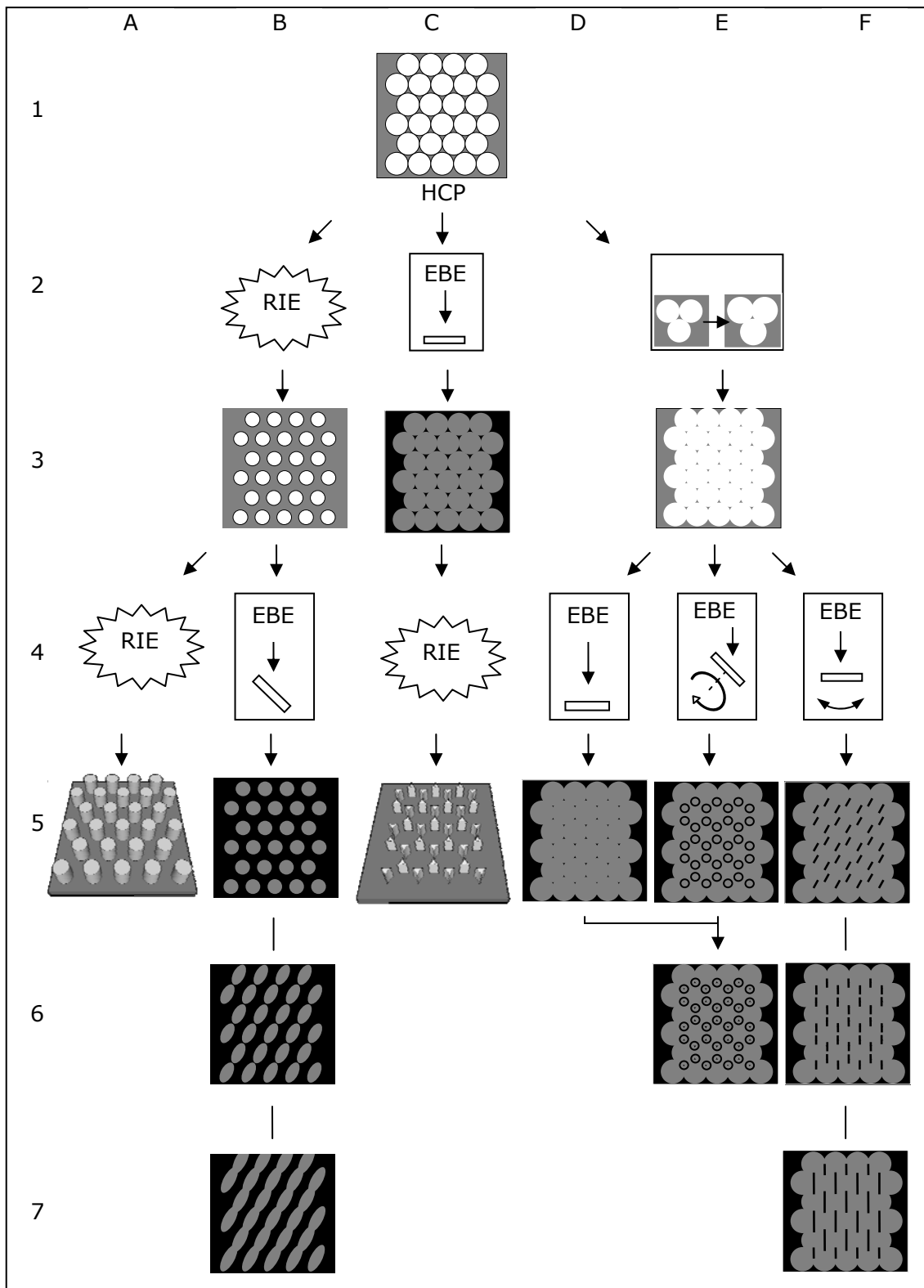
Figure 2.1. Schematic tree showing routes to achieve arrays of different nanostructures. C1) Colloidal PS mask on a substrate. B2, A4, C4) Reactive ion etching. C2, D4) Electron beam evaporation: perpendicular. E2) Aperture diminishing – process of decreasing interstices in the PS mask. B3) PS mask with etched spheres. C3) Substrate patterned with an array of triangles. E3) PS mask with reduced interstices. B4) EBE: perpendicular and at two other different angles. E4) EBE: at an incident angle close to orthogonal, with simultaneous rotation of the sample. F4) EBE: with

simultaneous changing evaporation angle (tilting). **A5) Substrate with patterned cylindrical pillars. B5, B6, B7) Evaporated grid with spherical meshes, elliptical meshes and interconnected meshes (i.e. wires), respectively. C5) Substrate with patterned prismatic pillars. D5) Substrate with an array of triangles similar to C3, but smaller. E5) Substrate with a template of rings. E6) Substrate patterned with an array of rings with dots inside. F5, F6) Pattern of rods differently oriented depending on the relationship of colloidal crystal orientation to the evaporation beam. F7) Interconnected rods on a substrate.**

2.2. Polystyrene mask preparation

The production of monodisperse colloidal spheres is already well-established on the market[53]. They can be made of diverse polymers in the size range of $10 - 10^6$ nm with various controlled physicochemical properties. Various nanospheres are available, with different surface functionalities, surface charges, protein-conjugations, magnetic coatings, and dyes. Complex chemical procedures and size separation techniques allow for the production of fractions with size distributions, reaching a coefficient of variation (CV); from 2% for larger particles (hundreds of nm), to over 10% for smaller sizes (tens of nm). The precise shape of the distribution curve is not known. Spheres are usually shipped in a water solution. Particles used in this work were PS micro or sub-micro spheres, also known as PS latex, with diameters ranging between 300 and 2000 nm. The assembly process takes a few seconds per square cm, during which 10^6 to 10^8, spheres are hexagonally arranged into the monolayer. Preparation of 2D colloidal crystals is the first technological step in SNSL. It involves interfacial self-assembly of nanospheres. The SNSL mask preparation procedure consists of seven major steps, described below. Experimental details are given in chapter 3.1.

1. **Application of colloidal solution on the water surface.** In the first step of preparation, it is important to trap nanospheres at the air-water interface. Only then, the spheres will be able to assemble into a big colloidal monolayer, required for further steps. A mixture of ethanol and PS-latex water solution is used for this purpose. After careful application of a PS solution onto the water, the liquid disperses over the interface. Some ethanol dissolves in the water, and some vaporizes from the water surface. What remains is the PS latex monolayer floating on the water. Eventually, some spheres also penetrate into the bulk of the water.

2. **Recrystallization.** When a monolayer is formed, due to the rapid and fluctuating process of self-assembly, it does not always yield large crystals. Augmentation of well-ordered crystals was induced by creation of water surface fluctuations via careful tilting of the vessel. Within this process, defected and multicrystalline parts of the colloidal crystal were rearranged into a single crystal. The suitability of a system to be recrystallized depends on the strength of the interactions between the spheres involved. The stronger the interaction, the more difficult the recrystallization is.

3. **Separation from a wall.** Interfacial monolayer upon contact with the wall of the beaker adheres to it. In order to manipulate a monolayer and to avoid structure damage in subsequent steps, it has to be separated from the wall.

4. **Increase of the density.** A monolayer is consolidated to assure close sphere packing and to avoid further structural changes. This step is done through introduction of surfactant molecules onto the water surface around the PS monolayer. Interface-adsorbed surfactant molecules induce pressure, which acts acting concentrically on the monolayer to consolidate it.

5. **Anchoring.** A floating and consolidated colloidal crystal is immobilized by anchoring at a beaker wall, to enable further (precise) deposition on a substrate.

6. **Substrate introduction.** Substrates have to be placed at the bottom of a beaker under a fixed monolayer. In the next step the removal of the water will lead to the deposition of a monolayer on substrates.

7. **Water removal, deposition on a substrate and drying.** The bulk water is removed from beneath a fixed colloidal crystal, until a thin layer between the substrate and the monolayer surface remain. The other water is left for self-vaporization and drying. After this process, samples are ready for further use.

2.3.   Interactions in colloids

Forces acting on colloids in solutions have been studied over several decades and are described in detail in the literature[54]. Despite the good understanding of individual forces in simple two-body systems, overall complex interactions in many-body systems are still too difficult to be precisely calculated, especially if long-range forces, i.e. acting on distances several times bigger than dispersed media, are involved. In order to distribute microspheres on the water, the PS-latex-water dispersion is mixed with ethanol. The reason for this is two-fold. Ethanol has about 79% of the density of water. Therefore, it is directed towards the water surface. Once the mixture reaches the surface, it is dispersed over a large area due to the amphiphilic ethanol molecules, which preferentially tends to cover the entire interface. Due to good solubility of ethanol in the water, some nanospheres might penetrate into the bulk water. In order to be trapped at the interface potential energy well, spheres should be hydrophobic. Immiscibility with water helps the spheres to be adsorbed at the interface and remain there. Once spheres reach the surface, they float from the application point towards the walls of a container. The behavior of spheres on the water surface, after deposition, is determined by the interaction potential of the spheres. The interactions of PS spheres at the interface arise due to attractive and repulsive forces and the interaction potential is determined by the sum of all potentials acting in the system (van der Waals, electrostatic, double layer, capillary etc.) The forces acting on the PS spheres are influenced by the following factors:

- Residual surfactant, initiator, monomer or other impurities, adsorbed on the PS latex after synthesis.

- Charge on the surface (i.e. type and surface density of functionalities on the PS sphere).

- The degree of diffusion of the dispersing medium into PS spheres.

- PS latex surface roughness.

- Ionic strength.

- Surface tension.

Since a detailed study of the above factors could not be performed due to the large number of parameters, the optimal suspension compositions were found for each specific batch of particles during numerous experiments.

Further preparation steps: recrystallization and increase of the density of monolayer, require the interaction potential to have; deep potential minimum, marked as primary minimum, and one big energy barrier (figure 2.2). The interaction potential presented in figure 2.2A has the secondary shallow minimum, which can trap a sphere weakly. The primary energy minimum is many times deeper than the Boltzmann energy k_BT at room temperature. Therefore, when

interfacial spheres approaching each other overcome the energy barrier between the two minima, they will experience strong attractions and coagulate.
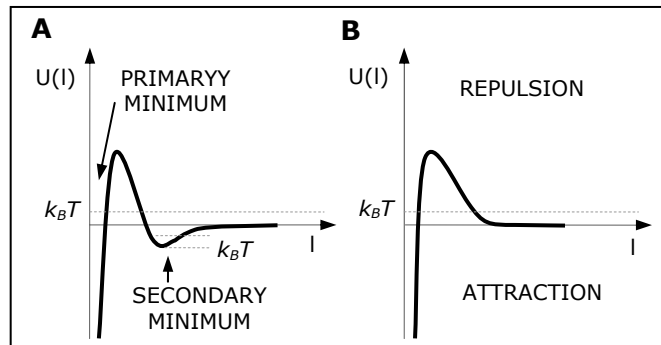
Figure 2.2. Examples of interaction energy potentials _U_ versus separation _l_ between two spheres trapped at air-water interface. A) Potential with two energy minima, B) Potential with one energy minimum. (k_BT is thermal energy at room temperature). Many similar interaction potentials are described in the literature[55] and references therein.

When spheres leave a pipette, they disperse over the air-water interface, evenly in all directions inside a beaker. This action is driven by the ethanol in PS solution dissolving in water and evaporating. A rate of diffusion depends on the amount of solution applied at a time onto air-water interface and on the diffusivity of ethanol in water. If spheres are to be arranged into a weakly bound colloidal crystal described by the interaction potential in figure 2.2A or a "two-dimensional gas of spheres" described by the interaction potential in figure 2.2B, the energy barrier in both cases has to be bigger than the kinetic energy carried by the momentum of the dispersing spheres. In case of interaction potential (A) floating spheres self-assemble due to attraction caused by the secondary shallow energy minimum creating loosely packed crystal. In case of potential interaction (B), floating spheres repel each other creating "2D gas of spheres" which can be compressed into a monolayer by continuous distribution of spheres until the entire area of the interface is covered. Such "stimulated ordering" is known as _Alder transition_[56]. Situations described by interaction potentials (A) and (B) are suitable for mask preparation, because the spheres can move relatively and rearrange themselves from multicrystalline structure into single crystal. If the energy barrier is surmounted by the PS spheres due to collisions and Brownian motion, they end up in a stable state described by the primary minimum. The monolayer is then multicrystalline and dense, and recrystallization step cannot be realized.

2.4. Polystyrene mask modification

As it was shown in chapter 2.1, reduction of the mask interstices is a key factor in SNSL manufacturing. Three different concepts, described in the following subchapters, have been contrived in order to decrease the size of the PS mask interstices: mask annealing, covering with silica, and surface dissolution.

PS mask annealing

The first concept for reduction of interstices in a PS mask, is to increase the temperature of the amorphous polystyrene spheres in order to increase the rate of polymer interdiffusion between spheres. Above the glass transition temperature T_g, thermal energy dominates cohesion of polystyrene. PS spheres in a mask start to exchange molecules, fusing with each other. Spaces between spheres begin to diminish and finally a mask collapses, forming a monolithic sheet of polymer with incorporated air blisters. Therefore, by choosing the appropriate temperature and

time of annealing, it is possible to control the degree of fusion. Polystyrene has a bulk glass transition temperature $T_g = 95$ °C, however this value should not be treated as a fixed and constant value, since the second-order phase transition is a smooth process. Additionally T_g depends on the molecular weight of PS, the degree of cross-linking, the surface-to-volume ratio of molecules in the sphere, impurities and the measuring method.

Three ways of heat transfer have been utilized here. First; by use of a heating plate, second; by utilizing hot air produced by an air gun, and third; microwave radiation. All these annealing techniques result in PS spheres melting together at contact areas.

PS mask coating with silica

A silica particle synthesis developed by Stöber and coworkers[57] was used for deposition of half-shells on PS spheres (figure 2.3). Recently, this method has also been applied to PS masks by Graf *et al.*[38]. The Stöber silica growth relies on hydrolysis of tetraethoxysilane (TES) catalyzed by ammonia in an ethanol solution. First, a silica precursor layer (1) is deposited in an EBE process on PS spheres (2) to promote the subsequent Stöber reaction and silica growth in activated areas. Details on the EBE process are presented in section 2.6. After EBE is accomplished, the PS spheres are half-covered with silica shells. Subsequently, a PS latex monolayer is introduced into a solution of ethanol/ammonia (for details see chapter 3.3). Addition of TES starts the Stöber reaction. The silica shell grows in previously evaporated selected areas (3). After deposition of silica, the apertures in the PS mask are reduced from their initial size A_0 to A_1.
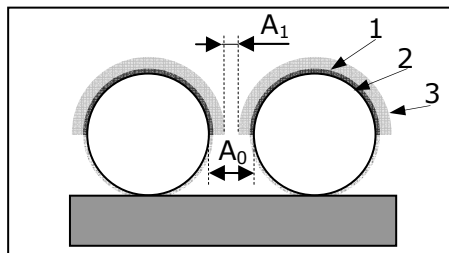

Figure 2.3. Schematic sketch of a PS mask covered with a silica layer. 1) Silica precursor layer, 2) PS sphere, 3) silica layer grown using the so-called Stöber process. Here, A_0 and A_1 are initial and final aperture sizes respectively.

PS mask surface-dissolving

The third method relies on partial dissolution of the PS latex in a vapor of organic solvent. A sample is placed under a glass cover together with a source of organic vapors, as shown schematically in figure 2.4A. The mask absorbs solvent from the air, because polymer chains in the sphere adhere stronger to the solvent molecules than to each other, and the mask becomes softer. This in turn allows spheres to exchange molecules at contact areas with neighboring spheres. Unfavorable large surface energies of spheres are minimized. As a consequence, mask interstices diminish as indicated with black arrows in the cross-section scheme 2.4B.
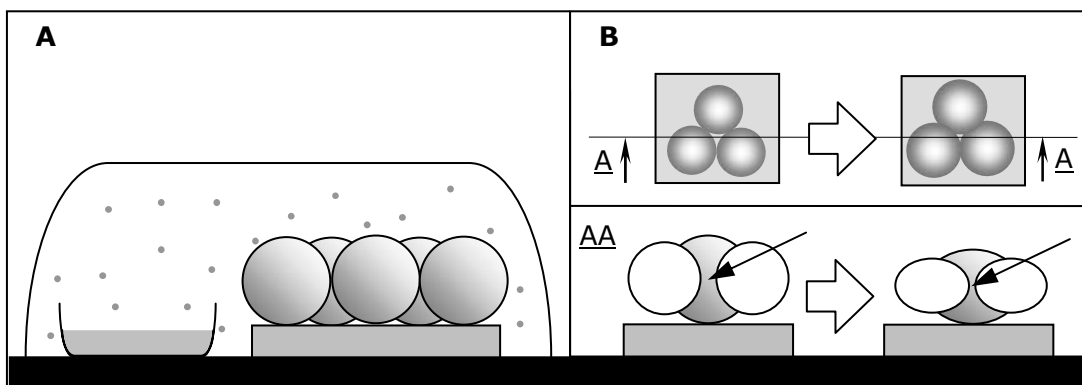
Figure 2.4 Vapor exposure of a PS mask. A) The colloidal mask on a substrate placed near a beaker containing organic solvent. B) Scheme of the mask before (top-left) and after (top-right) exposure to solvent vapors. Line AA indicates the cross-section plane. Bottom: cross-section of the mask showing shape change. Black arrows indicate aperture size before (left) and after (right) treatment.

A carefully chosen duration time of sample exposition to vapor allows for a controlled change of apertures in a mask. After a too long period, the mask will collapse forming a continuous layer of PS.

2.5. Reactive ion etching

The RIE technique uses an alternating electrical field to dissociate and ionize neutral gases. Upon collision with ions accelerated by the electric field, molecules fracture into radicals. Overall, the plasma contains various kinds of particles. Besides positive and negative ions, there are radicals and neutral molecules, excited species, and photons. Oscillating ions are responsible for mechanical bombardment, called physical etching or sputtering, for heat transfer and partially for chemical etching. Chemical etching is caused predominantly by the highly reactive, neutral radicals, which diffuse to all surfaces in a chamber and react with them. Therefore, chemical etching is rather isotropic contrary to directional, physical etching. Volatile by-products of the reaction are removed from the chamber by a vacuum pump. In the RIE process, important controllable parameters are the gas composition, plasma energy, pressure, and flow rate of reactive gas as well as the processing time. Details about the RIE technique can be found in the literature[58]. As shown in figure 2.1, RIE is used in this work for two purposes. First to decrease the size of PS spheres (C1 – B3), and second to transfer a pattern from a mask to a substrate (B3 – A5, C3 – C5).

Etching of a PS latex mask is done by oxidation of PS through oxygen plasma treatment.
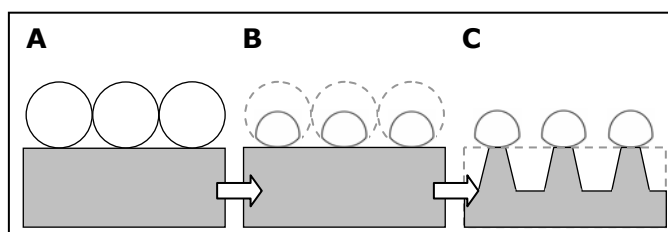
Figure 2.5. Schematic profile evolution through two, different RIE processes. A) Substrate with mask. Following, expected etch-profiles for: B) PS etching by O_2 plasma and C) subsequent Si etching by SF_6/O_2 plasma.

Due to the physicochemical etching nature of the RIE, the PS mask shown in figure 2.5A, attains after processing the shape shown in figure 2.5B. For structuring of a silicon substrate, a mixture of sulfur hexafluoride and oxygen provides efficient etching. Due to the presence of oxygen, spheres are etched simultaneously with silicon, which results in sloped sidewalls of Si pillars (figure 2.5C)

2.6.   Metal deposition

The following section is about the geometrical relationships between a mask and nanostructures. First, general EBE requirements for SNSL are discussed. Then, the applied evaporation processes and their resulting nanostructures, shown schematically in figure 2.1, are described.

2.6.1. General shadow nanosphere lithography requirements for evaporation system

Electron beam evaporation (EBE) is a deposition technique based on vaporization or sublimation of a source medium. Released atoms travel through a vacuum on straight trajectories and deposit on the sample. The EBE setup used in this study has two important characteristics:

First; the source of evaporation is smaller or comparable to the size of a sample. The distance between sample and source is much bigger than the distance between PS mask apertures and the substrate. In this arrangement, trajectories of atoms are considered as parallel. Only as such, can they be applied for localized patterning, whereas rays coming from all directions would cause material deposition in every possible area of the substrate. Deposition with a parallel beam is therefore essential for SNSL.

Secondly; atoms are emitted by a source in all directions. Hence, the thickness of the layer evaporated on the substrate is proportional to the inverse of the squared distance of sample to a source. When a substrate is being evaporated at an incident angle θ different from 0, then one side of the sample is closer, and the other is farther, from the source. For this reason, the deposition at short sample-source distance results in thickness variance on opposite sides of a sample. Keeping the evaporation distance large in comparison to the sample size minimizes thickness inhomogeneities.

The main idea of the shadow mask is to exploit the "active area" of the PS mask located within a half-sphere diameter distance $D_0/2$ from the substrate. Figure 2.6A shows a mask deposited on a slab. Figures 2.6B-C shows a cross-section of the mask from figure 2.6A. Separation $D_0/2$, unlike conventional masks, is a consequence of the employment of spheres as building blocks of a mask. Deposition of material through a distant mask gives the possibility to "write" arbitrarily shaped features on a substrate, by changing the angle of evaporation. This mechanism is effective only if point sources with parallel beams are used for the deposition, such as electron beam evaporation. It is important to notice that the width of the writing beam, as well as the amount of material reaching a substrate, are dependent on the deposition-angle. Beam y in figure 2.6C is narrower than beam x. Consequently, particle X is thicker and wider than particle Y.
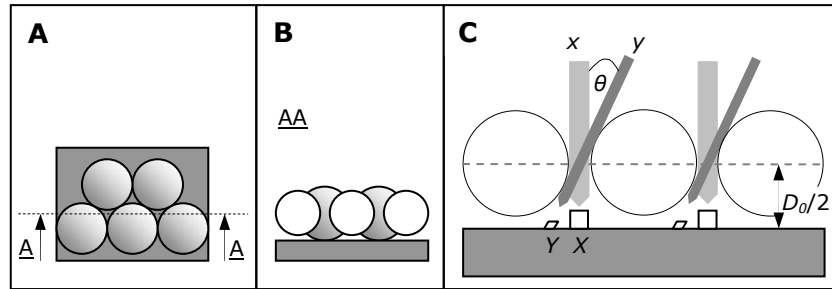
Figure 2.6. The idea of the shadow approach of nanosphere lithography. A) Colloidal crystal (mask) deposited on a substrate with indicated cross-section line – *AA*. B) The cross-section view of the mask, along the *AA* line from figure (A). C) Simplified scheme of B, showing deposition of material through the mask. Note that beam y delivers less material to the substrate than x. Additionally particle Y is deposited at an angle other than the right angle and as a result is inclined in contrast to particle X. Here *θ* is the angle of incidence.

The maximum size of each nanostructure made by SNSL is restricted spatially by spheres surrounding an aperture. In addition to the purely geometrical restrictions of the system, it must be noted, that each gap between spheres will decrease progressively, due to deposition of incoming material on the edges of the aperture. This process is shown in figure 2.7A. As evaporation proceeds, in one moment all gaps will be completely closed by the deposited material. This has two implications; first, evaporated particles are wider at the bottom and narrower on the top – figure 2.7B. Second, the amount of material that can pass through a gap is limited and so is the thickness of the nanostructure.
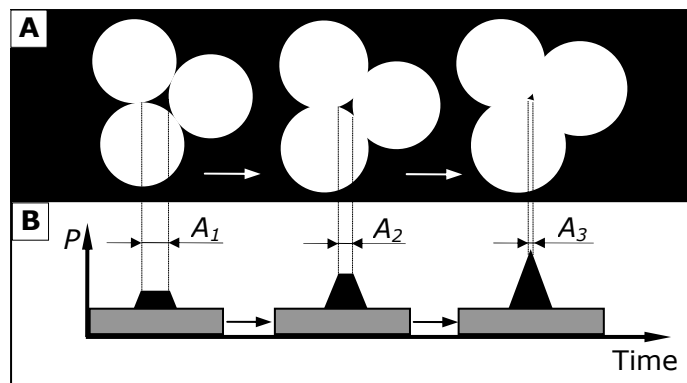
Figure 2.7. A) Progressive reduction of mask apertures $A_1 > A_2 > A_3$ during evaporation. B) Increasing thickness P of particles, evaporated on the substrates at three progressive stages of evaporation.

2.6.2. Grazing angle evaporation with rotation

In section 2.4 it is shown that before the silica overgrowth procedure is applied, spheres are covered with a hemisphere of silica precursor using EBE. Such deposition was accomplished by evaporation at a large angle $θ$ ($\approx 80 - 85°$) – figure 2.8.
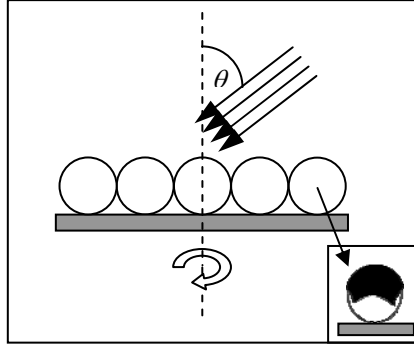
Figure 2.8. Preparation of a precursor hemisphere for further silica-shell growth. The evaporation (indicated by arrows) of the silica activation layer is done at an incident angle θ, while constantly rotating the sample around the rotation axis indicated by the dashed line. The inset shows the shell (black) evaporated on a sphere (white). The spiky edges arise due to shadow created by neighboring spheres during deposition.
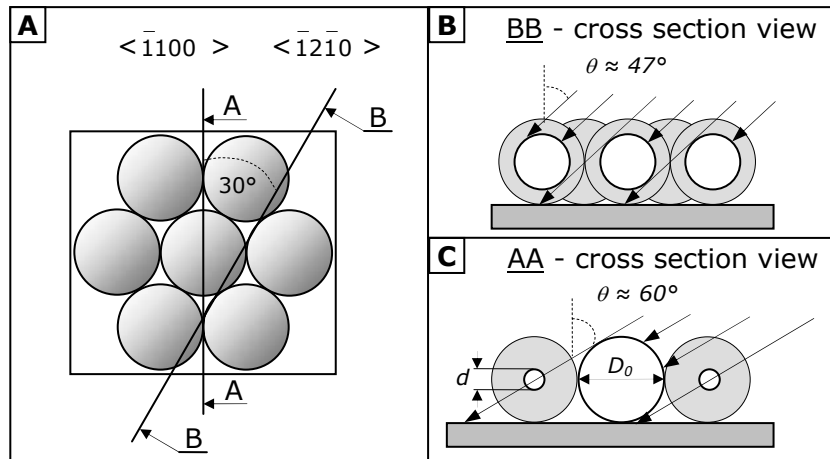
Rotation of the sample during evaporation ensures that the spheres are covered from all directions. The resulting silica cup on top of the spheres has a shape close to the one shown in the inset of figure 2.8. The reason for application of a large θ angle is the protection of the substrate from being coated with silica. Image 2.9A shows crystallographic directions of the considered crystal in Miller-Bravais notation. The minimum θ angle is estimated by analysis of two extreme situations shown in figure 2.9A, which are exchanging periodically every 30° during rotation. The critical angle θ for evaporation along $<\bar{1}2\bar{1}0>$ direction (figure 2.9A, B) is described by equation 2.1.

$$\theta = \arccos(\sqrt{2\sqrt{3}-1}) \approx 47° \qquad\qquad \textbf{2.1}$$

Evaporation through a PS mask along $<\bar{1}2\bar{1}0>$ direction of the crystal, at angles θ larger than ≈ 47° will not pattern the substrate. When the evaporation direction changes from $<\bar{1}2\bar{1}0>$ to $<\bar{1}100>$ (figure 2.9A, C), then the critical angle is described by equation 2.2. For θ angles larger than those depicted in scheme 2.9C, no material is going to be deposited on a substrate. However, there is one exception to these equations, which is described later.

$$\theta = \arccos(\frac{1}{2}(\frac{d}{D_0}+1)) \qquad\qquad \textbf{2.2}$$

The parameter d is the effective diameter of the contact area between two spheres. From equation 2.2 it follows that for d values close to 0, θ approaches 60°. Therefore, for evaporation angles, which are larger than 60°, deposition on a substrate does not occur. In reality, the diameter of the contact area d is much bigger (d ≈ (0.1 − 0.25)D_0) than a point contact (d = 0), which implies that in this direction even smaller angles θ could be used.

Figure 2.9. Mechanism of evaporation at angle θ during continuous rotation of the sample. A) Notation of Miller-Bravais indices. B) Cross section view along BB line in (A). The critical evaporation angle below which substrate will be structured during evaporation along $<1\bar{2}\bar{1}0>$ direction is $\approx 47°$. The critical evaporation angle below which substrate will be structured during evaporation along $<\bar{1}100>$ direction is $\approx 60°$.

The previously mentioned exception to the above is that along $<1\bar{2}\bar{1}0>$ directions, deposition is possible for θ approaching 90°. Figure 2.10 shows a mask from the source point of view. A substrate at this orientation can theoretically be patterned.
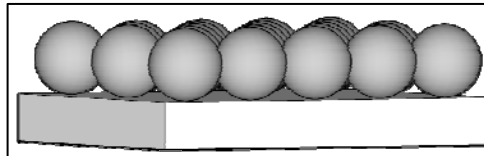
Figure 2.10. View along the direction almost parallel to the $<1\bar{2}\bar{1}0>$ direction, showing the three-dimensionality of the PS mask. Between the substrate and the spheres, clearances are visible, through which atoms from the source can penetrate the mask and deposit on the substrate, or even move across the sample.

The dependence of the penetration length on the angle θ along the $<1\bar{2}\bar{1}0>$ direction is given by:

$$n = \frac{\tan\theta}{4}$$

2.3

where n is the length counted from the edge of a sample, expressed in the number of spheres. For example, for a typical value of $\theta = 85°$ used for the silica coating procedure, $n = 2.9$ spheres. Thus for samples of 1 cm size, the phenomenon of high θ evaporation penetration can be omitted.

The next feature (described below) is important not only for silica overgrowth, but also for non-zero-angle, or rotation-evaporated nanoparticles. It is the difference between the thickness of the material emitted by a collimated source and the thickness of the material deposited on a moving substrate. In the case shown in figure 2.11, the fact that a sample was evaporated from one direction, caused exposition from just one side, whilst the other side remained in shadow. The

thickness and morphology of the shadow-evaporated layer depends on the surface curvature and relative motion of the sample and source. For simplification of the explanation of the rotational deposition, the following example is considered. Figure 2.11A shows a "2D sphere" on which a layer of material was deposited by a collimated source. If the thickness to be deposited was set to P_0, then the total amount expressed in surface units is $P_0\pi D/2$ for a stationary substrate. When the rotation is applied, the amount of material will remain constant, but the layer will become homogeneously distributed around the circle (figure 2.11B).
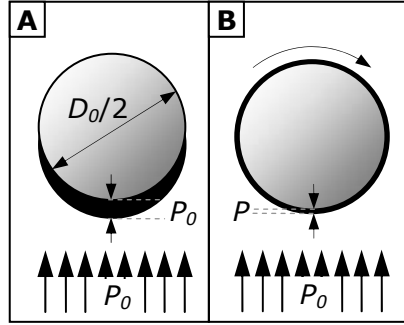
Figure 2.11. Schematic of evaporation of material on a sphere A) without and B) with rotation. Here D_0 is the diameter of the sphere, P_0 is the set value of deposit thickness, and P is deposit thickness on a rotating sphere.

Simplified calculation of the thickness P in the rotating case leads to a consecutive formula:

$$P = \frac{D_0}{2}\left(\sqrt{1 + \frac{4P_0}{\pi D_0}} - 1\right) \qquad \textbf{2.4}$$

The thickness P for values of $D_0 = 500$ nm and $P_0 = 30$ nm is equal to 9.4 nm. Equation 2.4 describes the thickness in the area where the incident beam is orthogonal to the sphere surface. The thickness of a deposited layer on the sides of a sphere, where the incident beam is non-orthogonal to the surface, is less. Equation 2.4 gives an approximate value of the thickness of a deposit in the rotational evaporation process.

2.6.3. Perpendicular evaporation

Evaporation at an angle $\theta = 0°$ through a 2D HCP PS latex mask results in the formation of triangular particles with concave walls. For simplicity, this shape is called "triangle" throughout this work. The size of triangles depends on the size of apertures in the mask. These in turn depend on the diameter of the spheres used D_0, and on the aperture decreasing process. For particles shown in figure 2.12A, in-plane-height h_p is:

$$h_p = \frac{D_0\sqrt{3} - 1}{2} - \frac{d}{2} \approx 0.366D_0 - \frac{d}{2} \qquad \textbf{2.5}$$

Theoretically, the h_p value depends only on D_0. however, the spheres do not have a point, but contact area of finite size d. Therefore, the second term $d/2$ has to be taken into account. For the same reason, the real surface coverage SC_{real} of triangular particles is smaller than that theoretically predicted (0.093):

$$SC_{real} < \left[1 - \frac{\pi\sqrt{3}}{2} \approx 0.093 \right]$$ **2.6**
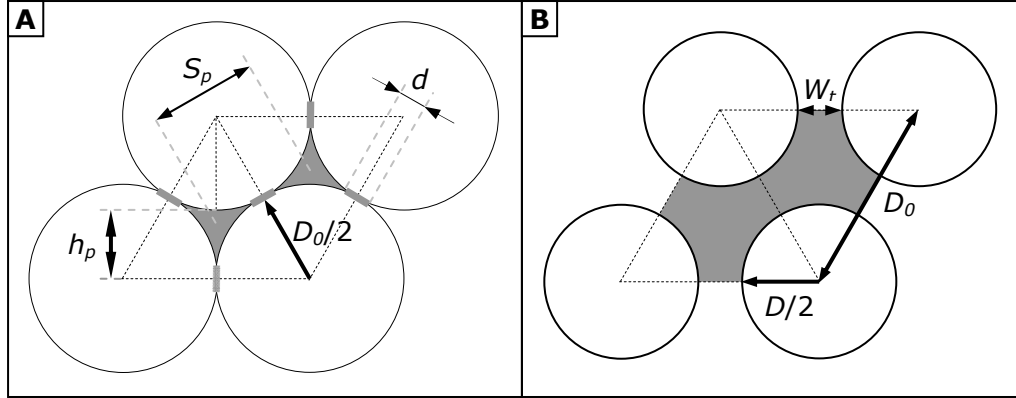
Figure 2.12. Geometry of structure for evaporation at $\theta = 0°$ through 2D HCP mask, A) before additional mask processing; B) after RIE. Here D_0 is the sphere diameter, d is the diameter of the contact area between spheres indicated in grey, h_p is the triangle height (in-plane size of the triangle), D is the etched sphere diameter, and W_t is grid wall thickness.

Spacing S_p of two neighboring triangles depends on D_0:

$$S_p = \frac{D_0}{\sqrt{3}} \approx 0.577 D_0$$ **2.7**

In the case of RIE processing of the mask, and subsequent perpendicular evaporation, the previously triangular particles will become interconnected, forming a grid (figure 2.1B5). In such a case, the wall thickness W_t between two holes in the grid presented in figure 2.12B is equal to the difference between diameters of a sphere before, and after RIE:

$$W_t = D_0 - D$$ **2.8**

where D is the diameter of an etched sphere. The surface coverage for a grid is given by:

$$SC = \frac{D_0^2 \sqrt{3} - \dfrac{\pi}{2D^2}}{D_0^2 \sqrt{3}}$$ **2.9**

For all structures mentioned in this paragraph, the thickness P in the direction perpendicular to the plane of figure 2.12 is equal to the amount of material set for evaporation P_0.

2.6.4. Non-perpendicular evaporation

Evaporation at non-zero incident angles through the etched spheres yields nanostructures like elliptical-mesh grids and parallel lines, if EBE is realized along the $<1\bar{2}\bar{1}0>$ crystal directions. A bare substrate, seen between spheres, indicates that the evaporation from this viewpoint creates a grid with spherical or elliptical gaps - figure 2.13A, B. If the incident EBE angle is large enough, spheres will cast shadow over each other, and periodic parallel lines will deposit on the substrate between spheres (figure 2.13C). To achieve this, the incident angle θ has to follow the simplified formula:

$$\theta > \arctan \frac{D_0}{D} \qquad \qquad \textbf{2.10}$$

The length of the wires depends on the quality of a crystal – the number of defects and the homogeneity of crystal alignment.
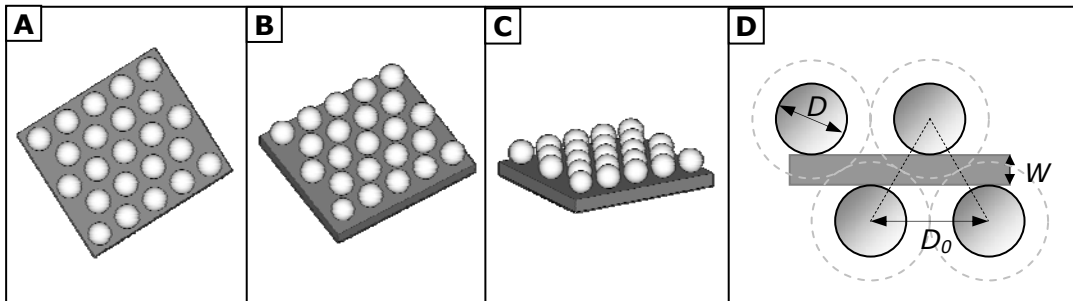
Figure 2.13. Substrate covered with etched spheres aligned with $<1\bar{2}\bar{1}0>$ direction (vertical edge of the image), positioned at three different incident angles θ. Evaporation from presented viewpoints results in fabrication of: A) a spherically meshed grid, B) an elliptically meshed grid and C) periodic parallel lines. D) Scheme of the line evaporated between spheres. Width of the the line W is related to the diameter of spheres before and after etching D_0 and D respectively. The minimum value of the diameter of etched spheres allowing line manufactureing is $D < 0.86D_0$.

According to the dimensions shown in figure 2.13D, the width W of the lines is:

$$W = \frac{D_0 \sqrt{3}}{2} - D \approx 0.866D_0 - D \qquad \qquad \textbf{2.11}$$

The fact that the W value cannot be negative yields the etching condition for preparation of nanowires: etched spheres must have a diameter smaller than 0.86 of the original size. Approximated surface coverage of lines is given by:

$$SC = 1 - \frac{2D}{\sqrt{3}D_0} \qquad \qquad \textbf{2.12}$$

Thicknesses of structures evaporated at non-zero θ, follow the formula:

$$P = P_0 \cos \theta \qquad \qquad \textbf{2.13}$$

Spacing S_p of lines in an array is given by:

$$S_p = \frac{D_0 \sqrt{3}}{2}$$

2.14

The above calculations are derived for a simplified 2D model. As such, they do not describe line corrugations such as those presented in figure 2.13C.

2.6.5. Evaporation with tilting

Periodical tilting of a substrate during the evaporation process creates an array of rods (figure 2.1F). The size of these rods depends on the range of the tilting angle θ, on the size of the apertures in a mask, and on the orientation of the colloidal crystal in relation to the EBE beam direction. Figure 2.14 presents the scheme of a mask on a slab (A), and four examples of rods (B-E). These can be achieved by EBE on a substrate, tilting from θ to - θ, along the directions given below each image and indicated with a line in the bottom left corner of each image. In figure 2.14D the size of the nanorods is almost twice as big as that of rods in 2.14C. For large changes of θ during tilting, the neighboring particles can overlap and merge. Such structures arise when deposition along the $<\bar{1}100>$ direction occurs. This feature can be used further for preparation of zigzag nanowires, shown in figure 2.14E. To achieve this, two evaporation steps have to be performed: one in $[\bar{1}100]$, and the second in $[01\bar{1}0]$ direction. Other pairs of directions are also feasible, and these examples are given below.
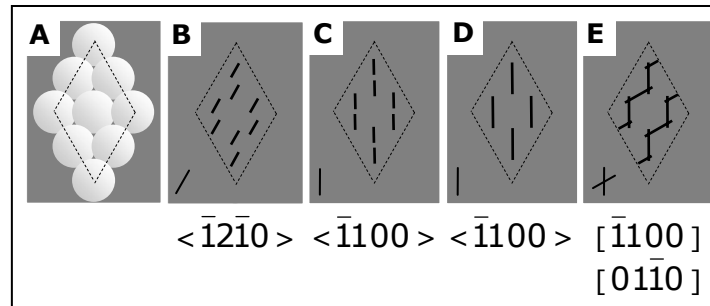
Figure 2.14. A) Sketch of a PS-latex mask on a substrate. B-E) Examples of rods on a substrate. Below the images the writing directions are indicated along which a crystal has to be continuously tilted during the EBE process in order to achieve the corresponding structure.

The thickness of rods is mostly affected by the aperture-size-restricted flux of the vaporized material. Thus, it can be approximated as a function of the diameter of an aperture A_0 and length of a rod L_0:

$$P = \frac{P_0 A_0}{L_0}$$

2.15

However, the profile of rods is expected to be thicker in the middle and thinner at both ends of the rod. There are two reasons for this phenomenon. First; the deposited thickness for non-perpendicular evaporation shrinks with θ (equation 2.13) and secondly; the effective aperture size A_e, depends on the angle θ, the initial aperture size A_0, and the thickness of the aperture T, as is described by the following equation:

25

$$A_e(\theta) = A_0 \cos\theta - T\sin\theta \qquad\qquad \textbf{2.16}$$

Where T is the thickness of an aperture, as indicated in figure 2.15.
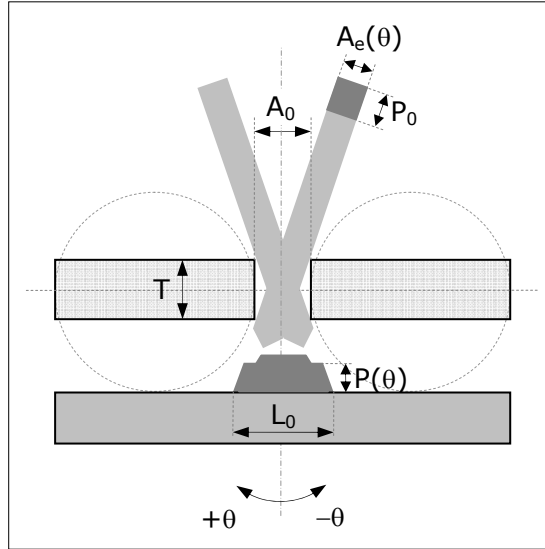
Figure 2.15. Scheme of an aperture in a PS mask approximated with rectangular gap. Tilting the substrate from + θ to - θ creates rods of length L_0. The effective size of the aperture depends on θ. The final thickness profile P(θ) is drawn schematically.

Substituting A_0 from equation 2.15 with $A_e(\theta)$ from equation 2.16, and scaling the whole expression using equation 2.13 gives a more precise value of the thickness profile function along the axis of the rod:

$$P = P_0 \cos\theta \frac{A_0 \cos\theta - T\sin\theta}{L_0} \qquad\qquad 2.17$$

The width of nanorods is equal to the value of A_0. The spacing of two closest nanoparticles, presented in figure 2.14B and C, is identical to the spacing of triangles calculated previously, i.e.: $Sp = D_0/\sqrt{3}$.

2.6.6. Non-perpendicular evaporation with sample rotation

EBE of a tilted and rotating substrate with the PS-latex mask allows for preparation of ring-shaped or cup-like particles. These particles are arranged in the same order as triangles and rods – in a honeycomb lattice. The thickness of rings can be approximated using a formula analogous to that used for the rod-like particles:

$$P = P_0 \cos\theta \frac{A_0 \cos\theta - T\sin\theta}{C_0} \qquad\qquad \textbf{2.18}$$

C_0 is the average length of the circumference of a ring-shaped particle. The outer and inner diameters of the ring depend on the incident angle θ and the size of the apertures A_0. In certain conditions – like for small θ, and large A_0 – rings can

become disks. Changing the incident angle during rotation and evaporation would produce a spiral particle.

Detailed calculations of the described formulas are attached in chapter 8.3. It should be emphasized that these estimations are based on simplified models. They do not take into account such effects as change of sphere dimensions during the time of evaporation or the fact that atoms arrange into nanocrystals and that the nano-scale structures cannot be treated as a continuum.

3. Methods of Nanofabrication and characterization

3.1. Substrate preparation

SNSL is compatible with a wide variety of substrates. The substrates used within this work are Si (100), Si (111), Al_2O_3 a-plane, $LiNbO_3$, and SiO_2 (BSG). Wafers are cut into 10x10 mm or 9x9 mm pieces. After dicing, substrates are pre-cleaned by three minutes ultrasonication and rinsing with 2-propanol. Following this, the substrates are submerged for 30-60 minutes in a standard cleaning solution (SC1)[59] of 7% NH_4OH/30% H_2O_2/Milli-Q water (vol. ratio 1:1:5) at 80 °C, then rinsed thoroughly in Milli-Q water and finally dried in a stream of argon.

3.2. Polystyrene mask preparation

Various polystyrene (PS) solutions are tested for buoyancy on water and positive candidates are used for further experimentation. For convenience, PS solutions will be denoted analogous to the example: "PS 470 nm", which stands for "dispersion of PS spheres having a diameter of 470 nm". Adsorption of PS spheres from the deposition solution to the water interface is spontaneous. In the case of PS 470 nm, the dispersion buoyancy is improved by addition of sulfuric acid and in the case of PS 540 nm dispersion, by centrifugation and partial removal of water from the stock solution. The ability of PS solutions to cover the interface is driven by diffusion of ethanol to the air-water interface and it is controlled by ethanol content. Stabilization of spheres trapped at the interface against aggregation is assured by electrostatic repulsion, between the native charges resulting from hydrolyzed sulfate groups on the spheres, and by steric stabilization through the addition of styrene.

Seven different sizes of PS spheres are chosen for mask fabrication. All PS latex solutions are prepared using materials received from the manufacturer without any additional treatment, unless stated.

- Preparation of PS 127 nm solution: 10 wt. % aqueous dispersion of PS latex 127 nm, is mixed in vol. ratio 1:1 with ethanol.

- Preparation of PS 470 nm solution: 10 µl of H_2SO_4 (98%) is mixed with 1 ml of 1 vol. % of styrene in ethanol. 10 µl of prepared solution is added and blended with 290 µl of the 1 vol. % styrene in ethanol and then mixed with 300 µl of the 6.9 wt. % aqueous dispersion of PS 470 nm suspension.

- Preparation of PS 540 nm solution: 8 wt. % aqueous dispersion of PS latex 540 nm, is centrifuged and concentrated to about 30% in water. Then the suspension is mixed in vol. ratio 1:1 with ethanol.

- Preparation of PS 980 nm solution: 8 wt. % aqueous dispersion of PS latex 980 nm solution, as received, is mixed in vol. ratio 1:4 with ethanol.

- Preparation of PS 1710 nm solution: 10 wt. % aqueous dispersion of PS latex 1710 nm, is mixed in vol. ratio 1:1 with ethanol.

- Polymethyl methacrylate (PMMA) 1060 nm solution: 10 wt. % aqueous dispersion of PMMA 1060 nm, is mixed in vol. ratio 1:1 with ethanol.

Mask fabrication is carried out in standard glass Petri dishes with diameters between 10 and 20 cm and a typical height of 2-3 cm. Prior to use, dishes are cleaned in ethanol or 2-propanol and rinsed in Milli-Q water. A distribution pipette,

with a curved ending and modified outlet, is created by shaping a standard disposable glass pipette using a flame burner. The initial size of the outlet of the pipette (1 mm) is decreased to about 0.1 – 0.5 mm. The curvature of the pipette is aimed to direct the flow of suspension against the direction of gravity – figure 3.1A. The size of the outlet is optimized for the most convenient application rate compartment, in which the flow of suspension had to be operated. After the experiment, pipette cleaning is done by ultrasonication and rinsing in 2-propanol followed by drying in a stream of argon.

A pre-cleaned Petri dish half-filled with Milli-Q water is placed under a lamp, on a black background, facilitating good visibility of the monolayer during preparation. About 0.5 ml of PS dispersion is drawn into the glass pipette with a curved ending, and distributed on the water surface. The position of the pipette with respect to the water level influenced the flow of the PS solution and is kept as shown in figure 3.1B-D. The pipette position is chosen in order to achieve a laminar and steady flow of PS solution. Additionally, the application rate is regulated by changing the air rate being sucked into the pipette upon hydrostatic pressure created by the liquid inside. The transfer of the PS suspension is stopped when the monolayer covers about 60 - 70% of the water surface. At this point, the particles are usually arranged into a colloidal multicrystalline monolayer, visible by a mixture of iridescent colors. If the particle-particle interaction at the interface is weak enough to allow relative movement of spheres (corresponding to secondary minimum from figure 2.2A, a recrystallization procedure could be started. During this step, tilting of the glass vessel is done until fine waves of water ($\lambda \approx 3 - 15$ cm, amplitude <1 cm) made the crystals grow large enough to cover the Si pieces.
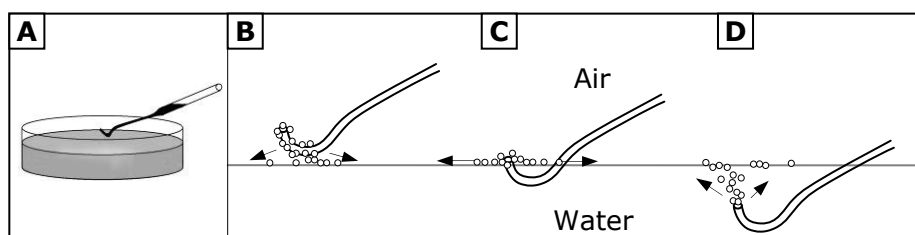
Figure 3.1. A) Distribution of PS dispersion on water substrate. B) Distribution with the pipette touching the water surface. C) Distribution with outlet of the pipette touching the water surface. D) Deposition from bulk water.

Tilting movement is generated by hand. About 30 minutes of such recrystallization leads to significant improvement of the monolayer. Eventually, small areas with defects or contamination within the monolayer can be removed using a pipette attached to the suction pump. In such cases, the removed area is immediately replaced by surrounding spheres. Once recrystallization is finished, the monolayer is carefully separated from the vessel wall by insertion of silver wire wetted by a solution of Triton X-100 all along the beaker wall. During each insertion, surfactant molecules entering the water surface create a front of different surface energies that disperses concentrically from the wire. Consequently, the energy front pushes the spheres away, breaking the crystal apart. Finally, the crystal is liberated from the beaker wall. Further surfactant introduction results in consolidation of the monolayer, since the free water surface is being reduced, as it had to be shared between the monolayer and Triton X-100 molecules. Now the spheres are pushed closer together, therefore entering the primary interaction energy minimum (figure 2.2A) and creating a stable crystal. Subsequently, the monolayer is anchored on the wall of the beaker: the colloidal crystal is pushed towards the wall of the vessel, and a small amount of water is drained from the vessel reducing the water level and resulting in deposition of a monolayer on the beaker wall. The driving force for the monolayer movement is removal of surface-adsorbed Triton X-100 molecules

on one side of the monolayer, using the suction pump, and simultaneous addition of fresh molecules on the opposite side of the monolayer, using wire wetted by Triton X-100. Then, the desired substrates are submerged in the water and aligned under the PS monolayer. To protect the substrate surface from unnecessary adsorption of contaminants from the water surface, slabs are coated with droplets of clean water prior to insertion. The deposition from the air-water interface to the substrate is realized by a two-step water removal. Most of the water from the beaker is pumped out slowly (about 10 ml/minute), until the water surface began to "bend" at the substrate edge. The rest of the water is evaporated overnight at a temperature of $\approx$ 26 °C. Some samples required the colloidal crystal direction to be aligned with regard to the evaporation direction e.g. for preparation of lines. Orientation of the colloidal crystal is revealed by creating a diffraction pattern upon illumination with laser light. Displayed diffraction spots are analyzed and the crystal orientation is determined. The marked direction is later aligned with respect to the evaporation direction in the evaporator.

3.3.   Polystyrene mask modification

PS mask annealing by a heating plate

During the usual annealing process, the substrate is placed on a Si wafer, located on the heating plate. Thermal conductivity between the heating plate, and Si wafer is improved by use of a thin layer of silicon oil. The whole setup is covered with a polymer cover tha a small window to improve heat stability. The temperature of the process is monitored via a thermocouple adhered to the Si wafer and covered with a piece of Al foil to reduce uncontrolled fluctuations. After an annealing period, the samples are placed on the laboratory bench to cool down. Annealing periods are in the range of tens of seconds, and temperatures are between 100 and 150 °C.

PS mask annealing by air gun

For air-gun annealing the setup consists of a Si wafer support, with an air gun placed above, and a room temperature argon dispenser located below the wafer. The stream of hot air used for PS fusion is adjusted between 70 and 140 °C as measured by a thermocouple placed next to the sample. The Ar dispenser provides cooling of the sample via heat sinking through the Si wafer support. After fusion is complete, the sample is left to cool down.

PS mask annealing by microwave irradiation

The samples are inserted into a 25 ml water/ethanol/acetone mixture (vol. ratio 3:1:1), in a glass beaker. Clean water proved to be an inconvenient medium, since high surface tension caused mask desorption. Submerged samples are exposed to microwave radiation (2450 MHz) in a commercial 1200 W microwave oven operated at full power. The time of annealing is measured from the moment at which the liquid achieves the boiling point. After this point, the sample is removed from the beaker and dried.

PS mask coating with silica

PS masks are evaporated with 20 – 30 nm of silica at 0.2 – 0.3 nm/s and at an incident angle of θ = 80 – 85°, with sample rotation turned on. Evaporation of 20 – 30 nm of material on spheres of 500 nm in diameter corresponds to 6.3 – 9.4 nm thick shells deposited on spheres, according to equation 2.4. In all SiO_2-coating processes, substrate pieces with masks covered with a silica precursor layer are submerged into 20 ml of 4.2 vol. % of NH_4OH (28 wt % in water) in ethanol in a

PS vessel. Then, 200 µl of 10 wt. % of tetraethoxysilane in ethanol is added, slightly mixed and left for various incubation periods. Subsequently, the samples are rinsed with ethanol and dried.

PS mask surface dissolving

Solutions of tetrahydrofuran (THF) and acetone (vol. ratio 1:2) or THF and ethanol (vol. ratio 1:4) are used. According to chapter 2.4 the samples and vessel containing the mixture are covered with a Petri dish in ambient conditions (i.e. RT) and held for various periods. After treatment, samples are ready for further use.

3.4. Reactive ion etching

RIE is realized using a Multiplex Atmospheric Cassette System from Surface Technology Systems. PS spheres are etched using a 30 – 150 W RF power plasma at a pressure of 60 – 100 mTorr. Etching compositions include the following gases: argon, carbon tetrafluoride, sulfur hexafluoride, and oxygen. The electrodes in the aforementioned etching reactor are in parallel-plate configuration.

For Si etching, in pillar preparation, deep RIE is realized by an inductively coupled plasma (ICP) etcher using "Bosch" process[58]. The "Bosch" etching process consists of two, periodically exchanging stages: etching and passivation. During the passivation stage, sidewalls of the pattern are being coated with a thin polymer layer, which protects the structure from etching in the subsequent etching stage. In this way, it is possible to etch very deep structures having vertical sidewalls. In this processing sulfur hexafluoride, gas is used for silicon etching and octafluorocyclobutane is used for passivation.

3.5. Electron beam evaporation

Evaporation processes are done using a modified e-beam evaporator, BAK 640, from Unaxis, Switzerland (currently Oerlikon Corporate). Since the aforementioned evaporator is a high-throughput system, it has an umbrella shaped holder for 24 wafers, presented in figure 3.2A. Such a setup could not provide the necessary sample position control, therefore a separated rotation holder is designed for SNSL purposes. Rotation holder presented in figure 3.2B is designed[60], assembled and introduced into the chamber via a sidewall vacuum flange (shown in figure3.2C). A stepper motor attached to the outer shaft of the vacuum feedthrough (figure 3.2C) provides control of the incident angle θ control via an external controller connected to a PC. The vacuum motor mounted on the inner part of the feedthrough is used for sample rotation - figure 3.2B.
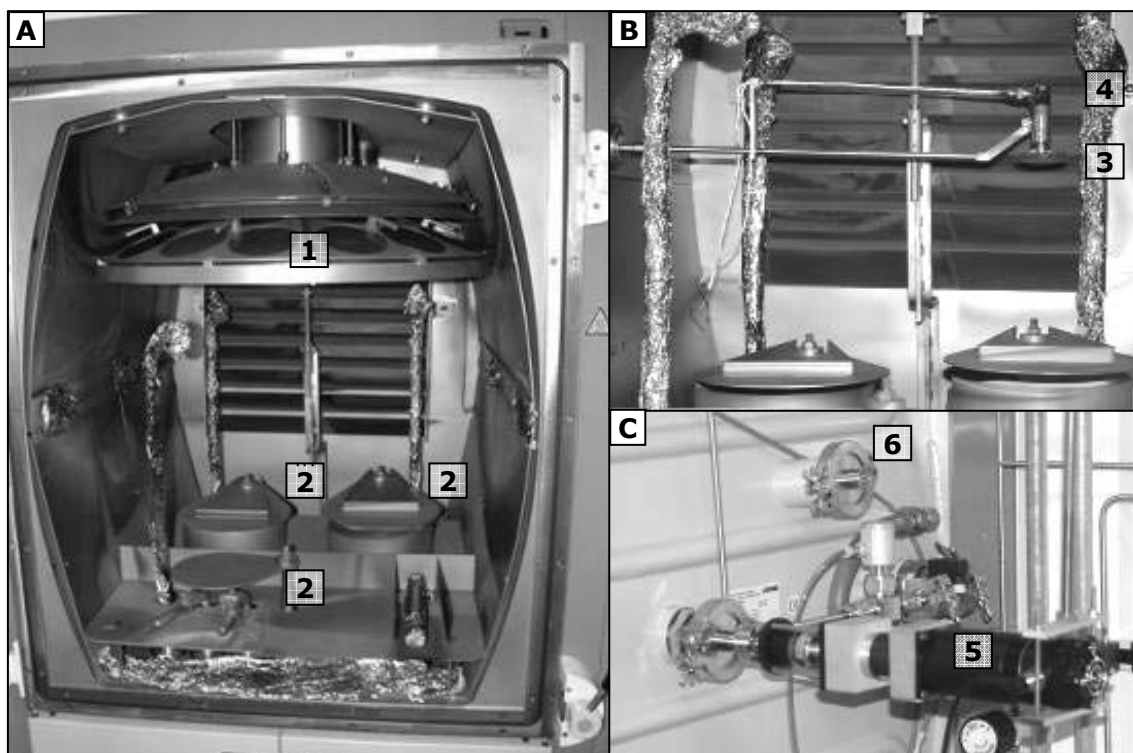
Figure 3.2. Evaporation setup for SNSL. A) Vacuum chamber of BAK 640: 1) rotation high-throughput holder, 2) evaporation sources. B) Shaft with rotation motor: 3) substrate holder 4) vacuum motor. C) BAK 640 wall chamber seen from outside: 5) stepper motor attached to rotary feedthrough, 6) electrical feedthrough for vacuum motor.

All evaporation processes could be handled by a rotation holder. However, for system convenience and performance, a stationary holder is used for fixed-angle evaporations. It is placed on the vertical shaft at the rear of the vacuum chamber, directly over one of the sources. The distance between sample and evaporation source is about 33 cm, for the rotation holder and about 50 cm for the fixed holder. During all metallization processes, the base pressure in the chamber is lower than 4.5 mTorr. The rotation motor, used in some processes, is operated at 18 rpm. Thickness of evaporated material (in BAK 640) is controlled by an automatic built-in quartz-crystal microbalance.

3.6.   Lift-off process

After the pattern is transferred to the substrate, the PS mask is removed in two steps: (i) adsorption of PS spheres to adhesive tape, then peeling it from the substrate, (ii) lift-off treatment is based on ultrasonication of the sample in THF or in 1-methyl 2-pyrrolidone (NMP). Depending on the patterning method and type of structure, ultrasonication takes 30 s to about 1 hour. The temperature of the dissolving medium is increased to about 70$°$C to improve cleaning. After THF or NMP treatment, the sample is rinsed several times with 2-propanol and dried in a stream of argon. The lift-off process is carried out in a 40 W ultrasonicator (vol. 1l).

3.7.   Characterization Methods

Characterization methods include atomic force microscopy, scanning electron microscopy, and optical microscopy characterization. The atomic force microscope (AFM) Dimension 3100 with Nanoscope IV controller from Veeco Probes is used to

characterize the dimensions of nanostructures. The samples are scanned in tapping mode using silicon tips with spring constants of $k_1 = 5$ N/m and $k_2 = 40$ N/m, having a nominal resonant frequency of 150 kHz and 300 kHz respectively. Both kinds of AFM sensors have a tip radius of less than 10 nm according to the data provided by the manufacturer (Veeco Probes). The scanning electron microscope (SEM) Supra 55 with Gemini® column, from LEO Electron Microscopy Group is used to image sample surfaces. The images are acquired at an acceleration voltage of 2-6 kV for nonconductive, and 3 – 25 kV for conductive substrates, using an in-lens detector. Surface coverage (SC) factors are estimated by calculating the fraction of bright pixels in the images selected by using the contrast threshold command, and normalizing it to the total number of pixels in the image.

4. Nanofabricated Structures

4.1. Polystyrene mask

The first observable effect to confirm formation of a hexagonal PS sphere structure is the appearance of iridescent colors. It is observed for monolayers built of particles as small as 470 nm and as large as PS 4.23 μm. For PS 127 nm, no iridescence is observed. This effect does not exist in monolayers without the hexagonal arrangement. PS latexes are received from various suppliers as water dispersions. However, on centrifugation, some of the stock solutions revealed yellowish supernatant and organoleptic tests reveal that many of the latexes possess a particular smell of styrene. Proper compositions of PS dispersions are found by adjusting the ingredients concentrations for each PS solution on a trial-error basis. Image 4.1A shows PS spheres during the recrystallization process of PS 470 nm, while image 4.1B shows a large fully recrystallized monolayer of PS 1710 nm. Three different phases of the monolayer in 4.1A are indicated by solid, white lines. The multicrystalline part, seen in figure 4.1A2 after the recrystallization step, can become monocrystalline (figure 4.1A1). However, rapid movement can destroy the order resulting in the amorphous (or multicrystalline) phase seen in 4.1A3. According to the preparation procedure, after recrystallization, the monolayer is detached from the wall, consolidated, and then anchored back to the wall. At this point, the substrates are inserted and bulk water is removed. The monolayer at this stage is shown in 4.1C.
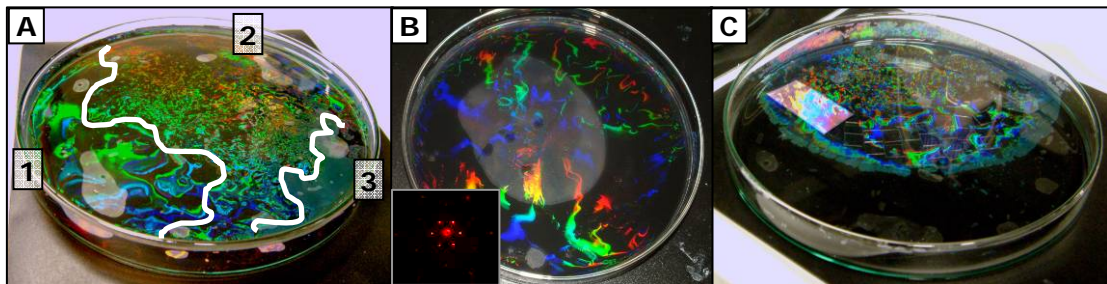
Figure 4.1. Optical images of latex monolayers on the water surface in various stages of preparation[60]. A) PS 470 nm monolayer during the recrystallization process. White lines roughly indicate borders between different phases: 1) monocrystalline phase, 2) multicrystalline phase, 3) amorphous phase. B) PS 1710 nm colloidal crystal after recrystallization. The inset shows the diffraction pattern made upon the illumination of the mask with a red laser beam. C) Condensed and anchored PS 470 nm monolayer (from image A) with substrates located beneath. All Petri dishes have diameters of 20 cm.

The search for feasible PS solution compositions yields the following dependences:

- Depletion of water from original PS solutions by centrifugation sometimes results in improved buoyancy of the spheres.

- Increasing the concentration of ethanol in PS solution leads to an enhanced deposition rate of PS spheres on the water surface. Large concentrations of ethanol (> 70%) mostly result in turbulent deposition of spheres and penetration into the subphase.

- Increasing the concentration of sulfuric acid in PS solutions leads to improved buoyancy of PS spheres - i.e. the water subphase remains cleaner if higher acid concentrations are used, but the monolayers exhibit increased

stiffness, and multicrystalline growth is induced. The two latter effects inhibit the recrystallization process or make it impossible.

- Addition of small amounts of styrene to the PS solution stabilize the interface spheres and improve the mobility within a monolayer. This in turn facilitates the elasticity of the crystal, which aids the recrystallization step.

Observation of laser diffraction from 2D colloidal crystals reveals that PS spheres shown in figures 4.1A1 and 4.1B are arranged predominantly in single crystals (i.e. rapid changes of the diffraction pattern, indicating grain boundaries, are rarely observed), contrary to the monolayer shown in figure 4.1A2. It is found that the crystal orientation in figures 4.1A1 and 4.1B changes smoothly, i.e. the diffraction pattern rotates slightly when the laser position over the monolayer changes. The degree of deformation, or "bending" of the monolayer as well as the transition of more ordered areas of the crystal into an amorphous phase, depend very much on direction, amplitude and length of the waves generated for recrystallization. As expected, after densification, the monolayer is smaller (image 4.1C) than before. It amounts to about 60% of the uncompressed crystal (image 4.1A). Such a difference in size of the loosely packed monolayer corresponds to a period change from 607 nm to 470 nm (HCP). Detailed examination (AFM and SEM) reveals that the surface of the PS particles is rough, as shown in figure 4.2A and B. The height difference of surface corrugation according to AFM measurements is 5 – 15 nm.
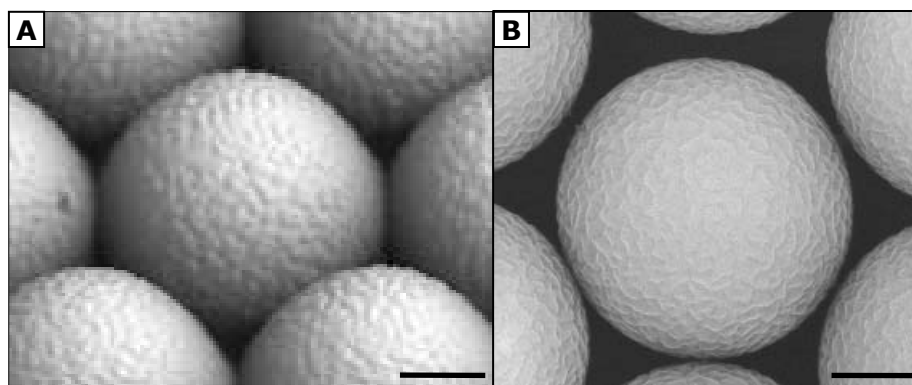
Figure 4.2. Images of the surface of PS 1710 nm spheres: A) three-dimensional (3D) AFM[60], B) SEM[61]. Scale bars are 500 nm.

As expected, the mask quality (expressed here by the number of defects) changes from sample to sample. Figure 4.3A shows SEM images of a typical mask made of PS 540 nm. One multilayer defect (A1) and cracks can be identified in the micrograph.
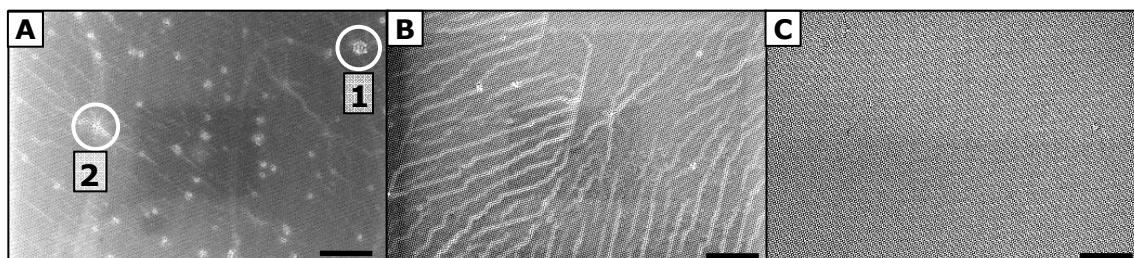
Figure 4.3. SEM images[60] of A) typical PS 540 nm crystal: 1-multilayer defect, 2-point defect, B) PS 540 nm crystal with defects, and C) high quality PS 470 nm crystal on Si substrates. Scale bars are 10 μm.

Spheres, different from the average sphere diameter, create point defects. Larger spheres, incorporated into the crystal, are sometimes found to be the reason for

crack generation (A2). Figure 4.3B shows a PS 540 nm crystal, which has pronounced structural defects and contains many aligned cracks, whereas in figure C, a well-ordered PS 470 nm mask can be observed.

To estimate the quality of colloidal crystals in a quantitative way, densities of cracks, dislocations and point defects are calculated. Densities of dislocations or cracks are calculated by dividing the length of defect lines in the image by its area. Table 4.1 displays data from SEM images of PS masks.

PS spheres: Density:	From figure 4.3A	From figure 4.3B	From figure 4.3C
Double layers [$1/cm^2$]	5.7×10^4	2.8×10^4	2.8×10^4
Point defects [$1/cm^2$]	1.6×10^6	3.7×10^5	3.7×10^5
Cracks and dislocations [m/cm^2]	7	25	1

Table 4.1. Densities of defects in various colloidal crystals calculated from SEM images shown in figure 4.3.

In another part of the examination, two colloidal crystals, one floating on water and another deposited on the substrate, are photographed. An optical microscope image 4.4A shows a colloidal crystal of PMMA 1060 nm on a Si substrate. The sample contains cracks (visible as black lines) and the average spacing of 148 spheres, measured in close packed areas, is 1102 ± 6 nm.
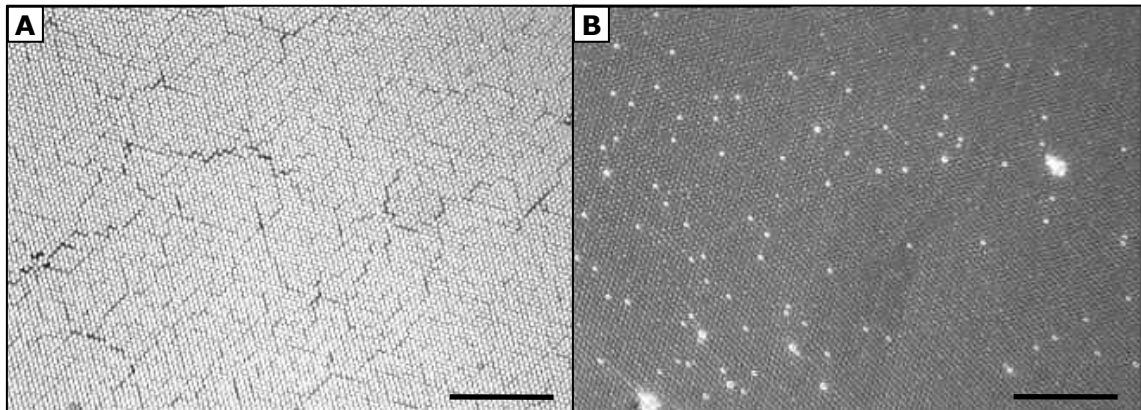

Figure 4.4 Optical microscope images[60] of colloidal crystal made of PMMA 1060 nm: A) deposited on Si substrate, B) trapped at the interface. Scale bars are 20 μm.

In figure 4.4B, a monolayer of the same kind of spheres is trapped at the interface, and the distribution of spheres appears to be more homogeneous, i.e. no cracks are observed. The average period, measured on 223 objects is 1111 ± 7 nm.

4.2.   Modified polystyrene mask

PS mask annealing by a heating plate.

SEM pictures in figure 4.5A and B, which present PS 980 nm masks annealed at 105 °C for 2 and 22 seconds have interstices sizes of h_p = 204 nm and h_p = 150 nm respectively.
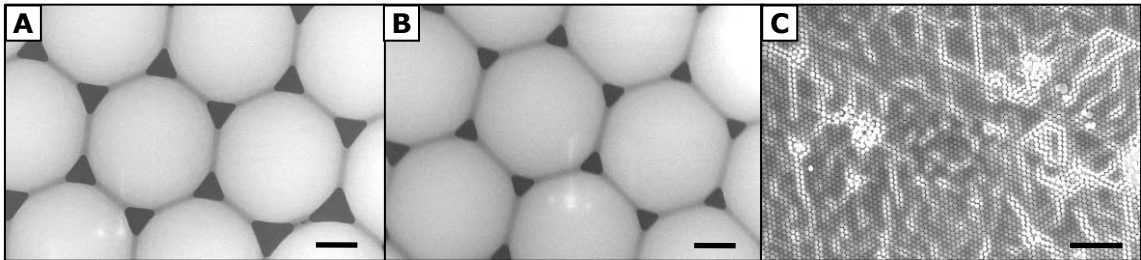
Figure 4.5. SEM images[60] of PS 980 nm masks on Si surface annealed via a heating plate at 105 °C. Annealing periods: A) 2 s, B) 22 s, C) sample B at low magnification. Structural defects are visible. Scale bars are 300 nm, 300 nm, and 10 μm respectively.

Image C shows a typical example of the mask after 22 seconds treatment. Through analysis of such images it is found that cracks present in the crystals before annealing, become larger and new errors appear. The density of cracks extracted from this image is 12 m/cm^2.
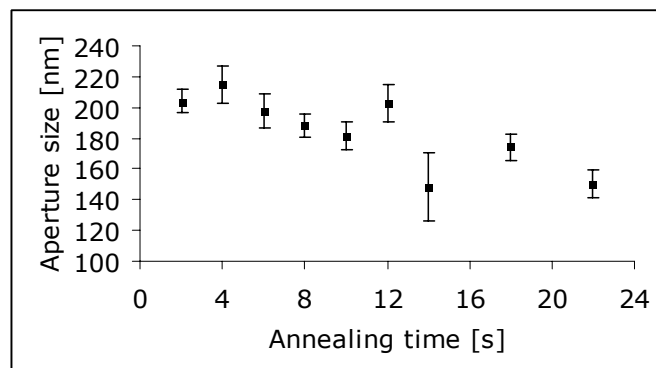

Figure 4.6. Time-dependent aperture size characteristic of PS 980 nm mask after annealing at 105 °C on a heating plate for various periods.

From these and other SEM images taken at intermediate annealing stages, the sizes of apertures are measured and plotted as a time-dependent characteristic in figure 4.6.

PS mask annealing by an air-gun.

The samples are brought to 125 °C for various periods. Interstices in masks diminish to 66 ± 3 nm (CV = 5%) after 10 s (figure 4.7A), to 38 ± 5 nm (CV = 12%) after 20 s (figure 4.7B), and after 30 s of annealing they are completely closed (figure 4.7C).
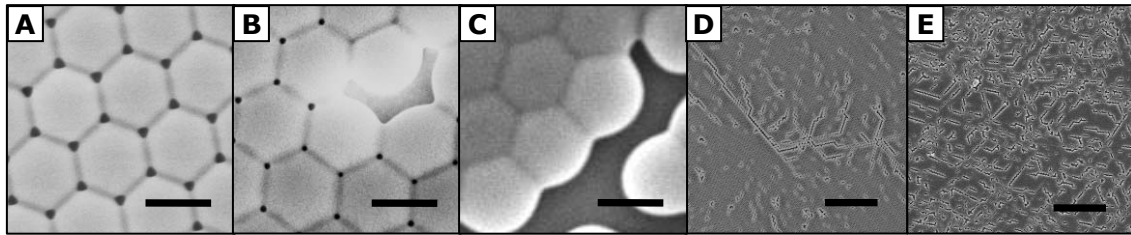
Figure 4.7. PS 540 nm masks on Al$_2$O$_3$ surface annealed at 125 °C by an air-gun[60]. Annealing periods: A) 10 s, B) 20 s, C) 30 s, D) sample A at low magnification, E) sample C at small magnification. Scale bars are 500 nm (A - C) and 10 μm (D - E).

Annealing via an air-gun causes structural errors that are evident in images 4.7D and E. Respective values of crack densities for these images are 12m/cm^2 and 25m/cm^2.

PS mask annealing by microwave irradiation.

Heating of PS 540 nm masks in a buffer mixture (water/ethanol/acetone, vol. ratio 3:1:1) is carried out in a microwave oven at 1200 W. The samples are annealed for 28 – 280 s at 1200 W. Estimated crack densities correspond to 25 m/cm^2, which is comparable to crack density of masks annealed by an air gun (12 m/cm^2 and 25 m/cm^2). After analysis of the gathered SEM images (figure 4.8A – F), it is found that the aperture size decreases linearly with ≈ 0.35 nm/s – figure 4.8G.
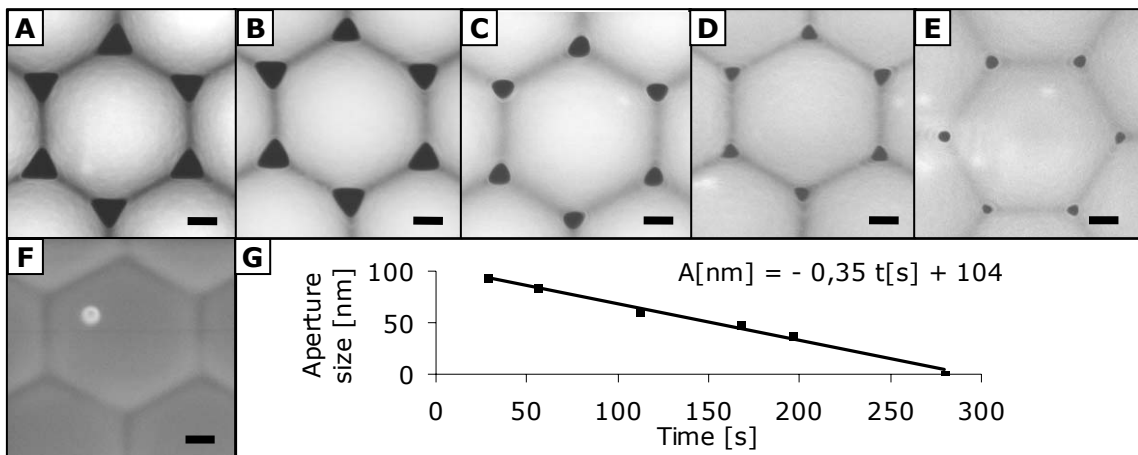

Figure 4.8. PS 540 masks annealed by microwave radiation[60] in the following time intervals: A) 28 s, B) 56 s , C) 112 s , D) 168 s, E) 196 s, and F) 280 s. Scale bars are 100 nm. G) Achieved aperture size plotted versus time.

Submerging the mask into buffer solution sometimes removes the mask from the substrate.

PS mask coating with silica

On rotating PS 470 nm mask oriented at an incident angle θ = 80°, 30 nm of silica is thermally deposited. After which, the samples are submerged into Stöber solution for 1 – 4 hours in order to grow the silica shell, which consumes space between the spheres and decreases the apertures in the mask. SEM images of PS spheres modified by a silica shell show that the silica growth is a homogeneous process (figure 4.9A-C).
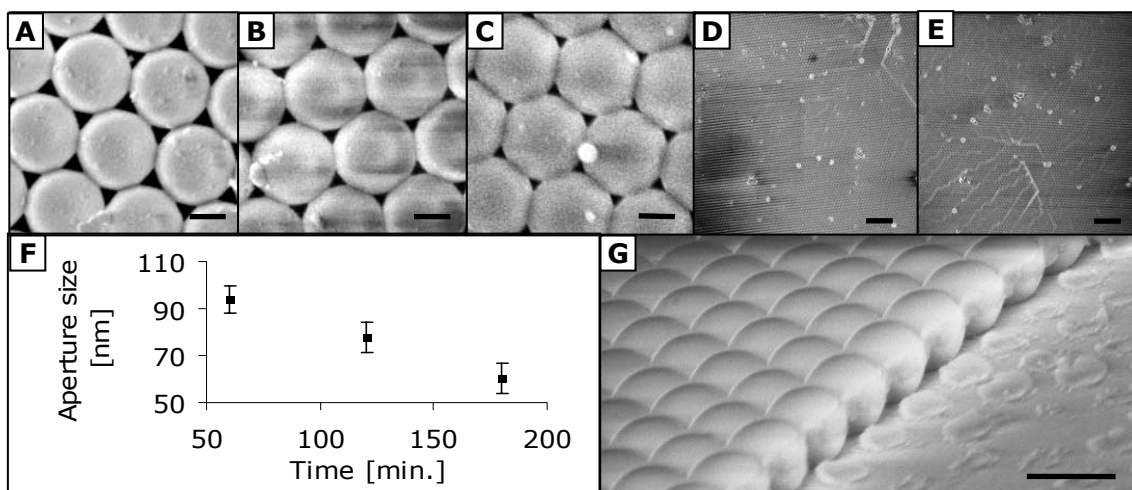
Figure 4.9. SEM images of PS 470 nm masks on Al$_2$O$_3$, covered with SiO$_2$ shells. Stöber growth is performed in the following periods and decrease apertures to the following sizes: A) time 1 h[62], size 94 ± 6 nm, B) time 2 h[62], size 78 ± 7 nm, C) time 3 h[62], size 60 ± 7 nm. Images D), E) show linear and point defects of the PS 540 nm mask after SiO$_2$ covering in 2 - 4 hours[60]. F) Aperture size versus annealing time characteristic of the PS 470 nm mask based on pictures (A, B, C). G) SEM image of silica residue on Si substrate after lift-off of the silica-modified PS 540 mask[60]. Scale bars are 200 nm (A, B, C), 5 μm (D, E) and 500 nm (G)

It is observed that small silica particles are created in some samples, which are deposited on top of colloidal crystals, figure (A – C). Crack densities calculated from images in figure D and E are 3 m/cm^2 and 6 m/cm^2 respectively. Comparing these values with the crack density present in a typical mask (7 m/cm^2, figure 4.3A) it follows, that this method (figure 4.9D-E) does not produce additional cracks. Figure F presents aperture size h_p dependence on silica growth time, based on images A – C, which appear to be linear.

Inspection of the substrate surface, after lift-off of the SiO$_2$ covered PS mask, reveals that in many samples small amounts of silica residue are attached to the sphere-substrate contact area. This indicates that the liquid can easily penetrate the mask figure (G). Submerging samples into ethanol during Stöber silica growth is found to be non-destructive for masks.

PS mask surface-dissolving

Figure 4.10 presents a PS 1710 nm mask on silicone substrate treated for various periods with vapors of THF/acetone solution (vol. ratio 1:2). SEM images show (A) the untreated sample, (B) treated for 30 s, and (C) treated for 40 s. The treatment increases the average density of cracks from about 5x10^6/cm (A) to 1x10^7/cm (B).
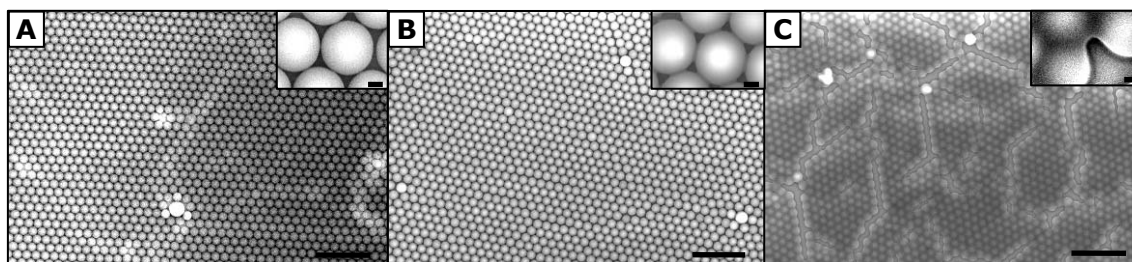
Figure 4.10. SEM images[60] of PS 1710 nm masks treated with organic vapors for the following periods: A) untreated mask, B) 30 s and C) 40 s. Scale bars are 10 μm and 500 nm (insets).

After the mask is fused completely (C), SEM examination reveals that the density of cracks in the crystal is 1×10^7/cm and that cracks are more than 5 times thicker (1100 nm) in comparison to cracks from sample (A) (159 nm) and (B) (219 nm). From insets of figure 4.10A – B it can be seen that during the first 30 s the aperture decreased from (546 ± 22) nm to (316 ± 16) nm, which gives a decreasing rate of 7.7 nm/s. From images B – C it follows that in the last 10 s the apertures decrease from (316 ± 16) nm to a completely closed structure, which gives a rate of at least 31 nm/s. Due to rapid reaction of the mask to the presence of THF/acetone vapors, this solution composition is inconvenient.

Due to the aforementioned disadvantage of the THF/acetone solution, in another experiment, a less aggressive solution is used (THF/ethanol, vol. ratio 1:4). The PS 540 nm masks are treated with vapors for 10 – 50 s (figure 4.11A - E). The sample exposed for 60 s, has all interstices fused and has many defects (figure 4.12B).
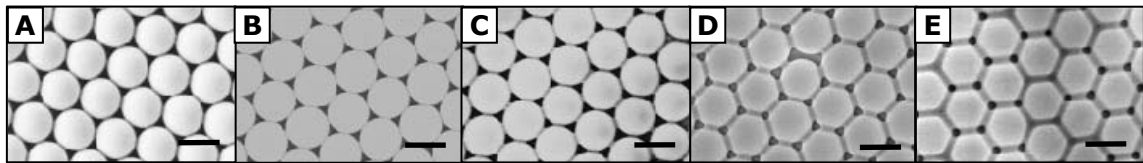
Figure 4.11. SEM images[60] of PS 540 nm masks exposed to THF/ethanol vapors for increasing time, A) 10 s, B) 20 s, C) 30 s, D) 40 s and E) 50 s, show decreasing aperture sizes (see figure 4.12A). Scale bars are 500 nm.

It is concluded that for longer exposition periods, apertures decrease inhomogeneously – for example, about 30% of the apertures in image 4.11E are closed, while the rest of the gaps still have considerably large sizes. The interdiffusion rate is constant, except for the last 10 s (figure 4.12A), where sudden mask collapse is observed, similarly to the previous experiment with PS 1710 nm spheres.
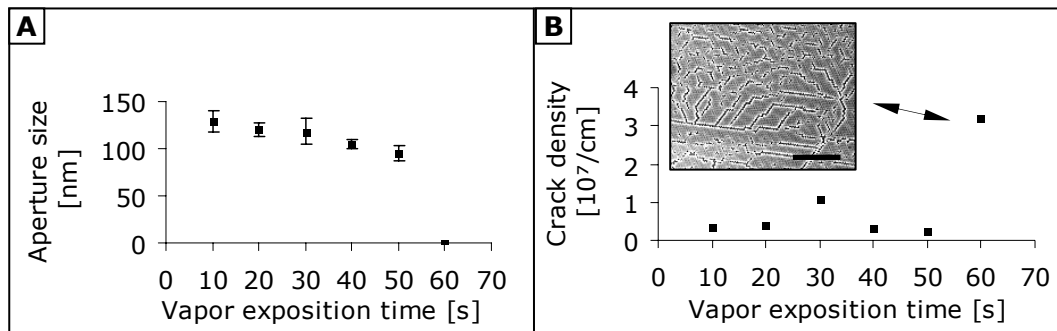
Figure 4.12. Time-dependent characteristics of PS 540 nm masks exposed to THF/ethanol vapors: A) Aperture size and B) crack density. The inset in image (B) shows a collapsed PS crystal[60]. The scale bar is 10 μm.

The density of the cracks does not show monotonic behavior as well as B. Within the last 5 s of treatment, the colloidal crystal has collapsed, forming a closed layer perforated with cracks (inset in image B).

4.3.   Etched polystyrene mask

Optimal conditions for etching of PS spheres are found experimentally. A PS 980 nm mask is used for that purpose. A test etching is performed in carbon CF_4/O_2 plasma (flow rate 40/60 of standard cubic cm (sccm), pressure $Pr = 80$ mTorr, power $Po = 80$ W). Spheres are deposited on a silicon substrate and subsequently etched for 2 min. From the SEM image in figure 4.13A it is observed

that spheres are almost completely consumed and that the substrate is slightly etched.
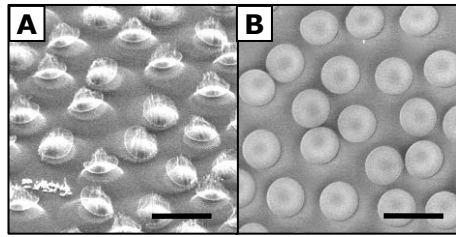
Figure 4.13. SEM images[60] of a PS 980 nm mask on a Si substrate. The mask is etched in CF$_4$/O$_2$ (flow rates: 40/60 sccm) plasma driven at A) 80 W - side view, B) 40 W – top view. Scale bars are 1 μm.

Such an etching process is too fast to be useful for precise microsphere etching.

Preparation method:

To slow down the process, the same experiment is performed at reduced power (40 W); figure 4.13B. The mask survives the treatment, but the hexagonal order is disrupted. To avoid this problem, in the next trial, the mask is fused with the substrate by short an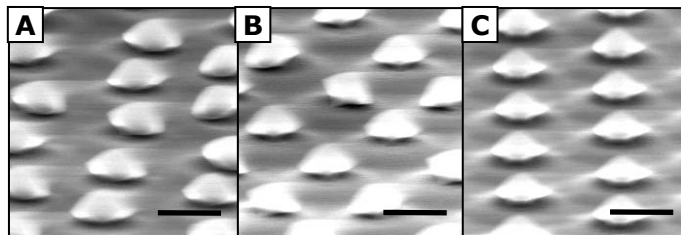nealing at 105 °C. Figure 4.14 presents SEM images of PS 980 nm samples on Si, annealed for 2, 4 and 6 s on a heating plate, and subsequently etched in CF$_4$/O$_2$ plasma (15/30 sccm) driven at 60 W and 60 mTorr for 2 min. The PS crystals in images A and B are disordered, while the sample in C is not. This indicates that the 6 s annealing fused the spheres to the substrate strongly enough to keep the hexagonal order during plasma treatment. However, there is still slight substrate damage noticeable. Therefore, further optimization of the process is required.

Figure 4.14. SEM images[60] of PS 980 masks etched by CF$_4$/O$_2$ (flow rates: 15/30 sccm) plasma (60 W, 60 mTorr), after annealing at 105 °C for the following periods: A) 2 s, B) 4 s, C) 6 s. Scale bars are 500 nm.

Etching of the PS 980 sample with pure oxygen (flow rate 60 sccm) at 60 W and 60 mTorr for 2 min, inhibits chemical etching of the substrate, but at the same time it increases the number of oxygen ions that could react with PS. As a consequence, exclusion of CF$_4$ increases the yield of PS etching by oxygen and faster mask consumption – figure 4.15A. The PS etching rate is reduced in the same process by decreasing the oxygen flow to 25 sccm and by the addition of a neutral gas like argon, at 20 sccm, as shown in figure 4.15B. It is found that plasma with low oxygen content (5 sccm), and increased Ar (40 sccm) result in inefficient chemical etching and that redeposition of sputtered material (polymer) takes place. This is shown in figure 4.15C, where the PS 470 nm mask is etched for 50 s.
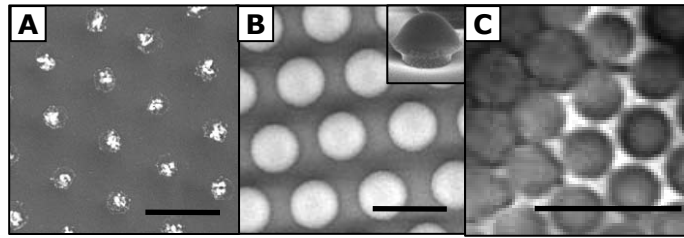
Figure 4.15. SEM images[60] of masks annealed at 105 °C for 6 s and processed by RIE plasma at 60 mTorr and 60 W. A) PS 980 nm mask etched in O$_2$ (60 sccm) plasma for 2 min. B) PS 980 nm mask etched in Ar/O$_2$ plasma (20/25 sccm) for 2 min, C) PS 470 nm masks etched in Ar/O$_2$ plasma (40/5 sccm) for 50 s. Scale bars are 1 μm.

Once the plasma conditions have been adjusted, a PS 540 nm mask is deposited on Si substrate, annealed for 5 s at 105 °C and used to find the etching rate of the RIE process. Six samples are etched in periods of 30 – 60 s using Ar/O$_2$ (10/35 sccm) plasma, driven at 60 W and 60 mTorr. The samples are characterized by SEM (figure 4.16A-G) and measured diameters are plotted as a function of time in figure 4.17.
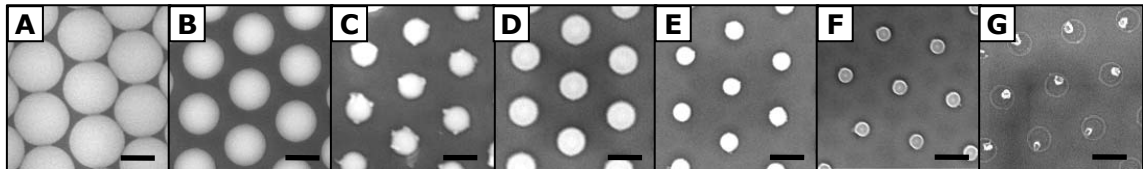
Figure 4.16. SEM images[60] of PS 540 nm masks annealed and exposed to RIE. Measured diameters and etching periods are: A) 535 nm/unetched, B) 401 nm/30 s, C) 252 nm/35 s, D) 294 nm/40 s, E) 175 nm/45 s, F) 129 nm/50 s, G) 80 nm/60 s. Scale bars are 300 nm.
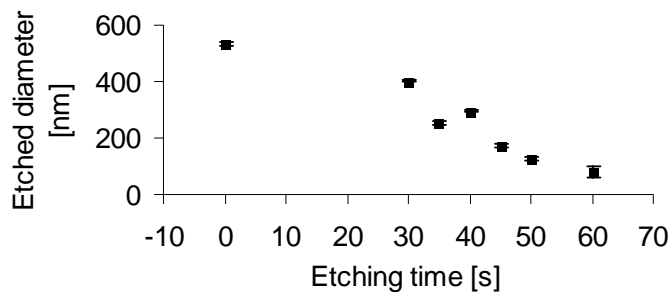
Figure 4.17. PS 540 nm spheres etched in Ar/O$_2$ plasma (flow rates: 10/35 sccm) operated at 60 W and 60 mTorr. Data plotted on the basis of measurements acquired from SEM images presented in figure 4.16.

The sample in figure 4.16G is almost completely etched. Inhomogeneous PS remains, inside a bigger ring-like residue in the micrograph, indicating contact areas of spheres and the substrate. Spheres from figure 4.16C have small features on the edges. These elements are pointing in directions where neighboring spheres lie. Such behavior is also encountered in other samples, which are not annealed.

RIE of a PS 540 nm mask is homogeneous and shows linear behavior, except the non-etched sample – figure 4.17.

4.4. Triangles and dots

Three different sizes of triangular particles are prepared by evaporation of 30 nm of Co at an incident angle $\theta = 0°$, through PS 496 nm, PS 980 nm, and PS 1710 nm masks. After removal of the mask with adhesive tape and subsequent (2 min) ultrasonication in THF, SEM characterization yields the images shown in figure 4.18. The influence of the PS sphere roughness (shown in figure 4.2) on the evaporated triangle can be observed in the insets of figure 4.18B and C, in the form of edge corrugation.
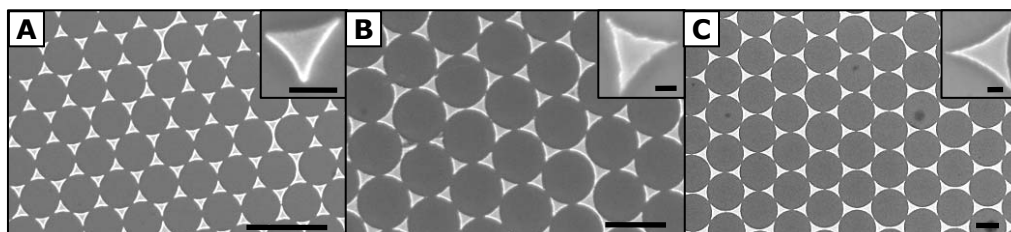
Figure 4.18. SEM images[63] of triangle arrays evaporated (30 nm Co) through: A) PS 496 nm, B) PS 980 nm, and C) PS 1710 nm masks. Scale bars in each set of pictures are 1 μm and 100 nm (insets).

Diameter D_0, triangle size h_p, intersphere contact area diameter d, spacing S_p and surface coverage SC (as defined in paragraph 2.6.3) are measured using SEM images from figure 4.18.

PS [nm]	D_0 (M) [nm]	$h_{p,\,d=0}$ (C) [nm]	h_p (M) [nm]	d (C) [nm]	S_p (M) [nm]	S_p (C) [nm]	SC (M) [%]	SC (C) [%]
496	518 ± 3	189	141 ± 6	97 ± 6	305 ± 5	299	10.7 ± 1.5	9.31
980	943 ± 10	345	232 ± 15	226 ± 15	560 ± 26	544	10.3 ± 2.4	9.31
1710	1683 ± 20	616	501 ± 21	230 ± 21	987 ± 19	971	9.9 ± 1.0	9.31

Table 4.2. SEM measurements (M) and calculated (C) values of PS diameter D_0, triangle height h_p, intersphere contact area diameter d, spacing S_p and surface coverage SC for three sizes of PS latex: PS 496 nm, PS 980 nm, and PS 1710 nm.

From these values, listed in table 4.2, the following observations can be made:

- Values of PS diameters (D_0 (M)), extracted from SEM images, are slightly different from the nominal PS latex diameters. Percentage variations for PS 1710 nm, PS 980 nm, and PS 496 nm, are + 1.5%, + 3.8% and - 4.4% respectively. (Coefficient of variation (*CV*) given by the manufacturers are CV = 1.2% for PS 1710 nm and *CV* = 4% for PS 980 nm).

- Triangle height values measured and normalized to the diameter of PS spheres (h_p (M)/D_0) for PS 1710, PS 980 and PS 496 nm, are 30%, 25% and 27%, whereas the normalized theoretical triangle height value is PS size independent: (h_p (C)/D_0) = 37%.

- Diameters of contact areas between spheres (d (C)) derived as fractions of PS diameters are 14% for PS 1710 nm, 24% for PS 980 nm and 19 % for PS 496 nm.

- Calculated and measured spacing values of neighboring triangles (S_p (C)) and S_p (M) are equal within the error range for all PS sizes.

- Calculated and measured values of surface coverage (*SC* (C)) and (*SC* (M)) are identical within the error range for all PS sizes.

Apertures in a mask, evaporated with a sufficiently thick layer of metal, should be closed due to the metal deposition at the edges of the interstices as shown earlier (figure 2.7). A simple test is realized by evaporation of increasing amounts of Ni (P_0 = 20 – 200 nm) through a PS 540 nm mask on Si substrate, and after mask removal by 1 min ultrasonication in THF, height profiles of Ni nanoparticles are acquired using AFM (figure 4.19).
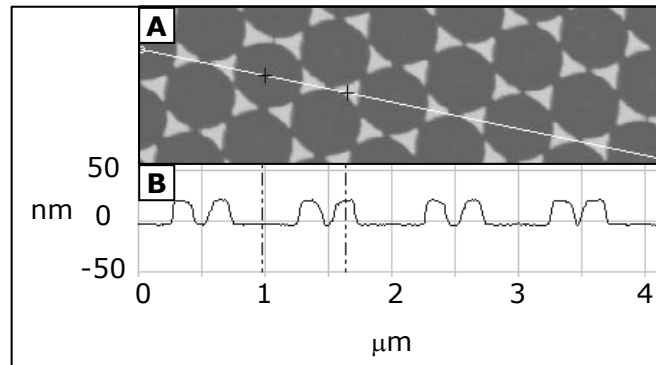
Figure 4.19. A) AFM topography image[60] and B) cross-section section profile[60] of along line depicted in (A) of a 20 nm Ni layer evaporated through a PS 540 nm mask.

Height measurements of Ni nanoparticles prepared in the experiment are summarized in table 4.3. The maximum thickness of Ni nanoparticles achieved in this experiment is P $\approx$ 123 nm, indicating that at this evaporation layer thickness the mask becomes closed and no more material will reach the substrate.

Thickness evaporated [nm]	Height measured [nm]
20	20
50	48
100	99
150	123
200	122

Table 4.3. Measured Ni nanoparticle heights obtained from 5 samples.

Similar AFM tests performed by evaporation of 400 nm Au through PS 980 nm, and 1000 nm Al through PS 1710 nm, reveal that maximum heights of nanoparticles for these masks is $P_{PS\ 980} \approx 381$ nm and $P_{PS\ 1710} \approx 542$ nm. SEM images of these nanoparticles show their morphology (figure 4.20A-B). In image A some pyramids have been removed during the lift-off process (adhesive tape peeling and THF 1 min ultrasonication).
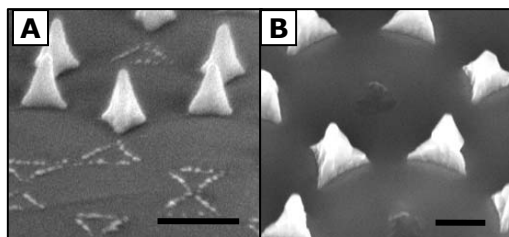
Figure 4.20. Images[60] of tetrahedronal particle arrays evaporated through a PS 980 nm mask. A) SEM, PS 980 nm. B) SEM, PS 1710 nm. Scale bars are 500 nm.

In image 4.20B, there are spots in the areas of contact between spheres and the substrate – polymer residue, which are the remains of incompletely removed PS spheres.

Figure 4.21 shows Co arrays of nanoparticles evaporated through a PS 540 nm mask annealed for 196 s by microwave radiation according to the previously described procedure. Co nanoparticles presented here have an average diameter of about 40 nm, but due to heterogeneous aperture sizes, particles as small as 25 nm and as large as 60 nm are often found in some samples.

Figure 4.21. SEM image[60] of Co dot arrays evaporated through an annealed PS 540 nm mask. Scale bars are 100 nm (inset) and 1 μm.

4.5. Rods

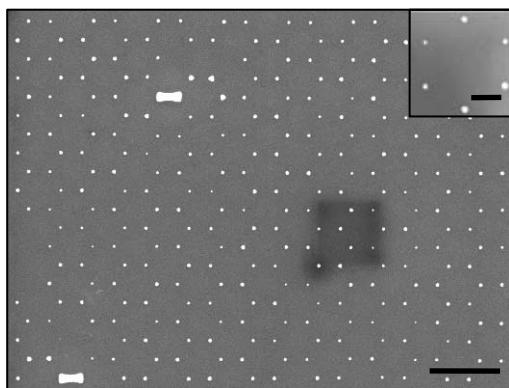Preparation of nanorod arrays is performed by evaporation of 100 nm of Au through the PS 540 nm mask on Si that is tilted during evaporation. The incident angle θ is alternated between + 30° and – 30°. The PS mask is previously annealed using the earlier described microwave heating (1200 W, 112 s in buffer solution) to reduce the apertures to about 60 nm – figure 4.22A. After successful preparation and mask lift-off (adhesive tape, THF ultrasonication for 30 s), arrays of nanorods are analyzed by SEM – figures (B, D) and by AFM – figure C. In figure B there are "strings" of very small "particles" visible, surrounding each gold rod. Figure 4.23 shows three-dimensional (3D) AFM images of nanorods. The cross section profile reveals the surface morphology of nanoparticles. Figure 4.23A shows length measurements of nanorods, and figure 4.23B of nanorods together with the surrounding nanoparticle string.
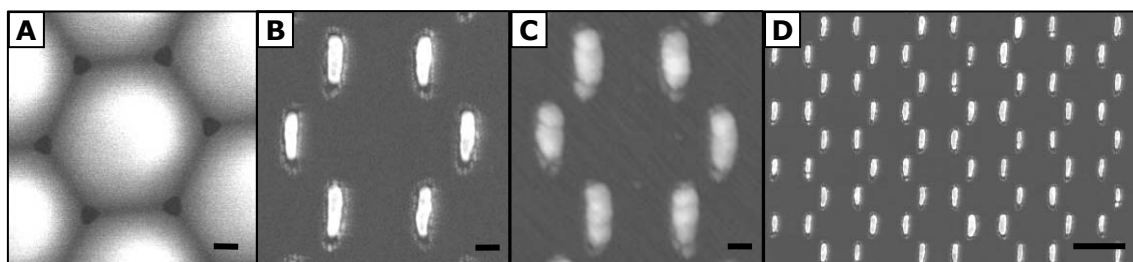
Figure 4.22. A) A PS 540 nm mask with about 63 nm apertures created by microwave annealing[60]. B) and C) – SEM and AFM (respectively) images[60] of nanorods created by evaporation of 100 nm of Au through an annealed PS 540 nm mask. Incident angle of evaporation is changing periodically from θ = - 30° to θ = 30°. D)[60] Honeycomb array of Au nanorods. Scale bars are 100 nm (A-C) and 500 nm (D).
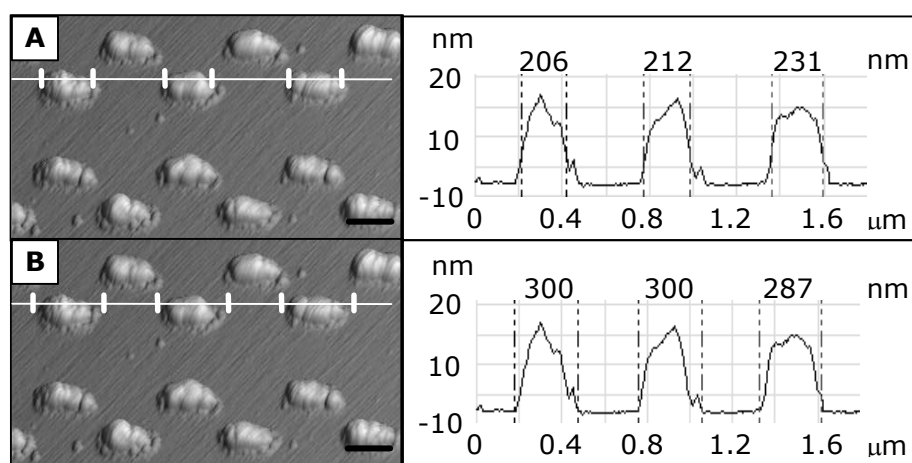
Figure 4.23. AFM 3D image[60] of gold nanorods and corresponding cross-section measurements. A) Length of nanorods. B) Length of nanorods with nanoparticle strings. Scale bars are 200 nm.

Values of thickness, width, and length, extracted from acquired micrographs are listed in table 4.4. Gold rods measured by SEM are (174 ± 7) nm long and (55 ± 5) nm wide, whereas particles from the same sample, measured by AFM are (194 ± 11) nm long and (73 ± 7) nm wide.

[nm]	Mask		Rods			Rods with "particle strings"	
	Aperture diameter A_0 [nm]	Contact area diameter d [nm]	Length L_0 [nm]	Width W [nm]	Thickness P [nm]	Length L_0 [nm]	Width W [nm]
AFM	–	–	194 ± 11	73 ± 7	25.3 ± 7.0	279 ± 8	95 ± 11
SEM	63 ± 4.8	242 ± 7	174 ± 7	55 ± 5	–	256 ± 4	103 ± 5

**Table 4.4. AFM and SEM measurements of the gold nanorods evaporated through a PS 540 nm mask.**

The difference between AFM and SEM nanorod sizes is due to an imprecise measurement, since the presence of the "nanoparticle string" around each nanorod prevents unambiguous determination of the beginning and the ending of a rod. "Strings" are located very close to the nanorods, and the AFM tip is not capable of

probing the structure (observable in cross-section profiles in figure 4.23) at given scanning conditions. Therefore, a nanorod size measured by the AFM is bigger than from the SEM image. AFM measurements of a rod with a surrounding "string of nanoparticles" ($L_0 = (279 \pm 8)$ nm and $W = (95 \pm 11)$ nm) coincide better with SEM measurements ($L_0 = (256 \pm 4)$ nm and $W = (103 \pm 5)$ nm respectively), in comparison to the measurement of rods without "particle strings". This is a consequence of the fact that beginning and ending of "nanoparticle strings" are easier to distinguish. The width of nanorods measured by SEM ($W = (55 \pm 4.6)$ nm), as expected are the same size as the measured sizes of gaps in the mask ($A_0 = (63 \pm 4.8)$ nm).

The values of lengths and widths of nanorods acquired by AFM have been decreased by 20 nm (probe radius $\approx$ 10 nm) to deconvolute the tip broadening effect.

4.6.   Cups and rings

For preparation of rings, PS 470 nm masks are deposited on sapphire substrates and modified by rotation evaporation of 30 nm of silica at an incident angle of $\theta = 80°$ followed 180 min by incubation in TES solution (Stöber silica coating). The apertures in the mask decrease to about 60 nm (figure 4.9C). Three different incident angles, $\theta = 6°$, $10°$, and $14°$, are used for evaporation of gold rings. Samples evaporated with 5 nm of Ti to promote adhesion between Si and Au, and with 100 nm of Au, are cleaned in a lift-off process by adhesive tape and subsequent double ultrasonication in THF for 60 s. AFM images are shown in figure 4.24 and the obtained measurements are summarized in table 4.5.
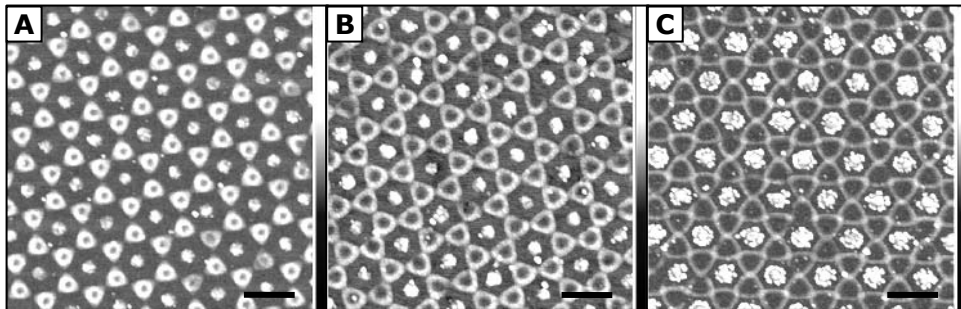
Figure 4.24. AFM images of Ti/Au rings[62] evaporated through silica-coated PS 470 nm spheres, at the following incident angles: A) $\theta = 6°$, B) $\theta = 10°$, C) $\theta = 14°$. Scale bars are 500 nm. Height grayscale corresponds to 40 nm.

The particles visible in the AFM images have a triangular shape. In areas where PS spheres are touching the substrate, there is residue debris visible.

Incident angle θ [°]	Inner diameter [nm]	Outer diameter [nm]	Thickness measured [nm]
6	47 ± 5	185 ± 13	10.9 ± 1.6
10	118 ± 10	248 ± 11	8.2 ± 1.3
14	172 ± 12	269 ± 11	4.9 ± 1.2

Table 4.5. AFM measurements of rings evaporated through a PS 540 nm mask with apertures decreasing to about 60 nm by covering with silica.

Examples of structures prepared by a two-step evaporation procedure are shown in figure 4.25. A layer of Cr, 150 nm thick is evaporated at an incident angle $\theta = 25°$ with sample rotation and followed by 15 nm of Ni deposition at $\theta = 0°$. The mask lift-off process is carried out using adhesive tape and 30 s of ultrasonication in THF.

Figure 4.25A shows Ni dots inside Cr cups. Some Ni nanoparticles are accidentally removed during ultrasonication. The Ni dots are smaller than the nominal size of the apertures in PS 540 nm mask. This is due to the deposition of Cr at the edges of the apertures. A second micrograph (figure 4.25B) shows 30 nm thick Au triangles evaporated ($\theta = 0°$) through PS 1710 nm on a silicon substrate, and covered by Cr cups deposited by rotation at the incident angle $\theta = 25°$. The mask lift-off process is the same as described previously.
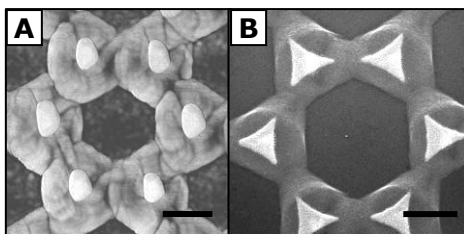
Figure 4.25. A) AFM phase image[60] of Cr cups with Ni dots inside, evaporated through a PS 540 nm mask. B) SEM image[60] of Au triangles covered by Cr cups, evaporated through a PS 1710 nm mask. Scale bars are 200 nm and 500 nm respectively.

4.7. Grids

Spherical grids are prepared by evaporation of a Ti/Au (2/20 nm) layer through an etched PS 470 nm mask on sapphire. Etching conditions are the same as those used for etching in figure 4.16, and the treatment lasts 40 – 60 s. After removal of the PS mask using adhesive tape and 10 min THF ultrasonication, the samples are studied by an AFM (figure 4.26). Centers of the meshes in the grid are filled by polymer residue after incomplete mask lift-off. In the case of intensively etched spheres, mask lift-off is not possible (figure 4.26E). In that case evaporated metal created a continuous layer on top of the mask.
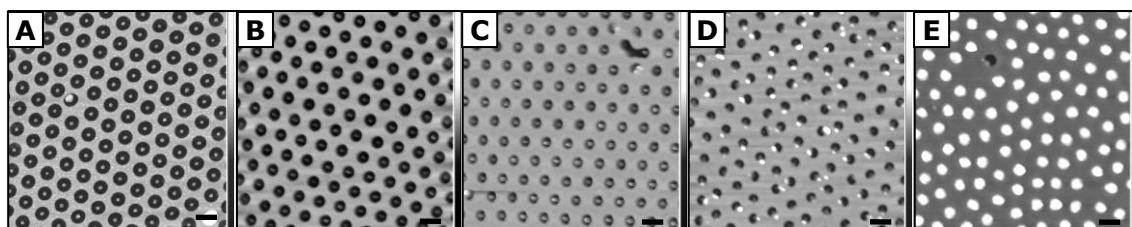
Figure 4.26. AFM images of Ti/Au grids[64] with spherical meshes evaporated through PS 470 masks etched fpr the following periods: A) 40 s, B) 45 s, C) 50 s, D) 55 s, E) 60 s. Scale bars are 500 nm. The height grayscale corresponds to 100 nm.

Therefore, encapsulated spheres could not be removed by an organic solvent. The hexagonal order of the sample etched in 60 s is slightly disturbed. The holes in the Au layers are studied, and the results are summarized in table 4.6. The grid period value, which is equivalent to the PS diameter D_0, measured by the AFM (separately for each sample) agrees with the nominal PS diameter within the range of the measurement error.

Etching time [s]	40	45	50	55
Grid period (D_0) [nm]	449 ± 14	463 ± 14	471 ± 12	441 ± 37
Hole diameter (D) [nm]	298 ± 10	263 ± 15	247 ± 21	161 ± 23
Calculated surface coverage [%]	60 ± 5.2	71 ± 5.1	75 ± 5.5	88 ± 5.5
Measured surface coverage [%]	56 ± 2.5	71 ± 3	77 ± 2	82 ± 4.5

Table 4.6. AFM measurements of Ti/Au (2 nm/20 nm) grids deposited on sapphire. Values of grid period and hole diameter are used in equation 2.9 for calculation of the surface coverage. Obtained *SC* values are compared with *SC* values measured by "ImageJ".

Surface coverage factors are calculated from the measured grid period D_0 and the hole diameter D via equation2.9. Results are then compared with values obtained by image analysis. The results are in good agreement within the error range. Incomplete mask removal, shown previously (figure 4.26), has stimulated the following lift-off test performed with increased ultrasonication time at elevated temperature using NMP solvent.
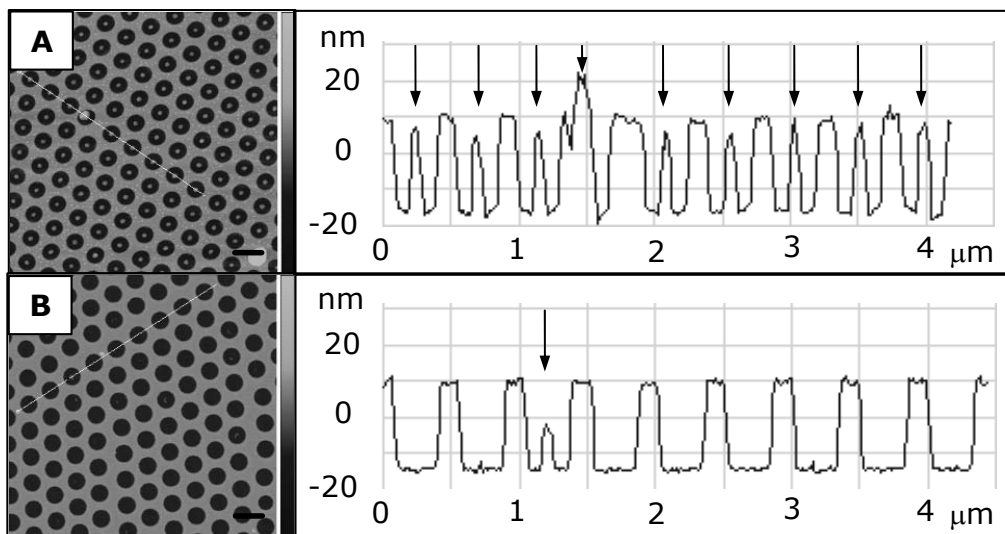
Figure 4.27. Comparison of AFM micrographs[64] of samples cleaned by two different methods. Arrows indicate PS residue. A) ultrasonication at RT for 2 min in THF – PS residue still present, B) ultrasonication at about 40 °C for 30 min in NMP – residue removed. Scale bars are 500 nm. Height grayscale corresponds to 100 nm.

Figure 4.27 shows a comparison of the cross section of the grid shown previously in figure 4.26A, which is cleaned in THF ultrasonication bath for 2 min and for another sample prepared in the same way, but cleaned in NMP ultrasonication bath for 30 min at about 40 °C. In the case of NMP treatment, the PS residue is almost completely removed as presented in figure 4.27B.

In another experiment, samples with gold grids are tested against aging. It is found that samples directly after preparation (figure 4.28A) look different from aged samples 4.28. All grids are stored at room temperature in a PS box for 160 days

and used from time to time for acquisition of optical spectra or examination by scanning near-field optical microscopy.
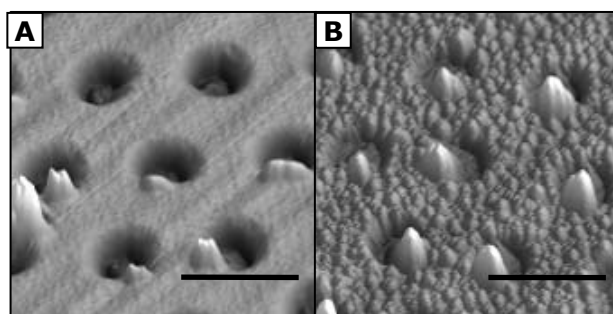
Figure 4.28 Gold grids evaporated through etched PS 470 nm spheres[64]. A) mesh size 161 nm – fresh sample and B) after 160 days. Scale bars are 500 nm.

On the surface of aged sample, figure 4.28B, formation of "particles" has occurred. All samples checked for aging (figure 4.26A-D) have similar morphology, but the size of particles is bigger in samples used more often. Observed "particles" are several times smaller than the holes. Subsequent cleaning in NMP ultrasonic bath for several minutes does not remove "particles" from the surface.

Grids fabricated by the angle-dependent EBE process can have various morphologies. Figure 4.29 shows an example of a grid created by evaporation of $P_0 = 100$ nm of gold through a PS 980 nm mask at the incident angle $\theta = 70°$. Before evaporation the mask is fixed by 6 s fusion at 105 °C and subsequently etched in 120 s in Ar/O$_2$ (35/10 sccm) plasma driven at 60 mTorr and 60 W. For the lift-off procedure, adhesive tape is used and subsequent NMP ultrasonication for 2 min is applied.
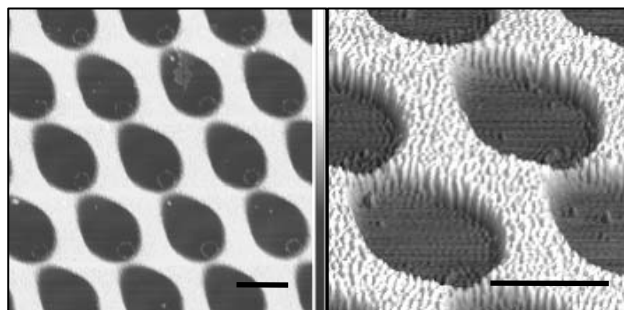
Figure 4.29. AFM height and 3D image of an Au grid evaporated through an etched PS 980 nm mask at the incident angle $\theta = 70°$. Scale bars are 500 nm. Height grayscale in the left image corresponds to 100 nm.

The EBE direction is aligned with the $<\bar{1}2\bar{1}0>$ direction of the colloidal crystal. Preparation of grids with oval meshes is similar to the preparation of lines; therefore equation 2.13, describing the thickness of the grid in relation to the evaporated thickness is also valid for grids: $P = P_0\cos(\theta) = 100\cos(70°) = = 34.2$ nm. The thickness of the grid measured by AFM is (34 ± 2) nm, which agrees well with the calculated value.

4.8. Lines

Layers of Co/Al (30/3 nm) are evaporated at the incident angle $\theta = 62°$ through PS 540 nm on Si, previously etched for 45 s in Ar/O$_2$ (10/35 sccm) plasma driven at 60 mTor and 60 W. The evaporation direction is aligned with the $<\bar{1}2\bar{1}0>$ direction of the colloidal crystal using red laser diffraction. As a result, a periodic pattern of

nanolines is obtained. During lift-off, adhesive tape and subsequent NMP ultrasonication for 2 min is used. The lines are imaged (figure 4.30A) and characterized (table 4.7) by AFM. A SEM image in figure 4.30B shows nanolines manufactured using a PS 470 nm etched mask with only part of the mask removed.
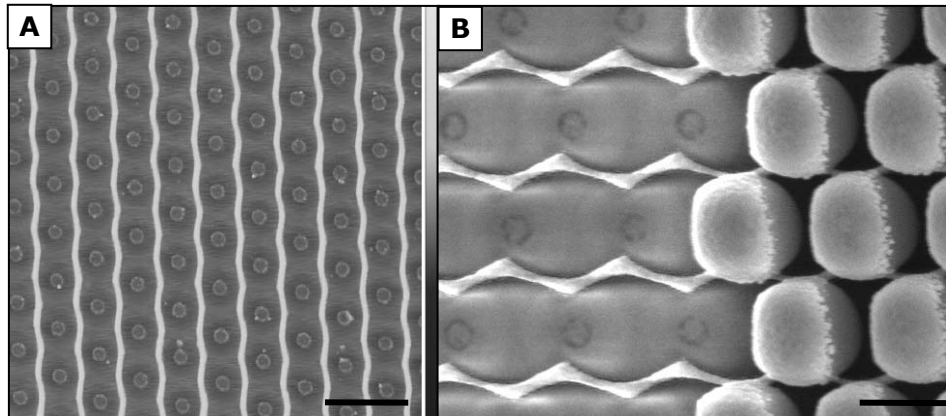
Figure 4.30. A) AFM Image[60] of Co/Al (30/3 nm) wires evaporated through a PS 540 nm mask etched in Ar/O$_2$ (10/35 sccm) plasma driven at 60 mTor and 60 W for 45 s. Scale bar is 1 μm. B) SEM image[60] of a PS 470 etched mask after metal evaporation of lines. The scale bar is 300 nm.

The measured value of the mask periodicity $D_0 = (554 \pm 6)$ nm is 14 nm larger than the nominal diameter of the PS 540 nm spheres used. The difference is caused by the drift of the sample during acquisition of the image. D_0 and the etched sphere diameter value D are used for calculation of the line thickness (equation 2.13), line width (equation 2.11), spacing (equation 2.14) and surface coverage of the lines (equation 2.12). Experimental values of the line thickness $P = (14 \pm 1)$ nm, and line spacing $S_p = (482 \pm 22)$ nm correspond well to calculated values $P = (15 \pm 2)$ nm and $S_p = (480 \pm 5)$ nm, respectively.

	Sphere diameter D_0 [nm]	Etched sphere diameter D [nm]	Line thickness P [nm]	Line width W [nm]	Line spacing S_p [nm]	Surface coverage SC [%]
Calculated	-	-	15 ± 2	61 ± 13	480 ± 5	12.8 ± 2.5
Measured	554 ± 6	419 ± 7	14 ± 1	67 ± 9	482 ± 22	14.8 ± 1.3

Table 4.7. Calculated and measured dimensions of Co/Al lines deposited on Si through PS 540 nm mask.

The calculated line width $W = (61 \pm 13)$ nm is close to the measured width of nanolines of $W = (67 \pm 9)$ nm. Consequently, measured surface coverage $SC = (14.8 \pm 1.3)$% agrees well with the calculated value of $SC = (12.8 \pm 2.5)$%. To check the alignment of the crystal with the evaporation direction over a large length scale, the sample (1x1 cm) is examined using SEM (figure 4.31A). Nine images are acquired at different sample locations sketched in figure 4.31B.
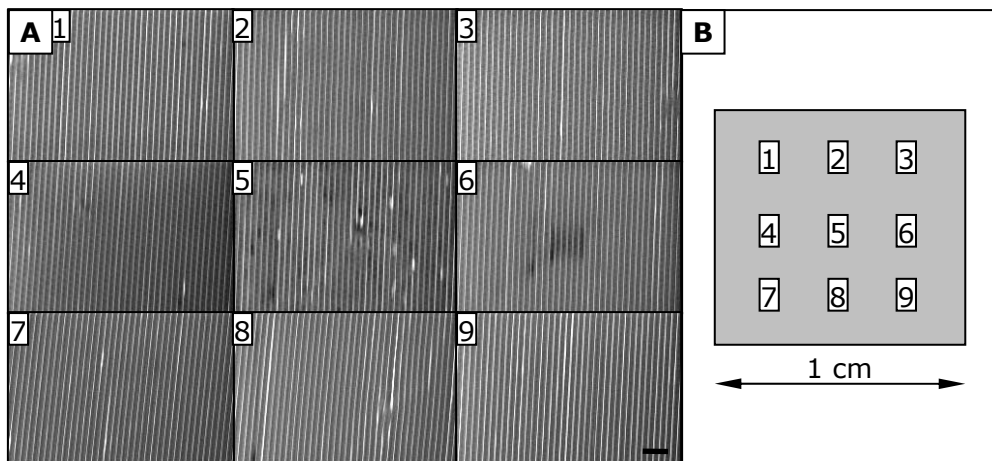
Figure 4.31. A) SEM images[60] of Co/Al wires collected at nine different sections of the 1x1 cm^2 sample. The scale bar is 2 μm. B) Locations of acquisition sections.

The acquired images show straight Co/Al lines oriented vertically with randomly distributed errors: gaps (e.g. in 4.31A5) and thickened lines (e.g. in 4.31A8).

4.9. Pillars

This section presents several examples of fabrication of pillars using metallic or PS colloidal masks and reactive ion etching. In the first experiment, arrays of Cr triangles (20 nm thick) evaporated through PS 1710 nm spheres on silicon are used as a mask for the RIE process, using SF_6/O_2 (26/5 sccm) plasma operated at 60 W in 60 mTorr. After 45 s treatment, silicon "pillars" are created. Figure 4.32A shows the Si pillars with the Cr mask on top, and figure B shows the same triangles after lift-off by 30 s THF ultrasonication. Removal of Cr triangles from Si "pillars" is purely mechanical.
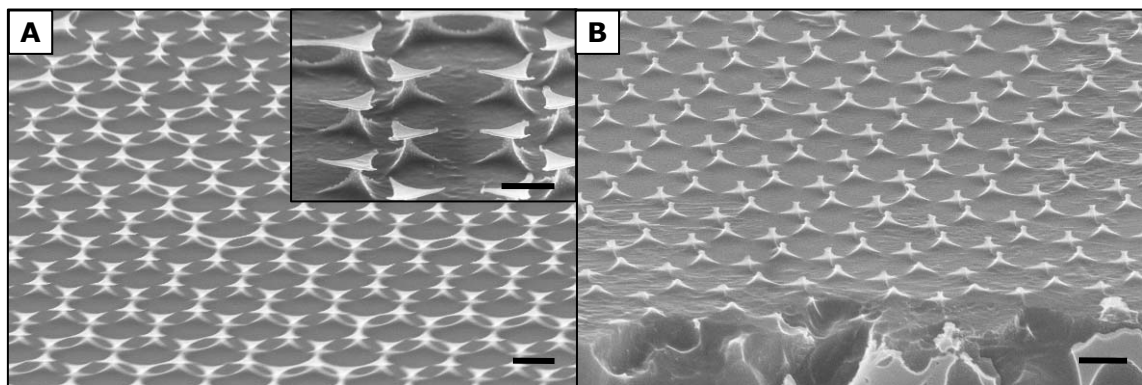
Figure 4.32. Si pillars in a honeycomb array having 1710 nm period[60] A) before Cr lift-off B) after Cr lift-off. Scale bars are 1 μm for main images and 500 nm for the inset.

In the second experiment, a PS 540 nm mask on Si is annealed for 5 s at 105 °C and subsequently etched for 50 s by the previously described oxygen RIE process (chapter 4.3, figure 4.16). After that, the sample is processed by the ICP etching process, which consists of two periodically exchanging stages: etching and passivation. During the process, the pressure in the chamber changes between (4.5 - 5.2) mTorr. The etching stage lasts for 12 s utilizing SF_6 (12 sccm) plasma. The passivation stage uses C_4F_8 (85 sccm) and lasts for 10 s. The applied power is 600 W (coil) and 12 W (platen). The whole process consists of 10 cycles, after

which arrays of silicon pillars are obtained. They are shown as a SEM images in figure 4.33. Pillars have sloped sidewalls due to PS mask erosion during the process. On the top of the pillars, there is PS mask residue visible. Pillars, on average, have heights of (268 – 297) nm as estimated from the SEM image. The diameter measured in the middle of the height range is between 77 and 104 nm.
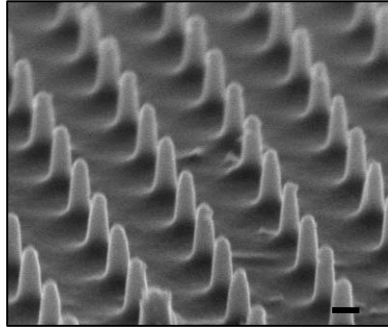
Figure 4.33. Si pillars in a hexagonal array having 540 nm period, with PS latex residue on top[60].

5. Discussion

5.1. Polystyrene mask preparation

The iridescence observed in 2D colloidal crystals is due to the diffraction of daylight (figure 4.1). It provides direct information; which part of the hexagonal colloidal crystal is monocrystalline, and which part is multicrystalline. Another independent study of the structure is performed using illumination of the sample with laser light. This method yields the diffraction pattern of hexagonally arranged spots corresponding to the six-fold symmetry of the layer. Diffraction patterns proved to be a useful technique for quality control and for crystal alignment in preparation of lines and elliptical grids. It can also be used as an analytical tool for periodicity measurement[65].

In the present work, in the very first moments of monolayer formation, the deposition agent (ethanol) delivers PS spheres to the vicinity, or directly to the air-water+electrolyte interface. Addition of sulfuric acid into PS solution has two effects on the monolayer formation. Firstly, it significantly improves the buoyancy of the spheres. Similar observations of improved buoyancy of microspheres in electrolyte solutions were also reported in the literature[65-68]. Adsorption of PS spheres at the air-water interface was studied in the literature[69], however this issue is not fully understood until now. In the present work, aside from the electrolyte, the presence of ethanol also influenced PS adsorption on the water surface (see chapter 2.3). In fact, using molecular dynamic simulations (supported by mass spectroscopy, neutron scattering and other measurements) of water/ethanol mixtures, it is concluded that amphiphilic ethanol tends to adsorb at the air-water interface and creates a monolayer with short CH_3CH_2 chains oriented vertically outside the water[70-73]. PS interfacial adsorption should be therefore enhanced by ethanol. Once PS spheres arrive at the interface, small amounts of ethanol from the PS solution will evaporate and dissolve in bulk water by diffusion and convection. Spheres are held at the interface due to hydrophobic interactions of water protruding PS spheres. Water is attracted to PS spheres via electrostatic interactions with sulfate groups. However, the surface of PS spheres is composed of a significant amount of water immiscible alkyl chains. Calculations based on Young's equation show that even for PS/water contact angles as small as 1-3°, interfacial energy well-depth corresponds to several k_BT at 298 K[69]. Therefore, once trapped, PS spheres remain at the interface. In fact, in experiments conducted in the present work, spontaneous penetration of already trapped PS spheres into bulk water is not observed.

Second effect of dissociated acid molecules in PS solution is shortening of the distances between spheres floating on the water. Electrolyte-induced coalescence is well known from Derjaguin-Landau-Vervey-Overbeek (DLVO) theory[55,74], in which free ions screen double layer repulsion competing with van der Waals attraction. In the case of 2D colloidal crystals, the interaction between spheres is more complicated due to the presence of the interface. Apart from well-known van der Waals attraction and double-layer repulsion, the interaction potential is affected by capillary forces arising either from an homogeneous[66,69,75], or from a surface-protrusion-born, inhomogeneous meniscus[76]. Additionally, dipole-dipole interactions caused by formation of asymmetric electric double-layer distributions[18,77], and water droplets on the PS spheres[66,67], affect the interaction potential. Nonetheless, this complexity of interaction forces does not drastically influence the final result. All forces, except the van der Waals dispersion interaction (London energy component), have Coulomb origins and they can be (fully or partially) screened by the ions in water. Electrostatic screening leads to dominating van der Waals

attractions and faster coalescence, manifest in the formation of monolayer multicrystallinity.

The influence of the trade-off between buoyancy of spheres and attraction of interface-trapped spheres, can be somewhat diminished by solvation stabilization. Mixing of small amounts of styrene with the PS 470 nm solution results in improved stability of the spheres and higher "elasticity" of the monolayer and is necessary for effective recrystallization. Photographs of a mask clearly indicat that the recrystallization step results in rearrangement of PS spheres, and transition of small (figure 4.1A2) into larger crystals (figure 4.1A1). Consolidation of the monolayer by application of Triton X-100 is found to be irreversible, i.e. removal of the surfactant from the interface around the monolayer in all cases leads to crack-like damage of the template. Recrystallization is risky, since too intense treatment can bring the spheres close enough to cause irreversible coalescence and destruction of long-range crystal ordering (figure 4.1A3). Respective error densities of assembled monolayers are summarized in table 4.1. No correlation between the size of the spheres and error densities is evident. A difficulty in quality reproducibility yields differences in error densities. This is no surprise, since all monolayers are prepared manually. Error densities presented here are spread over two orders of magnitude.

The linear defect density of colloidal 2D crystals, extracted from SEM images, is usually not smaller than 1 m/cm^2 and not larger than 25 m/cm^2 for PS of about 500 nm. The optical microscope image measurements of the average spacing of spheres in colloidal crystals, trapped at the interface and deposited on the substrate, reveal that there is a difference between them of only 9 nm. Such a small variation can hardly be interpreted as a real difference in structure as it is comparable with the value of standard deviation: 6 - 7 nm. Nonetheless, the homogeneous distribution of spheres in a monolayer trapped at the interface, and the number of linear defects in monolayers deposited on Si imply that the linear defects arise during the drying process. This suggests that the spheres on the water surface are not in direct contact, or that their diameter is larger in water than after drying. If so, it would be in agreement with the existence of small differences in spacing measured previously. Such effects can be attributed to the polymer swelling or to non-close-packing of the interfacial crystal.

5.2. Polystyrene mask modification

PS mask annealing.

From the obtained results, it follows that the annealing process, regardless of the method used, decreases gaps in the mask homogeneously at the same rate in all sample areas. It is possible to control annealing over time as shown in figures 4.6, 4.7A-B, 4.8G. The main drawback of this method is that during annealing the colloidal crystal is damaged. Decreasing apertures leads to creation of cracks in the PS colloidal crystal independently of the annealing technique. The density of cracks rises with the time of annealing as shown in figures 4.7D-E. Assuming that fresh masks have an average of 7 m of cracks per cm^2 (as in table 4.1), the density of cracks in these images (4.7D-E) is about 1.8 to 3.7 times bigger than in the initial state. Formation of cracks in the PS monolayer is a natural consequence of coexistence of two factors. First factor is the adhesion between spheres. Second factor is the friction (adhesion) between PS spheres and substrate, which counteracts any lateral movement of the spheres. Competition of both factors leads to formation of cracks, preferentially at the weak points of the monolayer – defects. Despite a crack formation process, using annealing methods it is still possible to decrease apertures below 40 nm. A further homogeneous decrease is impossible due to the uneven size of PS spheres in the mask. For example, the size distribution of PS 540 nm ($CV = 2.2\%$), which corresponds to almost 12 nm, is no longer negligible at the scale of 40 nm.

PS mask surface-dissolving

Decreasing apertures by the organic vapor treatment is similar to annealing. It occurs through the interaction of PS chains when spheres are in close proximity. The difference is that the mobility of PS is enhanced by the presence of THF molecules in air, unlike in annealing, where it is increased by the energy of Brownian motion. It is concluded from results in figures 4.11E and 4.12A that the most noticeable change in the size of mask interstices occurred during the final stage of PS fusion. Through the majority of experimental time (first 50 s), the aperture diminishing process is linear. During the last seconds of treatment. apertures start to disappear in a random way until all of them are closed. Polymer interdiffusion is more rapid and less homogeneous than the one observed for annealing. For example; for the same size of PS particles (540 nm), annealing decreased apertures down to $\approx$ 40 nm and all gaps are open (figure 4.7B and 4.8E). Whereas with the surface dissolving process, the smallest achieved apertures are $\approx$ 100 nm and about 30% of the gaps are already closed (figure 4.11E). The increased intermixing rate of PS hydrocarbons in the final stage of the process arise due to van der Waals attraction, which is much stronger at shorter (than at longer) distances. The difference in homogeneity of annealing and surface dissolving arises due to the fact that dispersion attraction, which dominates the van der Waals force, depends mainly on the difference of refractive indices between PS spheres and the surrounding medium[54]. This difference is larger for the pair PS/air (n_{PS} - n_{air} = 0.55) than for the PS/THF system (n_{PS} - n_{THF} = 0.15), which implies that PS interacts stronger through THF vapors than through air.

Similarly to annealing, surface dissolving processes create stress in the monolayer and consequently cause crack-like damage. Due to the aforementioned obstacles, this method is found to be impractical for the design of apertures smaller than about 100 nm.

PS mask coating with silica

Coating of the PS mask with silica via hydrolysis of tetraethoxysilane decreases the apertures homogeneously and linearly as shown in figure 4.9F. In some experiments, small quantities of silica precipitated on the mask in the form of nanoparticles – figure 4.9A-C. Other samples prepared in the same way proved that the amount of silica nanoparticles, formed each time, can be different. Since the coating procedure is the same in all experiments, the explanation for unwanted silica formation is presumably the mixing of solutions during silica shell preparation. An increased rate of collisions between molecules results in the formation of new silica particles, which can grow over time and adsorb on the PS mask. Therefore, via decreasing the probability of intermolecular collisions it is possible to decrease the mask contamination. Silica coating does not generate new cracks in the PS mask – the number of cracks after silica covering (3 m/cm^2 and 6 m/cm^2) is comparable with the number of cracks in a standard average mask (7 m/cm^2). At the same time, silica preferentially accumulates at multilayer defects or at point defects making them bigger.

An important issue is that silica easily deposits on silica or silicon substrates. It is found that silica preferably deposits at contact areas between mask and substrate (4.9G). However, this obstacle can possibly be overcome by terminating the surface of the substrate with a blocking agent.

5.3.   Etched PS mask

The PS etching procedure, found via experimental trials (figures 4.13 - 4.16), is feasible for PS spheres of various sizes (figure 4.17). Due to simultaneous PS mask and substrate etching, mixtures of CF_4/O_2 gases (figures 4.13 and 4.14) are found

to be less favorable than Ar/O$_2$ (figure 4.16B-G) for which the selectivity is much better.

Disruption of the colloidal crystal structure (figure 4.14A), caused by the plasma, treatment can be effectively inhibited by 4 – 6 s pre-annealing of a mask at 105 °C before RIE – figure 4.15C. For the spheres of 540 nm diameter (535 nm as measured using SEM micrograph in figure 4.16A), the method provides the smooth diameter reduction down to 129 nm (figure 4.16F), which is about 24% of the original size. The differences in the etching rate observed in figure 4.17 indicate that each etching process shows small differences in i.e. electric field homogeneity and gas flow. These are attributed to several issues. A few small (1x1 cm) samples are being etched at a time; while an etcher was designed to process one wafer (10 cm diameter) at a time. This introduces a necessity of using a wafer support, on which the sample is lying during the process. The edges of samples can perturb the flow of etching gas and thus affect the etching rate. Differences between the electrical conductivity of a sample substrate and supporting wafer influence locally the homogeneity of the electric filed, which also influences the etching rate. Despite small differences, the etching characteristic remains linear and the amount of etched material is proportional to the RIE period as shown in figure 4.17. A slight nonlinearity at the beginning of the etching characteristics is attributed to the plasma ignition and stabilization in the early stage of the process, when the etching is not as efficient as when the plasma is stable. Figure 4.17 shows the behavior of PS 540 nm spheres during the etching process. For different PS sizes the RIE process could be modified accordingly to specific length-scales in order to etch in convenient etching periods. Results of argon dilution or reduction of oxygen flow rate (presented in figure 4.15B), can help in achieving finer diameter control convenient for etching of small-sized PS spheres. On the other hand, higher oxygen flow rates with less or no argon admix resulting in higher etch rates, shown in figure 4.15A, can be applied to speed up etching of larger spheres. It is important to bear in mind that small oxygen-to-argon ratios can cause redeposition of etched material on the sample[58], as shown in figure 4.15C. In figure 4.17C it is found that some of the PS particles after etching possess small features at the edges, pointing outwards in the directions of the neighboring spheres. Such features can arise due to surface melting and polymer interdiffusion between the spheres in the early stages of etching. Such behavior of PS spheres can be induced by the ionic bombardment and elevated temperature of PS at the surface of the spheres. As the mask is etched, the "polymer connections" between PS spheres are broken, and the features disappear in the next stage of RIE processing. An extensive research on etching using spheres can be found in the literature[14,15,39,78,79].

5.4. Nanostructures

Geometrical relationships in nanoparticle arrays prepared by SNSL derived within this work have been compared with experimental measurements. Some of these expressions have already been published in external works[13]. All formulas derived from geometrical analysis allow prediction of distances, sizes, and coverage factors, which is consistent with the range of measurement error. These predictions are convenient tools in experimental planning and provide instant information about preparation limits.

Triangles and dots

Spacing, S_p, in arrays of triangles and surface coverage factors (SC) are in perfect agreement with calculated values (table 4.2). The size of triangles, h_p, depends on the contact area between spheres in the mask, which in turn depends on the internal pressure between spheres created during crystal preparation. Due to an insufficient number of the samples investigated it is not possible to find out, how precisely the values of the contact area diameter d expressed as a fraction of PS

diameter (14% for PS 1710 nm, 24% for PS 980 nm and 19% for PS 496 nm) depend on the PS sphere size. Value d depends on an internal pressure between spheres in the monolayer, which in turn depends on an amount of the surfactant used in step 4 of the monolayer preparation (chapter 2.2 and 3.2). In consequence, triangle size values h_p, expressed as a fraction of PS spheres diameter, also show variance (30%, 25% and 27% for PS 1710 nm, 980 nm and 496 nm respectively), but all values are below the theoretical h_p value (37%), which is calculated for a contact area d equal to 0 (contact point). Evaporation of thick layers, through the PS mask has created tetrahedrons (figure 4.20). For PS 1710, 980 and 540 nm, the maximum height of particles is determined from AFM images: 540, 380 and 120 nm respectively. Above these evaporation thicknesses, masks become closed due to deposition of metal at the edges of apertures. Nanoparticles created via evaporation through an annealed PS 540 nm mask (dots) have diameters of about 40 nm. Monodisperse dots, having diameters below 40 nm, cannot be prepared efficiently, since at these length-scales, the homogeneity of apertures in the PS mask is lost. In some samples PS residue is found in-between nanoparticles (figure 4.20B), similar to that observed literature[80]. This is due to incomplete lift–off process and can be removed by additional cleaning step.

Rods

It occurs that dimensions of rods obtained by SEM and AFM (figure 4.22C-B) differ significantly. This difference has been attributed to the presence of a string of nanoparticles surrounding each nanorod. The existence of such a string of particles around a nanorod, may indicate that originally the nanorod could have been bigger, but has shrunk during or after preparation, in between acquisition of SEM and AFM images. To resolve this question, more detailed tests are required. During the preparation of rods, the incident angle is periodically changing from – 30° to + 30°. At given dimensions of the system (evaporation of 100 nm of gold through a PS 540 nm mask with apertures of about 60 nm), according to equation 2.17, the rods should have been 267 nm long and 22 nm thick. Values measured by microscopes are between 174 nm and 194 nm for length and 25 ± 7 nm for thickness. There are several reasons, which can contribute to this difference. One explanation can be the aforementioned nanorod-shrinking phenomenon. The calculated length, 267 nm, corresponds well to the length of the nanorods measured including the surrounding nanoparticle string, which is around 256 nm (SEM) – 279 nm (AFM). Furthermore, the equation 2.17 does not take into account that the length of the rod is defined by curvature of spheres and the orientation of rods. In consequence, there is a compartment of incident evaporation angle outside which, the evaporated material will deposit on the sphere instead of the substrate. Finally, the thickness of an aperture T in figure 2.15 is assumed to be equal to the diameter of the contact area between spheres d (figure 2.9C). It is not clear how valid this approximation is, because the value T is never measured directly.

Cups and Rings

Rings that have been prepared by evaporation through silica-modified masks are not perfectly round. The reason for this kind of morphology is the triangular shape of an aperture. Perfect rings are feasible only when round apertures are employed in the evaporation process. Analysis of the size of rings (table 4.5) has shown that rings can be described by equation 2.18 within experimental accuracy. As expected, the thickness of ring particles decreases with increasing ring diameter. Particles having larger diameters can overlap creating an interconnected net of rings (figure 4.24C). Residual spots remaining among rings are composed of silica and are residues after the mask modification process. Formation of the residue could possibly be inhibited by an earlier modification of silicon surface with a blocking agent. Cr cups with nickel dots inside, presented in figure 4.25, are prepared in the early stages of research, where aperture-decreasing methods are unknown. At the

present stage of development, even more homogeneous and symmetrical structures should be possible like the ones simulated in the literature[81].

Grids

It is found that surface coverage of grids created by the EBE process (figure 4.26), is in good agreement with values calculated from 2.9. In image 4.26D, white spots visible at the edges of grids are pieces of a metal layer that covers the spheres. The presence of these scraps indicates that the critical evaporation thickness has been achieved and evaporation of more material would result in a closed layer – similar to the one which is covering the sample presented in image 4.26E. The critical evaporation thickness is related to the shape and size of etched spheres and decreases with decrease of the height of a sphere. For etched spheres with lateral size of 161 nm (figure 4.26D), the critical evaporation thickness is 22 nm. This value can be increased by finding etching conditions, in which spheres are decreased isotropically, i.e. by increasing the pressure and decreasing the plasma energy. In the performed experiments it is found that NMP removes PS more precisely than THF. At the same time it is less volatile and less harmful, which makes it a better stripping agent. Finally, the aging test result shows that gold grids deposited on a sapphire with an intermediate layer of titanium are not stable. After 160 days of the storage in ambient conditions significant changes in the morphology take place and a layer appears to be covered with particles (figure 4.28B). The process of nanoparticle formation proceeds at the cost of the layer thickness and, presumably, is driven by the room temperature (18 – 25 °C) diffusion.This drawback has to be resolved for applicability of such structures as micro- or nanostructured devices.

Lines

Measured values of width, spacing, thickness, and surface coverage are in good agreement with calculated values as is summarized in table 4.7. In between lines there are bright circles visible, which are the residual PS sphere fractions adhered to the substrate. This kind of residue accompanies structures prepared by NSL or SNSL, as it is shown in previous chapters. More rigorous lift-off treatment, as the one applied to gold grids in this work, improves removal of unwanted PS residue. The shape of the lines is not as simple in the case of the adapted model (figure 2.13D). Lines shown in figure 4.30 have been evaporated at the incident angle $\theta = 62°$ and they possess lateral protrusions. These protrusions can be minimized using bigger θ angles, but then the thickness of lines decreases as well. Images in figure 4.31A confirm that the mask prepared on this sample is indeed made of a single colloidal crystal and furthermore, they show disturbances of the structure. Cracks in the PS mask result in increased width of line defects or new gaps created in lines. Point defects produce gaps only.

Pillars

Due to extensive literature written about etching of colloidal crystals[39,79,82–89], structures shown in the present work (figures 4.32 and 4.33) are not studied in detail. The presented structures are just a few examples of 3D patterns available by processing of colloidal crystals.

6. Outlook

The method of nanosphere lithography (NSL) allows preparation of masks not only on flat surfaces: a colloidal crystal prepared at an air-water interface can be easily deposited on a 3D object of any shape. The uniformity of the covering of such objects depends on their specific morphology. Convex morphologies are supposed to be covered more evenly, while concave areas are supposed to remain partially or entirely uncovered.

In the present work, it is shown that different types of annealing and organic vapour treatment produce crack errors in the periodic structure. This is due to the fact that polystyrene (PS) spheres in a monolayer have a much bigger surface than a continuous layer would have. Elevated temperature or the presence of the solvent vapours triggers the cohesion force to convert the system into a configuration of lower free-surface energy.

However, using the silica covering technique does not lead to the formation of new cracks in the monolayer. The PS mask is preserved in its original state and the silica is deposited onto its surface without any changes caused to the spheres. Success of silica covering suggests that other techniques, which can deposit material on a monolayer at temperatures below the glass transition (T_g), should be employed to decrease the size of the apertures in the mask. One such method is electron beam evaporation (EBE). As is shown in chapter 2.6.2 the EBE process at grazing incident angles θ is capable of modifying spheres without structuring the substrate. Such a process could efficiently and precisely lower the dimension of mask interstices.

PS colloids, due to relatively low T_g temperatures, can be modified by an air flow at a temperature above T_g. The direction change of an air flow allows PS spheres to be formed into arbitrary shapes. The length of elongated PS spheres is limited by their volume. However, it should be possible to "write" simple shapes with PS; for example, elongated or C-shaped particles. A similar approach is used to modify the shape of water microdroplets condensed on the surface of organic solvent containing gold nanoparticles[90].

Preparation of ring nanoparticles, shown in chapter 4.6, can be improved by simple modification of the EBE setup, e.g. the insertion of a shutter having a specific shape between evaporation source and rotating sample. This would enable screening of a sample from deposition over a chosen section of sample rotation. For example, evaporation of a rotating sample at the angle of incidence $\theta = 10°$, and using a diaphragm that screens the sample over 1/6 part of the revolution would create an array of C-shaped particles, which could be useful; for example, to study negative refraction[91].

The NSL can be used as a patterning technique and further combined with replication techniques, for example with soft lithography or wet etching. Such attempts have already been performed by Xia[92]. This combined preparation method would yield maximized repeatability of the structures.

The produced arrays of nanoparticles presented in this work are useful systems to study various physical phenomena like interaction of metals confined in small volumes of various morphologies with light[93-99], magnetic properties[51,100,101], and ferroelectric properties[102]. Arrays of nanoparticles can be used for the catalytic growth of arrays of aligned rods, which might be used as photonic crystals[47], field emitters[45], or nanolaser arrays[36]. Furthermore, structures produced using colloidal crystals have potential applications or have been used as ultrasensitive biosensors[40], DNA electrophoresis[41], superhydrophobic materials[42], light emitting

diode (LED) arrays[44], optical antennas[46], polymer membranes[48], nanocrystals synthesis [49], protein micropatterning[50], and microlense arrays[43].

7. Summary

The present work introduces shadow nanosphere lithography (SNSL), which is a time-efficient lithographic method. It uses 2D colloidal crystals made of polystyrene (PS) spheres that serve as a lithographic mask. Evaporation material is deposited on the mask at various incident angles producing particles of various shapes on the substrate. In this way, simply by changing the orientation of the sample relative to the evaporation source, it is possible to "write" nanoparticles in an hexagonal matrix. In comparison to other lithographic techniques, such as electron beam lithography (EBL), this method substantially lowers the cost of preparation of nanostructured samples. The present work demonstrates that PS spheres can be arranged into large area monolayers (≈ 200 cm^2) having large (>20 cm^2) 2D colloidal monocrystals. As in classical crystals, colloidal monolayers also have structural errors incorporated. In average monolayers, assembled of 540 nm diameter PS spheres, the number of point defects is about 1.6×10^6 cm^{-2}. Prepared colloidal masks are used to manufacture periodic arrays of such particles like dots, triangles, rods, rings, cups, meshes, and wires.

Reactive ion etching, annealing, silica deposition, and organic vapor induced polymer interdiffusion are used to modify the size of interstices between spheres, in a controllable manner. Annealing and organic vapor induced polymer interdiffusion methods are not as successful at decreasing apertures as silica deposition, due to formation of cracks in PS masks. The origin of the crack formation is related to the fact that the spheres undergo polymer interdiffusion and to the balance between two forces: adhesion between PS spheres and adhesion between PS spheres and substrate. Silica deposition is a technique, which covers spheres in the mask with a thin silica shell. This process does not affect the inner structure of PS spheres, and therefore the crystal order is preserved. However, silica-modified PS masks produce silica residues on the substrate, which are hard to remove. These obstacles should not be present in a novel method for mask modification. Thermal evaporation of a material at a grazing incident angle $\theta = (80 - 85°)$ on the rotating sample should decrease mask apertures precisely and without contamination of the substrate.

Geometrical relations describing the nanoparticle size dependences on the experimental conditions have been derived for each kind of particle. Experimental and calculated sizes agree with each other within the measurement error range. Particles as small as 40 nm could routinely be produced. In another set of experiments, reactive ion etching is used to achieve masks with non-close packed arrays of PS spheres. Evaporation of material through etched spheres results in a layer perforated with spherical meshes. At increased evaporation incident angles, oval meshes or a structure of parallel lines are deposited. It is found that gold-perforated layers exhibit a thermodynamic morphology change, which occurs already at room temperature after 160 days.

The large size (1x1 cm) of well-ordered matrices, produced by SNSL, allow the use of macroscopic examination methods, which make the measurements much easier than in the case of single nanostructures. Furthermore, control of spacing, which covers a range of tens of nm – hundreds of microns, allows studying interactions and coupling effects between nanoparticles or individually occurring phenomena at various length scales.

The aforementioned advantages, together with low-cost requirements, make it a perfect method for preparation of prototype devices. Colloidal masks might be used as photonic crystals, field emitters or nanolaser arrays. Furthermore, they have potential applications as ultrasensitive biosensors, DNA electrophoresis, superhydrophobic materials, light emitting diode (LED) arrays, optical antennas,

polymer membranes, nanocrystals synthesis, protein micropatterning, assemblies and microlens arrays.

8.   Appendix

8.1.   Abbreviations and symbols

2D – two-dimensional

AFM – atomic force microscope(y)

DUVIL – deep ultraviolet immersion lithography

DUVL – deep ultraviolet

EBE – electron beam evaporation

EBL – electron beam lithography

EUVL – extreme ultra violet lithography

HCP – hexagonal close packed

IBL, FIB – ion beam lithography, focused ion beam

IL – interference lithography

LB – Langmuir-Blodgett

MOPL – maskless optical projection lithography

NMP – 1-methyl 2-pyrrolidone

NSL, CL, SNSL – nanosphere lithography, colloidal lithography, shadow nanosphere lithography

OPL – optical projection lithography

PL – photolithography

PS – polystyrene

PS 470 nm – PS spheres having diameter 470 nm

RIE – reactive ion etching

SC1 – standard cleaning solution 1: 7% NH_4OH/30% H_2O_2/Milli-Q water (1:1:5) by volume

sccm – standard cubic cm (cubic cm at standard pressure and temperature)

SEM – scanning electron microscope(y)

SFIL – step and flash lithography

SL – soft lithography

SPM – scanning probe lithography

THF – tetrahydrofuran

XRL – x-ray lithography

ZPAL – zone plate array lithography

Symbols

CV – coefficient of variation

k_BT – thermal energy

T_g – glass transition temperature

θ – incident angle of evaporation

D_0 – sphere diameter

D – etched sphere diameter

d – effective diameter of the contact area between two spheres in a 2D HCP mask

n – evaporation penetration length (details: chapter 2.6.2)

P_0 – set thickness of the evaporation layer

P – thickness of a structure

h_p – triangle height – triangular particle in-plane size or aperture diameter

SC – surface coverage = area fraction covered by the nanostructure, normalized to the whole area of the sample

S_p – spacing of the particles

W_t – thickness of a mesh wall in a metal grid

W – width of a structure

A_0 – diameter of an aperture

L_0 – length of a rod

A_e – effective aperture size

C_0 – length of the average circumference of the ring shaped particle


8.2. Table of materials used

No.	Name; article No.; batch No.	Company	Description
1	Sapphire wafer; ALA76D05C2; PO#51214/05	MTI corporation, USA	Formula: Al_2O_3 (α), A-plane crystal; purity 99.99%; Surface roughness <0.5 nm
2	Silicon wafer; SIA76B05D4; PO#81624/05	Si-Mat Silicon Materials	Formula: Si; <100>; purity 99.99%; Surface roughness <1 nm
3	Surfactant-free sulfate white polystyrene latex PS 470 nm; 1-500; 1713	Interfacial Dynamics Corporation (IDC), USA	Dispersed in de-ionized water; Diameter: 470 nm; CV = 2.6%; Surface with sulfate groups; negatively charged: 4.9 $\mu C/cm^2$; Percent solids: 6.9 g/100 ml;
4	Surfactant-free sulfate white polystyrene latex PS 540 nm; 1-500; 2028	Interfacial Dynamics Corporation (IDC), USA	Dispersed in de-ionized water; Diameter: 540 nm; CV = 2.2 %; Surface with sulfate groups; negatively charged: 6.3 $\mu C/cm^2$; Percent solids: 8 g/100 ml;
5	Polystyrene plain particles PS 980 nm; PS-R-1.0; PS-R-B288	Microparticles GmbH	Dispersed in de-ionized water; Diameter: 980 nm; CV = 4%; Surface with sulfate groups; negatively charged; Percent solids: 8%;
6	Polystyrene plain particles PS 1710 nm; PS-R-1.7;	Microparticles GmbH	Dispersed in de-ionized water; Diameter: 1710 nm; CV = 1.2%; Surface with sulfate groups;

	PS-R-L690		negatively charged; Percent solids: 10%
7	Poly(methyl metacrylate) particles PMMA 1060 nm; PMMA-R-1.0; PMMA-F-L1057-1	Microparticles GmbH	Dispersed in de-ionized water; Diameter: 1060 nm; Percent solids: 10%
8	1-methyl 2-pyrrolidone (NMP); 8.06072.1000	Merck	C_5H_9NO, pure for analysis (99.5%)
9	Ethanol (EthOH); 9065.4	Carl Roth GmbH	C_2H_6O, pure for analysis (99.8%)
10	2-Propanol; 6752.4	Carl Roth GmbH	C_3H_8O, pure for analysis (99.7%)
11	Acetone; 9372.5	Carl Roth GmbH	C_3H_6O, pure for analysis (99.8%)
12	Styrene; S497-2; Lot#S14456-243	Sigma-Aldrich	C_8H_8, 99%
13	Ammonia water solution 28-30%; 1.05423.1000	Merck	NH_5O, pure for analysis
14	Hydrogen Peroxide 35%; 9683.1	Carl Roth GmbH	H_2O_2, pure, stabilized
15	Sulfuric acid 96%; 9316.2	Carl Roth	H_2SO_4, pure
16	MiliQ water: PURELAB MAXIMA	USF ELGA	Ultra-pure, de-ionized water (18.2 MΩcm)
17	Triton X100; 234729	Sigma-Aldrich	$4\text{-}(C_8H_{17})C_6H_4(OCH_2CH_2)_nOH$, n~10
18	Tetraethoxysilane TES	Sigma-Aldrich	$(C_2H_5O)_4Si$, pure for analysis
19	Tetrahydrofuran THF; 4745.3	Carl Roth GmbH	C_4H_8O, pure for analysis (99.5%)

8.3. Calculations

Equation 2.1
$$\theta = \arccos(\sqrt{2\sqrt{3}-3}) = 47.1°$$
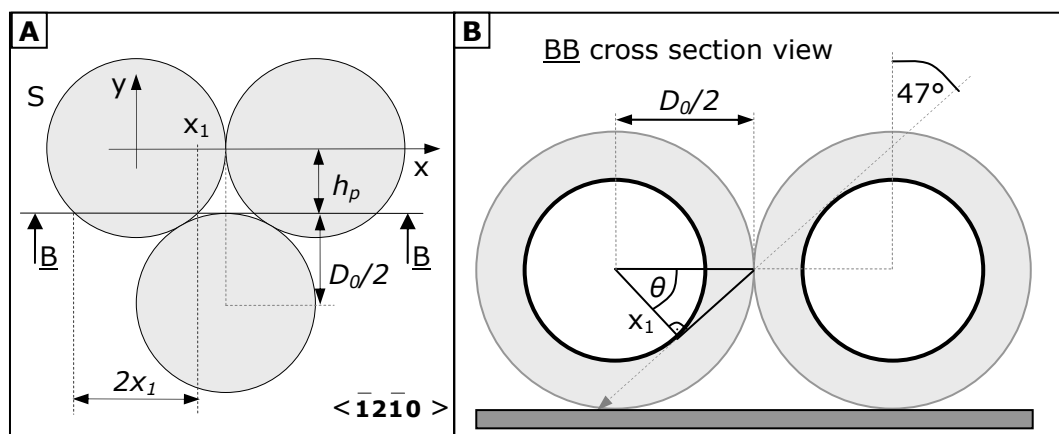
Figures adapted from figure 2.9A, B (chapter 2.6.2). A) Scheme of PS mask with a section line BB showing $<\bar{1}2\bar{1}0>$ colloidal crystal direction. B) PS mask cross-section view along line BB.

In order to find a critical evaporation angle θ for conditions depicted in figure 2.9, a dimension x_1 has to be found. It is calculated by substituting the value $y = -h_p$ into the circle equation of the sphere S indicated in the figure (A), where the circle S intersects with line BB.

The edge of the S sphere, in 2D, is described by Eq. 1:

$$x^2 + y^2 = \left(\frac{D_0}{2}\right)^2$$

Eq. 1

Where D_0 is the sphere diameter. Substituting $y = -h_p = -\dfrac{D_0(\sqrt{3}-1)}{2}$ (equation 2.5 for (d = 0), chapter 2.6.2) into Eq. 1 and solving it results in:

$$x_1 = \left(\frac{D_0}{2}\right)\sqrt{2\sqrt{3}-3} = 0.34 D_0$$

Eq. 2

From the sketch in figure (B) it follows that:

$$\cos\theta = \frac{2x_1}{D_0}$$

Eq. 3

Substituting Eq. 2 into Eq. 3, results in:

$$\cos\theta = \sqrt{2\sqrt{3}-3}$$

Eq. 4

Therefore, the critical value of the incident evaporation angle is given by:

$$\theta = \arccos(\sqrt{2\sqrt{3}-3}) = 47.1°$$

Eq. 5

Equation 2.2
$$\theta = \arccos(\frac{1}{2}(\frac{d}{D_0}+1))$$

The critical evaporation angle θ for $<\bar{1}100>$ PS crystal direction is calculated using relationships obtained from triangles (I, II, III) depicted in the figure 2.9C.
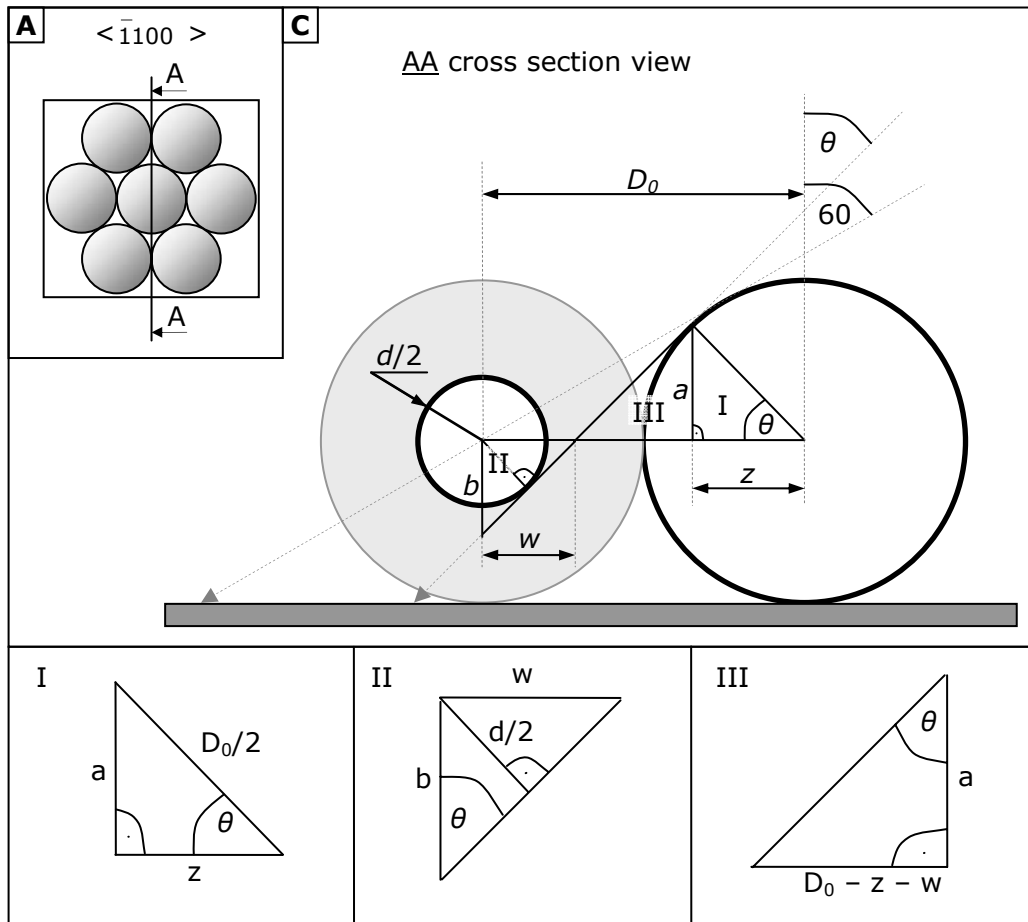
Figures adapted from figures 2.9A and C (chapter 2.6.2). A) Scheme of PS mask with a section line <u>AA</u> showing $<\bar{1}100>$ colloidal crystal direction. C) PS mask cross-section view <u>AA</u>. Triangles I, II, and III, for clarity, are shown separately – on the bottom of the scheme.

In triangle 'I' values a and z can be expressed by:

$$a = \frac{D_0 \sin \theta}{2} \qquad\qquad \text{Eq. 1}$$

$$z = \frac{D_0 \cos \theta}{2} \qquad\qquad \text{Eq. 2}$$

Where D_o is the diameter of the PS sphere, d is the diameter of the contact area between PS spheres, and θ is the incident angle of evaporation.

In triangle 'II' values b and w can be expressed by:

$$b = \frac{d}{2\sin\theta} \qquad\qquad \text{Eq. 3}$$

$$w = b\tan\theta \qquad\qquad \text{Eq. 4}$$

Substituting Eq. 3 into Eq. 4 results in:

$$w = \frac{d}{2\sin\theta}\tan\theta \qquad\qquad \text{Eq. 5}$$

From the triangle 'III' there follows a relationship between the angle θ depending on D_0, z, w, which can be written as:

$$\tan\theta = \frac{D_0 - z - w}{a} \qquad\qquad \text{Eq. 6}$$

Substituting Eq. 1, Eq. 2, and Eq. 5 into Eq. 6 gives an expression, which can be written as:

$$\theta = \arccos(\frac{1}{2}(\frac{d}{D_0} + 1)) \qquad\qquad \text{Eq. 8}$$

Equation 2.4 $\qquad\qquad P = \frac{D_0}{2}\left(\sqrt{1 + \frac{4P_0}{\pi D_0}} - 1\right)$

A 2D model is used for calculating the thickness P of a deposit, which is created during evaporation of some material onto a rotating sphere in the area where the atom flux is orthogonal to the sphere surface. The thickness P is calculated from the fact that the black fields F_A and F_B in the figure 2.11 are equal.
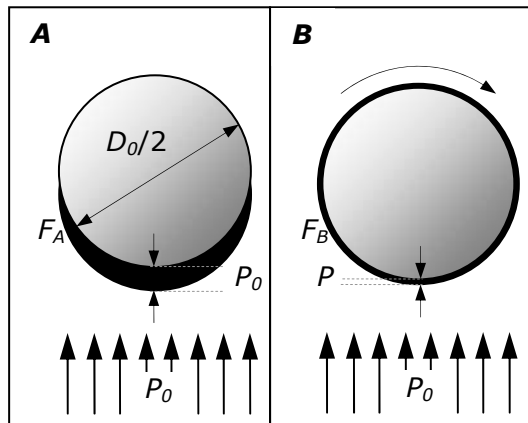
The figure is copied from figure 2.11 (chapter 2.6.2). Schematic of evaporation of material on a sphere without (A) and with rotation (B). D_0 is the diameter of the sphere, P_0 is the value set of deposit thickness, and P is the thickness deposit on the rotating sphere.

Fields F_A and F_B are expressed by the following expressions:

$$F_A = P_0 D_0 \qquad\qquad \text{Eq. 1}$$

$$F_B = \pi P D_0 + \pi P^2 \qquad\qquad \text{Eq. 2}$$

where P_0 is a given thickness of an evaporated layer and D_0 is a diameter of the PS sphere.

From the equality of these fields, it follows that:

$$\pi P^2 + \pi P D_0 - P_0 D_0 = 0 \qquad \text{Eq. 3}$$

This square trinomial has only one physically meaningful (positive) solution:

$$P = \frac{D_0}{2}\left(\sqrt{1 + \frac{4P_0}{\pi D_0}} - 1 \right) \qquad \text{Eq. 4}$$

End.

Equation 2.17 $\qquad P = P_0 \cos\theta \dfrac{A_0 \cos\theta - T \sin\theta}{L_0}$

The thickness of rods evaporated through the modified PS mask depends on several factors: evaporation thickness P_0, aperture size A_0, and the incidence angle of evaporation θ.
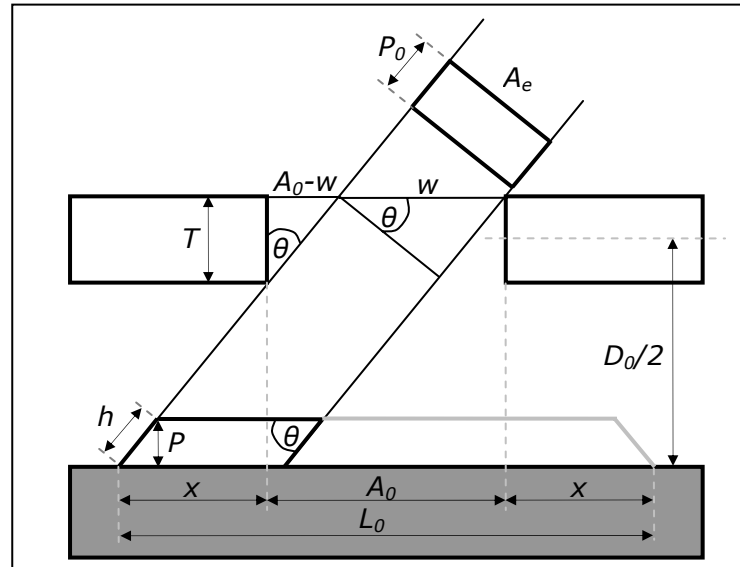
The figure is adapted from figure 2.15 **(chapter 2.6.5). Scheme of an aperture in PS mask approximated with rectangular gap. Tilting the substrate from + θ to - θ creates rods of length L$_0$. The effective size of the aperture depends on θ.**

From the above scheme following relationship can be written:

$$P = h\cos\theta \qquad \text{Eq. 1}$$

which describes thickness of the structure P evaporated at given incident angle θ. Furthermore, the dimension h depends on the initial thickness value P_0 evaporated through the effective aperture A_e, and a length of the nanorod L_0 as follows:

$$h = \frac{P_0 A_e}{L_0} \qquad \text{Eq. 2}$$

The equation for the effective aperture A_e can be calculated from the following relationships:

$$w = A_0 - T \tan \theta \qquad\qquad\qquad \text{Eq. 3}$$

and

$$A_e = w \cos \theta \qquad\qquad\qquad \text{Eq. 4}$$

where T is an aperture thickness and A_0 is the aperture size after PS mask modification. Inserting Eq. 3 into Eq. 4 and simplifying the result, it can be written that:

$$A_e = A_0 \cos \theta - T \sin \theta \qquad\qquad\qquad \text{Eq. 5}$$

Substituting Eq. 5 and Eq. 2 into Eq. 1 a final thickness profile function $P(\theta)$ is obtained:

$$P = P_0 \cos \theta \frac{A_0 \cos \theta - T \sin \theta}{L_0} \qquad\qquad\qquad \text{Eq. 6}$$

9. Literature

1. K. E. Drexler. *Nanosystems: Molecular Machinery, Manufacturing, and Computation*. John Wiley & Sons Ltd., New York (1992)

2. K. E. Drexler. *Engines of Creation: The Coming Era of Nanotechnology*. Anchor Books, USA (1986)

3. J. S. Hall. *Nanofuture : What's Next For Nanotechnology*. Prometheus Books, New York (2007)

4. National Science Foundation. http://www.nsf.gov/crssprgm/nano/reports/omb_nifty50.jsp (2007)

5. J. C. Hulteen, D. A. Treichel, M. T. Smith, M. L. Duval, T. R. Jensen, and R. P. Van Duyne. *Nanosphere lithography: Size-tunable silver nanoparticle and surface cluster arrays*. Journal of Physical Chemistry B **103,** 3854 (1999)

6. R. D. Allen, G. M. Wallraff, D. C. Hofer, and R. R. Kunz. *Photoresists for 193-nm lithography*. IBM Journal of Research and Development **41,** 95 (1997)

7. *Article: "IBM Develops 29.9nm Circuit"*. (2-21-2006)

8. D. Bratton, D. Yang, J. Y. Dai, and C. K. Ober. *Recent progress in high resolution lithography*. Polymers for Advanced Technologies **17,** 94 (2006)

9. M. Rothschild, A. R. Forte, R. R. Kunz, S. C. Palmateer, and J. H. C. Sedlacek. *Lithography at a wavelength of 193 nm*. IBM Journal of Research and Development **41,** 49 (1997)

10. B. D. Gates, Q. B. Xu, M. Stewart, D. Ryan, C. G. Willson, and G. M. Whitesides. *New approaches to nanofabrication: Molding, printing, and other techniques*. Chemical Reviews **105,** 1171 (2005)

11. R.Menon, A.Patel, D.Gil, and H.I.Smith. *Maskless lithography*. Materials Today **8,** 26 (2005)

12. T. A. Savas, M. L. Schattenburg, J. M. Carter, and H. I. Smith. *Large-area achromatic interferometric lithography for 100 nm period gratings and grids*. Journal of Vacuum Science & Technology B **14,** 4167 (1996)

13. C. L. Haynes, A. D. McFarland, M. T. Smith, J. C. Hulteen, and R. P. Van Duyne. *Angle-resolved nanosphere lithography: Manipulation of nanoparticle size, shape, and interparticle spacing*. Journal of Physical Chemistry B **106,** 1898 (2002)

14. H. W. Deckman and J. H. Dunsmuir. *Applications of Surface Textures Produced with Natural Lithography*. Journal of Vacuum Science & Technology B **1,** 1109 (1983)

15. H. W. Deckman and J. H. Dunsmuir. *Natural Lithography*. Applied Physics Letters **41,** 377 (1982)

16. A. Kosiorek, W. Kandulski, P. Chudzinski, K. Kempa, and M. Giersig. *Shadow nanosphere lithography: Simulation and experiment*. Nano Letters **4,** 1359 (2004)

17. U. C. Fischer and H. P. Zingsheim. *Sub-Microscopic Pattern Replication with Visible-Light*. Journal of Vacuum Science & Technology **19,** 881 (1981)

18. P. Pieranski. *Two-Dimensional Interfacial Colloidal Crystals*. Physical Review Letters **45,** 569 (1980)

19. C. L. Haynes and R. P. Van Duyne. *Nanosphere lithography: A versatile nanofabrication tool for studies of size-dependent nanoparticle optics*. Journal of Physical Chemistry B **105,** 5599 (2001)

20. P. N. Bartlett, P. R. Birkin, and M. A. Ghanem. *Electrochemical deposition of macroporous platinum, palladium and cobalt films using polystyrene latex sphere templates*. Chemical Communications **,** 1671 (2000)

21. T. R. Jensen, G. C. Schatz, and R. P. Van Duyne. *Nanosphere lithography: Surface plasmon resonance spectrum of a periodic array of silver nanoparticles by ultraviolet-visible extinction spectroscopy and electrodynamic modeling*. Journal of Physical Chemistry B **103,** 2394 (1999)

22. N. D. Denkov, O. D. Velev, P. A. Kralchevsky, I. B. Ivanov, H. Yoshimura, and K. Nagayama. *Mechanism of Formation of 2-Dimensional Crystals from Latex-Particles on Substrates*. Langmuir **8,** 3183 (1992)

23. R. Micheletto, H. Fukuda, and M. Ohtsu. *A Simple Method for the Production of A 2-Dimensional, Ordered Array of Small Latex-Particles*. Langmuir **11,** 3333 (1995)

24. P. Tessier, O. D. Velev, A. T. Kalambur, A. M. Lenhoff, J. F. Rabolt, and E. W. Kaler. *Structured metallic films for optical and spectroscopic applications via colloidal crystal templating*. Advanced Materials **13,** 396 (2001)

25. F. Burmeister, W. Badowsky, T. Braun, S. Wieprich, J. Boneberg, and P. Leiderer. *Colloid monolayer lithography-A flexible approach for nanostructuring of surfaces*. Applied Surface Science **145,** 461 (1999)

26. P. Hanarp, D. S. Sutherland, J. Gold, and B. Kasemo. *Control of nanoparticle film structure for colloidal lithography*. Colloids and Surfaces A-Physicochemical and Engineering Aspects **214,** 23 (2003)

27. R. C. Rossi, M. X. Tan, and N. S. Lewis. *Size-dependent electrical behavior of spatially inhomogeneous barrier height regions on silicon*. Applied Physics Letters **77,** 2698 (2000)

28. K. U. Fulda and B. Tieke. *Langmuir Films of Monodisperse 0.5-Mu-M Spherical Polymer Particles with A Hydrophobic Core and A Hydrophilic Shell*. Advanced Materials **6,** 288 (1994)

29. A. L. Rogach, N. A. Kotov, D. S. Koktysh, J. W. Ostrander, and G. A. Ragoisha. *Electrophoretic deposition of latex-based 3D colloidal photonic crystals: A technique for rapid production of high-quality opals*. Chemistry of Materials **12,** 2721 (2000)

30. M. Giersig and P. Mulvaney. *Preparation of Ordered Colloid Monolayers by Electrophoretic Deposition*. Langmuir **9,** 3408 (1993)

31. J. P. Hoogenboom, C. Retif, E. de Bres, M. V. de Boer, A. K. van Langen-Suurling, J. Romijn, and A. van Blaaderen. *Template-induced growth of close-packed and non-close-packed colloidal crystals during solvent evaporation*. Nano Letters **4,** 205 (2004)

32. Y. Lu, Y. D. Yin, and Y. N. Xia. *A self-assembly approach to the fabrication of patterned, two-dimensional arrays of microlenses of organic polymers*. Advanced Materials **13,** 34 (2001)

33. J. C. Hulteen and R. P. Vanduyne. *Nanosphere Lithography - A Materials General Fabrication Process for Periodic Particle Array Surfaces*. Journal of Vacuum Science & Technology A-Vacuum Surfaces and Films **13,** 1553 (1995)

34. P. Jiang and M. J. McFarland. *Wafer-scale periodic nanohole arrays templated from two-dimensional nonclose-packed colloidal crystals*. Journal of the American Chemical Society **127,** 3710 (2005)

35. D. Marczewski and W. A. Goedel. *The preparation of submicrometer-sized rings by embedding and selective etching of spherical silica particles*. Nano Letters **5,** 295 (2005)

36. X. D. Wang, C. J. Summers, and Z. L. Wang. *Large-scale hexagonal-patterned growth of aligned ZnO nanorods for nano-optoelectronics and nanosensor arrays*. Nano Letters **4,** 423 (2004)

37. L. M. Goldenberg, J. Wagner, J. Stumpe, B. R. Paulke, and E. Gornitz. *Simple method for the preparation of colloidal particle monolayers at the water/alkane interface*. Langmuir **18,** 5627 (2002)

38. C. Graf, D. L. J. Vossen, A. Imhof, and A. van Blaaderen. *A general method to coat colloidal particles with silica*. Langmuir **19,** 6693 (2003)

39. C. L. Cheung, R. J. Nikolic, C. E. Reinhardt, and T. F. Wang. *Fabrication of nanopillars by nanosphere lithography*. Nanotechnology **17,** 1339 (2006)

40. A. J. Haes, L. Chang, W. L. Klein, and R. P. Van Duyne. *Detection of a biomarker for Alzheimer's disease from synthetic and clinical samples using a nanoscale optical biosensor*. Journal of the American Chemical Society **127,** 2264 (2005)

41. Y. S. Seo, H. Luo, V. A. Samuilov, M. H. Rafailovich, J. Sokolov, D. Gersappe, and B. Chu. *DNA electrophoresis on nanopatterned surfaces*. Nano Letters **4,** 659 (2004)

42. J. Y. Shiu, C. W. Kuo, P. L. Chen, and C. Y. Mou. *Fabrication of tunable superhydrophobic surfaces by nanosphere lithography*. Chemistry of Materials **16,** 561 (2004)

43. H. Yabu and M. Shimomura. *Simple fabrication of micro lens arrays*. Langmuir **21,** 1709 (2005)

44. J. G. C. Veinot, H. Yan, S. M. Smith, J. Cui, Q. L. Huang, and T. J. Marks. *Fabrication and properties of organic light-emitting "nanodiode" arrays*. Nano Letters **2,** 333 (2002)

45. K. H. Park, S. Lee, K. H. Koh, R. Lacerda, K. B. K. Teo, and W. I. Milne. *Advanced nanosphere lithography for the areal-density variation of periodic arrays of vertically aligned carbon nanofibers*. Journal of Applied Physics **97** (2005)

46. Crowley R.J. *US Patent No. 6,258,401 (10 July 1997)*.

47. K. Kempa, B. Kimball, J. Rybczynski, Z. P. Huang, P. F. Wu, D. Steeves, M. Sennett, M. Giersig, D. V. G. L. Rao, D. L. Carnahan, D. Z. Wang, J. Y. Lao, W. Z. Li, and Z. F. Ren. *Photonic crystals based on periodic arrays of aligned carbon nanotubes*. Nano Letters **3,** 13 (2003)

48. F. Yan and W. A. Goedel. *Polymer membranes with two-dimensionally arranged pores derived from monolayers of silica particles*. Chemistry of Materials **16,** 1622 (2004)

49. J. E. Barton and T. W. Odom. *Mass-limited growth in zeptoliter beakers: A general approach for the synthesis of nanocrystals*. Nano Letters **4,** 1525 (2004)

50. F. L. Yap and Y. Zhang. *Protein micropatterning using surfaces modified by self-assembled polystyrene microspheres*. Langmuir **21,** 5233 (2005)

51. J. Rybczynski, U. Ebels, and M. Giersig. *Large-scale, 2D arrays of magnetic nanoparticles*. Colloids and Surfaces A-Physicochemical and Engineering Aspects **219,** 1 (2003)

52. B. D. Rabideau and R. T. Bonnecaze. *Computational predictions of stable 2D arrays of bidisperse particles*. Langmuir **21,** 10856 (2005)

53. Y. N. Xia, B. Gates, Y. D. Yin, and Y. Lu. *Monodispersed colloidal spheres: Old materials with new applications*. Advanced Materials **12,** 693 (2000)

54. Israelachvili J. *Intermolecular & surface forces, second edition*.**,** Elsevier Academic Press, London (1991)

55. E.J.W.Verwey and J.Th.G.Overbeek. *Theory of the stability of lyophobic colloids: The interaction of sol particles having an electric double layer.***,** Elsevier Publishing Company, Inc., New York (1948)

56. B. J. Alder, W. G. Hoover, and D. A. Young. *Studies in Molecular Dynamics .V. High-Density Equation of State and Entropy for Hard Disks and Spheres*. Journal of Chemical Physics **49,** 3688 (1968)

57. W. Stober, A. Fink, and E. Bohn. *Controlled Growth of Monodisperse Silica Spheres in Micron Size Range*. Journal of Colloid and Interface Science **26,** 62 (1968)

58. Madou M.J. *Fundamentals of microfabrication, the science of miniaturization, second edition*.**,** CRC Press, London (2002)

59. Kern W. and Puotinen D. RCA Review **,** 187 (1970)

60. Prepared in collaboration with A. Kosiorek

61. M. A. Correa-Duarte, A. Kosiorek, W. Kandulski, M. Giersig, and L. M. Liz-Marzan. *Layer-by-layer assembly of multiwall carbon nanotubes on spherical colloids*. Chemistry of Materials **17,** 3268 (2005)

62. Pawelczyk M. Private communication

63. Glaczynska H. Private communication

64. Jarzebinska R. Private communication

65. J. W. Goodwin, R. H. Ottewill, and A. Parentich. *Optical Examination of Structured Colloidal Dispersions*. Journal of Physical Chemistry **84,** 1580 (1980)

66. D. J. Robinson and J. C. Earnshaw. *Initiation of Aggregation in Colloidal Particle Monolayers*. Langmuir **9,** 1436 (1993)

67. R. Aveyard, J. H. Clint, D. Nees, and V. N. Paunov. *Compression and structure of monolayers of charged latex particles at air/water and octane/water interfaces*. Langmuir **16,** 1969 (2000)

68. D. J. Robinson and J. C. Earnshaw. *Experimental-Study of Colloidal Aggregation in 2 Dimensions .1. Structural Aspects*. Physical Review A **46,** 2045 (1992)

69. D. F. Williams and J. C. Berg. *The Aggregation of Colloidal Particles at the Air-Water-Interface*. Journal of Colloid and Interface Science **152,** 218 (1992)

70. G. Raina, G. U. Kulkarni, and C. N. R. Rao. *Surface enrichment in alcohol-water mixtures*. Journal of Physical Chemistry A **105,** 10204 (2001)

71. M. Tarek, D. J. Tobias, and M. L. Klein. *Molecular dynamics investigation of an ethanol-water solution*. Physica A **231,** 117 (1996)

72. M. A. Wilson and A. Pohorille. *Adsorption and solvation of ethanol at the water liquid-vapor interface: A molecular dynamics study*. Journal of Physical Chemistry B **101,** 3130 (1997)

73. M. Tarek, D. J. Tobias, and M. L. Klein. *Molecular dynamics investigation of the surface/bulk equilibrium in an ethanol-water solution*. Journal of the Chemical Society-Faraday Transactions **92,** 559 (1996)

74. B.V.Derjaguin and L.Landau. *Theory of the stability of strongly charged lyophobic sols and of the adhesion of strongly charged particles in solution of electrolytes*. Acta physicochimica URSS **14,** 633 (1941)

75. V. N. Paunov, P. A. Kralchevsky, N. D. Denkov, and K. Nagayama. *Lateral Capillary Forces Between Floating Submillimeter Particles*. Journal of Colloid and Interface Science **157,** 100 (1993)

76. D. Stamou, C. Duschl, and D. Johannsmann. *Long-range attraction between colloidal spheres at the air-water interface: The consequence of an irregular meniscus*. Physical Review e **62,** 5263 (2000)

77. A. J. Hurd. *The Electrostatic Interaction Between Interfacial Colloidal Particles*. Journal of Physics A-Mathematical and General **18,** 1055 (1985)

78. X. Y. Zhang, A. V. Whitney, J. Zhao, E. M. Hicks, and R. P. Van Duyne. *Advances in contemporary nanosphere lithographic techniques*. Journal of Nanoscience and Nanotechnology **6,** 1920 (2006)

79. A. J. Parker, P. A. Childs, and R. E. Palmer. *Design and fabrication of colloid-based vertical nanoscale devices*. Microelectronic Engineering **61-2,** 681 (2002)

80. M. Winzer, M. Kleiber, N. Dix, and R. Wiesendanger. *Fabrication of nano-dot- and nano-ring-arrays by nanosphere lithography*. Applied Physics A-Materials Science & Processing **63,** 617 (1996)

81. Kosiorek A., Kandulski W., Glaczynska H., and Giersig M. *Fabrication of Nanoscale Rings, Dots, and Rods by Combining Shadow Nanosphere Lithography and Annealed Polystyrene Nanosphere Masks*. Small **1,** 439 (2005)

82. J. Aizpurua, P. Hanarp, D. S. Sutherland, M. Kall, G. W. Bryant, and F. J. G. de Abajo. *Optical properties of gold nanorings*. Physical Review Letters **90** (2003)

83. C. W. Kuo, J. Y. Shiu, Y. H. Cho, and P. Chen. *Fabrication of large-area periodic nanopillar arrays for nanoimprint lithography using polymer colloid masks*. Advanced Materials **15,** 1065 (2003)

84. C. W. Kuo, J. Y. Shiu, and P. L. Chen. *Size- and shape-controlled fabrication of large-area periodic nanopillar arrays*. Chemistry of Materials **15,** 2917 (2003)

85. C. W. Kuo, J. Y. Shiu, P. L. Chen, and G. A. Somorjai. *Fabrication of size-tunable large-area periodic silicon nanopillar arrays with sub-10-nm resolution*. Journal of Physical Chemistry B **107,** 9950 (2003)

86. D. G. Choi, H. K. Yu, S. G. Jang, and S. M. Yang. *Colloidal lithographic nanopatterning via reactive ion etching*. Journal of the American Chemical Society **126,** 7019 (2004)

87. A. Valsesia, P. Colpo, M. M. Silvan, T. Meziani, G. Ceccone, and F. Rossi. *Fabrication of nanostructured polymeric surfaces for biosensing devices*. Nano Letters **4,** 1047 (2004)

88. A. V. Whitney, B. D. Myers, and R. P. Van Duyne. *Sub-100 nm triangular nanopores fabricated with the reactive ion etching variant of nanosphere lithography and angle-resolved nanosphere lithography*. Nano Letters **4,** 1507 (2004)

89. D. G. Choi, S. Kim, S. G. Jang, S. M. Yang, J. R. Jeong, and S. C. Shin. *Nanopatterned magnetic metal via colloidal lithography with reactive ion etching*. Chemistry of Materials **16,** 4208 (2004)

90. J. Li, J. Peng, W. H. Huang, Y. Wu, J. Fu, Y. Cong, L. J. Xue, and Y. C. Han. *Ordered honeycomb-structured gold nanoparticle films with changeable pore morphology: From circle to ellipse*. Langmuir **21,** 2017 (2005)

91. W. J. Padilla, D. N. Basov, and D. R. Smith. *Negative refractive index metamaterials*. Materials Today **9,** 28 (2006)

92. Y. N. Xia, J. Tien, D. Qin, and G. M. Whitesides. *Non-photolithographic methods for fabrication of elastomeric stamps for use in microcontact printing*. Langmuir **12,** 4033 (1996)

93. W. Y. Huang, W. Qian, and M. A. El-Sayed. *Coherent vibrational oscillation in gold prismatic monolayer periodic nanoparticle arrays*. Nano Letters **4,** 1741 (2004)

94. T. R. Jensen, M. L. Duval, K. L. Kelly, A. A. Lazarides, G. C. Schatz, and R. P. Van Duyne. *Nanosphere lithography: Effect of the external dielectric medium on the surface plasmon resonance spectrum of a periodic array of sliver nanoparticles*. Journal of Physical Chemistry B **103,** 9846 (1999)

95. P. N. Bartlett, J. J. Baumberg, S. Coyle, and M. E. Abdelsalam. *Optical properties of nanostructured metal films*. Faraday Discussions **125,** 117 (2004)

96. I. I. Smolyaninov, C. C. Davis, V. N. Smolyaninova, D. Schaefer, J. Elliott, and A. V. Zayats. *Plasmon-induced magnetization of metallic nanostructures*. Physical Review B **71** (2005)

97. A. J. Haes, C. L. Haynes, A. D. McFarland, G. C. Schatz, R. R. Van Duyne, and S. L. Zou. *Plasmonic materials for surface-enhanced sensing and spectroscopy*. MRS Bulletin **30,** 368 (2005)

98. F. Yan and W. A. Goedel. *Preparation of mesoscopic gold rings using particle imprinted templates*. Nano Letters **4,** 1193 (2004)

99. K. L. Kelly, E. Coronado, L. L. Zhao, and G. C. Schatz. *The optical properties of metal nanoparticles: The influence of size, shape, and dielectric environment*. Journal of Physical Chemistry B **107,** 668 (2003)

100. J. Sort, H. Glaczynska, U. Ebels, B. Dieny, M. Giersig, and J. Rybczynski. *Exchange bias effects in submicron antiferromagnetic-ferromagnetic dots prepared by nanosphere lithography*. Journal of Applied Physics **95,** 7516 (2004)

101. S. M. Weekes, F. Y. Ogrin, and W. A. Murray. *Fabrication of large-area ferromagnetic arrays using etched nanosphere lithography*. Langmuir **20,** 11208 (2004)

102. W. H. Ma, D. Hesse, and U. Gosele. *Nanostructure patterns of piezoelectric and ferroelectric complex oxides with various shapes, obtained by natural lithography and pulsed laser deposition*. Nanotechnology **17,** 2536 (2006)

Acknowledgments

At the end, I would like to acknowledge my gratitude to a number of different people without whom, this work could not be realized.

I would like to express a deep gratitude to Prof. Karsten Buse for providing an opportunity to finish my PhD in his group. It was a great honour to experience his motivation, support, critical comments and guidance throughout writing part of my PhD.

My special thanks go to Prof. Michael Giersig, not only for providing an advanced laboratory environment, stimulating ideas and international cooperation with many scientific groups but also for showing the backstage appearance of a scientific life.

I am particularly thankful to my project colleague, Adam Kosiorek, for a very fruitful collaboration in shadow nanosphere lithography and all side-projects we have been through. Exciting ideas, discussions and experiments performed together but also his endless patience made my work a very fun and pleasant activity.

Many thanks go to Prof. Dr. Karl Maier for being my co-referee and to Prof. Dr. Moritz Sokolowski and Prof. Dr. Bernard Metsch for participating in my disputation as an examination commettaee memebers.

Furthermore, I would like acknowledge my appreciation for great time, which I have spent in at caesar - Research Center in a cleenroom facility of Dr. Manfred Lacher, learning how to work in a high-standard lithographic laboratory. I am thankful to: Peter Holik, Rene Borowski for endless patience and advices during numerous evaporation processes and modification of an evaporator (Hope it is still works :-)); Jacha van Hout and Marion Baer for servicing numerous etching processes; Jorg Scheurer for introducing me into mask preparation techniques. This acknowledgement would not be complete without mentioning their helpful and responsible attitude, which certainly helped me to survive the work in the cleenroom.

Thanks go to Dr. Michael Hilgendorf, which supported me with his extensive knowledge in physical chemistry and thought how to stay alive in the laboratory.

I would like to thank Renata Jarzebinska, Dr. Tobias Jungk and Dr. Helge Eggert, for useful advices and critical comments regarding my Ph.D thesis.

I thank Dr. Peter Karageorgiev for very inspiring cooperation and discussions regarding on numerous scientific subjects.

I express my deep gratitude to my girlfriend - Renata Jarzebinska, which patiently and continuously supported me in my actions.

Nothing would be easy without very helpful assistance of Ms. Jolanta Kremer and Ms. Raja Bernard. Particularly I would like to express my gratitude to. Jolanta Kremer for her help regarding accommodation problems, and numerous text translations.

Last but not least, I would like to thank many other people, particularly: present and past members of Nanoparticle Technology Group and other neighbouring groups, family who accompanied me all along my stay in Bonn and old friends from my home-city - Poznań. Great atmosphere they have created contributed to my very good mood.

List of own Publications

- W. Kandulski, A. Kosiorek, J. Rybczynski, D. Bauman, M. Giersig. *Preparation and characterization of two-dimensional ordered arrays of metallic nanoparticles.* Acta Physica Polonica A **104**, 495-502 (2003)

- A. Kosiorek, W. Kandulski, P. Chudzinski, K. Kempa, M. Giersig. *Shadow nanosphere lithography: Simulation and experiment.* Nano Letters **4**, 1359-1363 (2004)

- A. Kosiorek, W. Kandulski, H. Glaczynska, M. Giersig. *Fabrication of nanoscale rings, dots, and rods by combining shadow nanosphere lithography and annealed polystyrene nanosphere masks.* SMALL **1**, 439-444 (2005)

Curriculum vitae

WITOLD KANDULSKI

Date	1978
Country and place of birth	Poznań, Poland
Citizenship	Polish

EDUCATION AND RESEARCH EXPERIENCE

M.Sc. Eng. Studies	University of Technology in Poznań, Poland
	1997 – 2002
Scholarships during studies:	EU - Socrates/Erasmus programme at University of Applied Sciences, Wildau, Germany
	12.03.2001 – 14.06.2001
	Sommer Student Programm 2001 at Hahn-Meitner-Institut, Berlin, Germany
	06.08. - 28.09.2001
Visiting scientist at:	Hahn-Meitner-Institut, Berlin, Germany
	01.12.2002 – 01.04.2003
	Center of Advanced European Studies and Research, Bonn, Germany
	01.06.2003 – 31.10.2006
Ph.D. Studies	Rheinischen Friedrich-Wilhelms-Universität Bonn, Germany
	Ph.D. thesis title: Shadow nanosphere lithography
	01.10.2006 – present

July 2007, Bonn